UNIVERSITÀ
DEGLI STUDI
DI PADOVA

Sede Amministrativa: Università degli Studi di Padova
CISAS – Centro d’Ateneo di Studi ed Attività Spaziali G. Colombo

---

SCUOLA DI DOTTORATO DI RICERCA IN: SCIENZE TECNOLOGIE E MISURE SPAZIALI
INDIRIZZO: MISURE MECCANICHE PER L’INGEGNERIA E LO SPAZIO
CICLO XXVII

INVESTIGATION OF DEORBITING SYSTEMS USING PASSIVE ELECTRODYNAMIC PROPULSION

Direttore della Scuola: Ch.mo Prof. Giampiero Naletto
Coordinatore d’indirizzo: Ch.mo Prof. Stefano Debei
Supervisore: Ch.mo Prof. Enrico Lorenzini
Co-Supervisore: Ch.mo Prof. Juan Sanmartín

Dottorando: Riccardo Mantellato

Abstract

In the last decade, the continuous and alarming growth of space debris prompted many space agencies all over the world to adopt debris mitigation strategies. Present guidelines indicate the need to deorbit new satellites launched into low Earth orbit (LEO) within 25 years from their end of life. At present, a space-proven technology suitable to carry out a complete deorbit utilizes classical chemical propulsion. However, a deorbit maneuver by means of chemical rocket strongly affects the satellite propulsion budget, thus limiting the operational life of the satellite. These issues bring the need to develop innovative deorbiting technologies. One of these consists in using electrodynamic tethers that, through its interaction with the Earth ionosphere and magnetic field, can take advantage of Lorentz forces for deorbiting. Previous studies have shown the effectiveness of such a technology to deorbit LEO satellites from different altitudes and inclinations in a relatively short time. This work addresses some of the issues of deorbit systems based on electrodynamic tether systems. First, a passive elastic-viscous damping device installed at the attachment point of the tether to the spacecraft is studied to damp the low and yet continuous injection of energy into the system produced by Lorentz forces that, in the long run, can bring the tether to instability. Second, the issues related to the in-orbit deployment of a tape-shaped tether from a non-tumbling spacecraft are attacked to find simple and effective solutions. The chosen strategy is to deploy a tethered tip mass following a pre-determined flight path fed forward to a linear proportional-derivative closed-loop control operated by a brake system mounted on the deployer reel. Lastly, an optimization process for bare electrodynamic tether systems has been developed. The analysis focuses on the deorbiting performances of electrodynamic tether systems from LEO high ranking hot spot regions (e.g., sun-synchronous orbits), and includes a realistic mass budget of a deorbiting system suitable for small satellites.

Summary

The concept of *Tether Satellite System* was proposed to NASA and ASI at the beginning of '70s by Mario Grossi and Giuseppe Colombo. A tether satellite system is a space system that consists of the fundamental elements:

- the *mother spacecraft* must carry the sub-satellite and the tether until they are deployed;
- typically, the tether is several kilometer long and is made of high-strength material. Its main task is to keep mechanically connected the mother spacecraft with the sub-satellite;
- the sub-satellite is deployed from the mother spacecraft taking advantage of the gravity gradient.

To date, several space applications which involve the use of space tether systems have been proposed. Among the others, they include the Momentum Exchange Tethers, the active debris removal missions by means of tethered nets or harpoons, the tethered formation flight, the electric solar wind sails, the Tethered Electromagnetic soft-Docking concept, the ElectroDynamic Tethers, etc. The purpose of this thesis is the investigation of end-of-life deorbit devices based on the Bare Electrodynamic Tethers technology (BETs). The work that was carried out by the Author during his Ph.D. experience and that eventually led to the writing of this thesis was done in the framework of the FP7 "*BETs Project*" (BETs) funded by the European Commission in the 3-year-period 2012-2014.

The *Bare Electrodynamic Tethers Project* had the aim to research and develop a new technology based on electrodynamic tethers suitable to deorbit satellites at the end of their operational lives. The leading requirement of the investigation was to develop a reliable, competitive, and effective system. Within *BETs Project*, the deployment control of tape-shaped tether was investigated, plasma-tether interaction models were validated in plasma chambers, an extensive test campaign on debris impacts and survivability of the tether was conducted, and prototypes of the key subsystems were built by the BETs team. To be successful in their mission, *BETs* partners had to solve a number of issues that characterize the electrodynamic tethers. In this context the BETs research team at University of Padova, of which I was part of, took care of the dynamical aspects of the tethered system.

A BET system is composed of a passive reeling deployer from which a tethered tip mass is to be deployed with the aid of a low-thrust propulsion system located inside the tip mass itself. The deployer has a mechanical brake system positioned

in the inner supporting ring utilized in a feedback loop to control the tether deploying velocity. Tether in-line thrusters are to be turned on at the beginning of the deployment maneuver to provide a continuous and stable unreeling force without transmitting sudden tugs to the relative high-inertia reel, which would occur in case of a spring-initiated deployment. Once the deployment maneuver has ended the conductive bare tape-shaped tether starts to collect electrons from the Earth ionosphere that are re-emitted back through a plasma contactor, thus producing an electric current flowing inside the tether. In turns, the current interacts with the magnetic field according to Lorentz law producing drag forces distributed along the tether.

Several studies on electrodynamics tethers dynamic have been carried out since early 2000s. One of the most severe dynamical issue that must be dealt with is the stability of the tether dynamics throughout the deorbit maneuver. The interaction between tether and plasmasphere, in fact, produces a continuous injection of energy into the system that increases the amplitude of the tether oscillations over time. This effect can produce a reduction of the system efficiency and, in the worst case, cause dynamic instability (e.g., tether rolling around the mother satellite). In the last two decades many authors studied the dynamic instabilities of space tethers and the countermeasures that could be employed to prevent them. They included the use of internal tether frictions, active longitudinal damping devices, active current controls, movable booms, etc. In the first part of the thesis, new insights were gained on the use of a mechanical damper, installed at the attachment point between tether and spacecraft, to dissipate part or the whole of the oscillation energy of an electrodynamic tether. Unlike what has been done up to now, an investigation utilizing a damped two-bar model was used: the first bar represents the damper (a few meters long fishing rod) whereas the second bar is the tether. The final goal of the investigation was to maximize the energy transfer from the electrodynamic tether into the damper and thus its dissipation.

The deployment of a tether in space has been a critical phase for past tethered mission. Some of them experienced failures or malfunctions in orbit, mostly due to malfunctioning of the deployer control subsystem or ejection mechanism. Nonetheless, there have also been fully successful tethered space mission. Among all, the two NASA missions SEDS-1 and SEDS-2 that were specifically designed to test dedicated hardware and control strategies for the deployment of a multi-km tether from a non-spinning orbiting object (i.e., a DELTA-II second stage). The purpose of the work in the second part of the thesis is to study the issues related to the deployment of a BETs system and to find simple and effective solutions. Building on the success of the SEDS-2 deployment, we chose to utilize a strategy similar to the one implemented in that mission, that is to deploy the tip mass following a pre-determined flight path fed forward to a linear proportional-derivative closed-loop control operated by a brake system mounted on the deployer reel. This is to be done by controlling instantaneous tether length and velocity by means of a suitable set of sensors (e.g., incremental encoders) in order to force the tip mass to follow the reference trajectory.

In the last part of the thesis a new optimization process for BETs systems has been studied. Within *BETs Project*, bare electrodynamic tether systems have been studied overall to deorbit high-mass satellites, say of the order of 1000 kg. Investigation results on deorbiting performances suggest that BETs could be highly competitive on deorbiting mid-to-high mass satellites from high LEO ($<$1000 km) at every inclination. Instead, here we focused on the study of a scaled-down version of an EDT system suitable to provide deorbiting services to small satellites with mass in the 100-200 kg range. To do this a very common (and therefore densely populated by space debris) mission profile has been selected, that is a mid-LEO sun-synchronous orbit. The study was carried out by means of two software which were developed specifically for *BETs Project*. First, a preliminary semi-analytical study has been carried to find the optimized BET configuration for a given set of input variables such as orbit altitude, inclination, satellite mass, etc. Subsequently, the results thus obtained were used as input in an accurate tether simulator that utilizes a comprehensive model that takes into account both lateral and longitudinal motion of the tether along with all the latest environment routines. Results from the two software have shown to be comparable and this study points out that their combined use can be effective in finding an efficient and reliable configuration of BET systems used for deorbiting purposes.

Sommario

Proposto alla NASA e all'ASI agli inizi degli anni '70 da M. Grossi e G. Colombo, il concetto di *satellite a filo* è un sistema spaziale costituito da tre elementi fondamentali:

- il satellite-base, oltre al bus e al payload, deve contenere il sub-satellite e il tether fino al suo dispiegamento;
- il tether è un filo ad elevata resistenza, tipicamente lungo qualche chilometro, che deve mantenere il collegamento tra il satellite-base e il sub-satellite;
- il sub-satellite è rilasciato dalla base e si estende per effetto del gradiente di gravità.

Ad oggi, le proposte di utilizzo dei satelliti a filo sono diverse e varie. Tra le principali si annoverano i sistemi a filo per lo scambio del momento angolare, le missioni di rimozione attiva di detriti spaziali tramite reti e arpioni, il volo in formazione tramite fili, le vele solari con fili elettrostatici, il soft-docking elettromagnetico, i fili elettrodinamici, etc. Lo scopo di questa tesi è l'indagine su dispositivi per il rientro di satelliti a fine vita basati sulla technologia dei fili elettrodinamici (Bare Electrodynamic Tethers). La ricerca condotta durante il periodo del dottorato dall'autore è stata effettuata all'interno del progetto FP7 finanziato dalla Commissione Europea nel triennio 2012-2014 denominato "*BETs Project*".

Il progetto *BETs* (*Bare Electrodynamic Tethers*) aveva il compito di ricercare e sviluppare una nuova technologia basata sull'uso di fili elettrodinamici per il rientro in atmosfera di satelliti alla fine della loro vita operativa. Il requisito principale dell'indagine era quello di sviluppare un sistema affidabile, competitivo ed efficacie. All'interno del progetto *BETs* si è studiato il controllo del dispiegamento di un filo a nastro, i modelli di interazione tra un filo conduttore e un plasma sono stati validati in laboratorio, esaurienti test sulla capacità di sopravvivenza di un filo ad un impatto iperveloce sono stati condotti, i sottosistemi principali sono stati prototipati. Per terminare il progetto con successo, i partners del team *BETs* hanno anche dovuto affrontare e risolvere alcuni problemi che caratterizzano i sistemi a filo elettrodinamico. In questo contesto, il team di ricerca dell'Università di Padova, di cui facevo parte, si è occupato degli aspetti dinamici di tali sistemi.

Un sistema BET è composto da un meccanismo di dispiegamento passivo a rocchetto (deployer) attorno al quale è avvolto il filo e dal quale il sub-satellite, sempre connesso tramite il filo al satellite-base, deve essere dispiegato con l'aiuto

di un sistema di propulsione a bassa spinta installato all'interno del sub-satellite stesso. Il deployer è dotato di un sistema di frenaggio posizionato sull'albero del rocchetto, utilizzato per controllare la velocità di uscita del tether attraverso un controllo in feedback. I propulsori, che agiscono lungo l'asse longitudinale del filo, devono essere accesi all'inizio della manovra di dispiegamento per fornire una forza continua e stabile al sub-satellite senza provocare strattoni al sistema. Una volta che la fase di dispiegamento è giunta a termine il filo, costruito con materiali conduttivi, comincia a catturare gli elettroni dal plasma della ionosfera che poi saranno riemessi da un plasma contactor (catodo), producendo così una corrente elettrica all'interno del filo. A sua volta, la corrente elettrica interagisce con il campo magnetico terrestre secondo la legge di Lorentz producendo le forze di drag responsabili del decadimento dell'orbita del satellite-base.

Nei primi anni 2000 sono stati portati avanti svariati studi sui sistemi a filo elettrodinamico. Uno dei problemi carattistico di questi sistemi è la loro stabilità dinamica durante la manovra di rientro. L'interazione tra il filo e la plasmasfera, infatti, produce una continua immissione di energia nel sistema che tende ad aumentare l'ampiezza delle oscillazioni del filo. Questo fenomeno porta solitamente a una riduzione dell'efficienza del sistema e, nei casi peggiori, alla sua instabilità dinamica, facendo per esempio arrotolare il filo attorno al satellite-base. Negli ultimi due decenni molto autori hanno studiato le instabilità dinamiche dei sistemi a filo e con esse le possibili contromisure che possono essere adottate per previrle. Queste contromisure comprendono l'uso dell'attrito interno del filo, lo smorzamento attivo delle oscillazioni longitudinali del filo, il controllo attivo della corrente elettrica, l'utilizzo di estensioni mobili, etc. Nella prima parte di questa tesi, nuove scoperte sono state fatte sull'uso di un sistema di smorzamento passivo basato sul meccanismo massa-molla-smorzatore da applicare all'interfaccia tra il filo e il satellite-base. L'intenzione è quella di dissipare in modo completamente passivo una parte o la totalità dell'energia di oscillazione del filo elettrodinamico. Diversamente da quanto fatto finora, lo studio è stato effettuato facendo uso di un modello semplificato a due barre smorzate: la prima barra rappresenta lo smorzatore (si immagini una canna da pesca lunga alcuni metri), mentre la seconda barra modelliza il filo. Lo scopo finale della ricerca è stato quello di massimizzare il trasferimento dell'energia cinetica dal filo allo smorzatore, e qui dissiparla.

In passato, il dispiegamento di un filo nello spazio ha sempre rappresentato una fase critica per le missioni spaziali che utlizzavano tale tecnologia. Alcune hanno subito degli insucessi o malfunzionamenti in orbita, il più delle volte dovuti al malfunzionamento del sottosistema di controllo del dispiegamento o del meccanismo di eiezione del sub-satellite. Tuttavia ci sono state anche missioni che si sono concluse con un pieno successo. Tra le altre, ricordiamo le due missioni della NASA denominate SEDS-1 e SEDS-2, le quali erano state progettate specificamente per testare un deployer e le strategie di controllo per il dispiegamento di un filo lungo 20 km. L'obiettivo della seconda parte della tesi è stato quello di studiare i problemi relativi allo spiegamento di un sistema con tecnologia BETs e di trovarne soluzioni efficaci e semplici. Motivati dal successo della missione SEDS-2, è stato scelto di utilizzare la stessa strategia di dispiegamento utilizzata in tale missione. Essa prevede il dispiegamento del sub-satellite seguendo una traiettoria predefinita tramite l'uso di un controllo in retroazione operato dall'attuatore (sistema frenante) montato sul deployer. In breve, ciò è possibile se velocità e posizione istantanee del filo sono controllate attraverso un appropriato set di sensori (per esempio degli encoders incrementali) con lo scopo di forzare il sub-satellite a seguire la traiettoria di riferimento predeterminata.

Nell'ultima parte della tesi è stato sviluppato un nuovo processo di ottimizzazione per sistemi BETs. All'interno del *BETs Project*, i sistemi a filo elettrodinamico sono stati studiati soprattutto per il rientro di satelliti con massa elevata, per esempio sopra i 1000 kg. I risultati di varie indagine condotte sulle performance di rientro suggeriscono che i sistemi BETs possono essere altamente competitivi per manovre di rientro di satellite con massa medio-alta da orbite basse (<1000 km di altezza) ad ogni inclinazione orbitale. Nello studio di ottimizzazione, invece, ci siamo focalizzati sullo studio di una versione ridotta (in dimensione e massa) di un sistema BETs, utile per effettuare manovre di rientro per satelliti più piccoli con massa compresa tra i 100 e i 200 kg. Per far ciò, è stato scelto un profilo di missione molto comune (e quindi con una densità di detriti spaziali molto alta), ossia un'orbita eliosincrona polare. Lo studio è stato compiuto facendo uso di due software sviluppati *ad-hoc* per *BETs Project*. Per prima cosa, uno studio semi-analitico è stato effettuato per trovare la configurazione del sistema BETs ottimale per un insieme di dati iniziali fissati come l'altezza orbitale di partenza, l'inclinazione, la massa del satellite-base, etc. Successivamente, i risultati provenienti dal primo modulo sono stati usati come input per un software di simulazione che implementa un modello flessibile del filo. Grazie ciò, esso riesce a simulare sia il moto longitudinale che laterale del filo. I due software hanno fornito risultati compatibili tra di loro e lo studio di ottimizzazione ha dimostrato che il loro uso combinato può essere efficacie per trovare una configurazione efficiente e sicura di un sistema BETs.

Dear Mother, dear Father, dear Sister,

Though I'm past one hundred thousand miles, I'm feeling very still, and I think my spaceship knows which way to go. Tell my wife I love her very much, she knows.[1]

---

[1] *"Space Oddity", David Bowie (1969)*

Contents

1 Introduction

After I spent a long time thinking on how I could start the introduction of my thesis, I finally decided to begin with a question for who will venture in its reading: *how History, as we know it, would have changed if the European exploration of the American continent was stopped (or strongly slowed down) by some catastrophic event?* Let me explain. Imagine that we are back to the end of 15th century. Christopher Columbus has just discovered the New World disclosing to powerful and greedy European kingdoms an unprecedented chance to get their hands on a gargantuan source of every conceivable riches: a new, endless, virgin territory that must be, they hope, full of precious natural resources that can profusely flow toward their ever-empty treasuries. Europe has been an unique theater of war ceaselessly in the last one thousand years after the fall of the ancient Empire, but now that a boundless new continent is at hand all sovereigns start to consider it as a relief valve to lower the pressure on the European front and are planning to launch, as soon as possible, massive exploration campaigns toward the West Indies. At least those Super Powers that can afford a fleet of robust galleons suitable to cross the old Sea of Atlas...

It's a veritable rush! All Great Powers are rushing to the New World to put flags in the name of their Kings before someone else does it. They are rushing to enlarge Royal Navies, to build bigger and sturdier vessels which can better deal with the sudden Ocean's storms. They rush to strengthen their intelligence networks to figure out enemies intents quickly enough to plan efficient counter-strategies and prevent them taking possession of this or that resource. They rush to develop new technologies that can be of paramount importance when engaging a deadly foe and that could well tip the balance in their favor during uncertain disputes. They are rushing to make their people compact to face national enemies in the name of the immortal Glory and, overall, in the name of Gold and Silver and who knows what other riches the New World will amaze them with. Some of them rush because along with the New World they also see new potential flourishing commercial opportunities... In brief, they are all rushing.

Everybody rushes to launch his own fleet and do not have time to bother about the possible consequences that all these sudden changes will bring to the world. Hundreds of vessels sails toward the Indies and sometimes sails back East with their bays full of valuable goods, sometimes with nothing but a halved sick crew and a lot of work for the dockyards to fix beaten up boats. But sometimes they do not come back at all. Powerful storms, unknown seas full of insidious cliffs and shallows, continuous skirmishes between rival fleets, frequent mutinies of weary, undisciplined, eager crews, pirates attacks, hurricanes and new violent natural catastrophic events, great naval combats for the possession of some strategic islet.

These and other unforeseen events are the causes of a continuous decimation of fleets that, in turn, is slowly but unavoidably making the Indies seas and shores a giant shipwreck graveyard. Also, the ships that are damaged either along the new routes that connect the Old with New World or off-shore of recent conquered islands are sunk on the spot because bringing them back to homeland to have them repaired is way too expensive in terms of money, time, and manpower. Often the damaged ships are sunk too close to the docks, thus increasing the probability of damaging other ships coming from Europe, originating a vicious circle that soon has turned most of the New World harbors dangerous to be approached. Unfortunately, European Kings are deaf to ship commanders protests, which are quickly growing more and more nervous about the increasing risks of damaging or even have their vessel sunk at the end of an exhausting and dangerous Ocean crossing, right where weary crews should find shelter, right in the harbors. “Come on, the Ocean is so big, you will find another way in” all Sovereigns keep on saying to their fleet commanders, “just fetch Us some more gold”. Commanders have no choice: they must keep on doing their work despite the risks. Thus, after have their ships hulls strengthen in any manner that master carpenters could figure out, they lay up for the usual old routes praying their good stars.

And things go on with the same routine for many years, until... One day two cargo ships, filled with thousands pounds of inestimable treasuries, collide while maneuvering in front of a dock built on a big island of the New World, trying to avoid the shipwrecks that emerge from the quite sea surface, and eventually sink. As the two big cargoes are definitely obstructing the access to the dock, it must be closed for an unspecified lapse of time until the entrance is somehow cleared. It also happens that this dock is the only possible access to the island, which is packed with precious natural resources, thus its closure will also have the consequence of preventing any further exploration and exploitation of the island, causing a huge damage to the European Kingdoms for many years. On orders of the most powerful Kings, all the fleets are soon made return home and all the sea routes to the New World are deserted. What if a similar disaster would repeat? What if other important docks of the New World are to be closed? For these reasons the tradings are to be stopped temporarily, and with them the exploration of the New World, until a remedy is found. At least, if it is not too late...

Now, from what I am aware of, History did not go exactly that way. Or, better said, the History *did not end* that way. The rush to the New World exploration actually happened, along with thousands shipwrecks caused by uncountable naval combats and Oceanic storms, but most likely a dock was never shut down because its gateways were obstructed by wrecks. Thus, the exploration of the new overseas territories never stopped. However, the careful and well-informed reader will surely have noticed that the script of the previous paragraphs is also well suited to tell another story, that is the story of the human space era. In fact, if we replace “Christopher Columbus” with “Yuri Gagarin, “New World” with “Universe”, “ship”

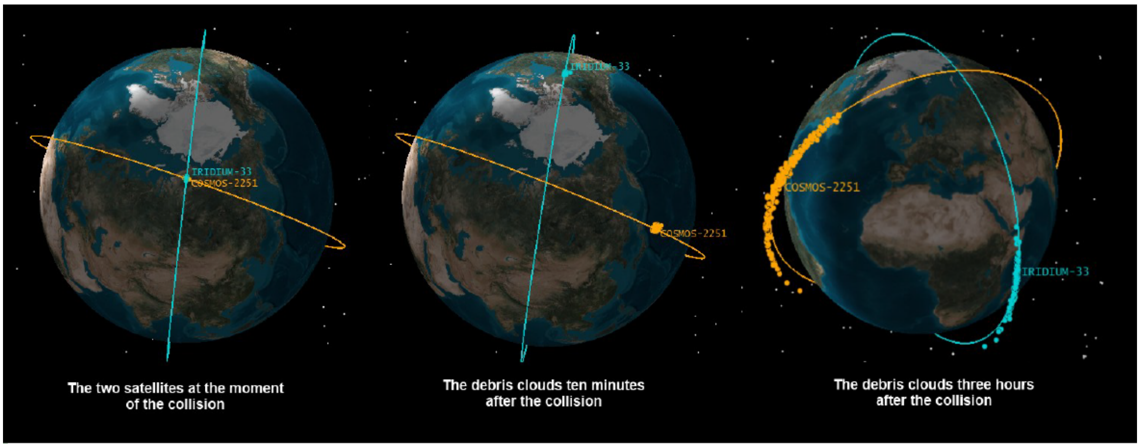

Figure 1.1: The evolution of the formation of the debris cloud produced by the collision between two spacecraft in 2009.

with “spacecraft”, “dock” with “orbit”, “route” with “launch window”, “Kingdoms” with “cold war Super Powers”, “wreck” with “space relict”, and so on, we get in brief (with some due adjustments) the story of the space experience of Mankind from the first successful launch of a satellite in 1957 to the present exploitation of near-Earth orbits under a particular perspective: the problem of the ever-growing number of manmade space debris. Just like happened after the discovering of the American continent by Columbus, when the technologies needed to put a manmade object (or a human being) into orbit were sufficiently mature, all the nations that were capable of producing and handling such technologies (actually, as it will be clear later on, at the beginning of the space era there were only two of them: the Soviet Union and the United States) rushed to invest money on extremely expensive space programs, develop cutting edge technologies, and eventually put hundreds of spacecraft into Earth orbit with massive launch campaigns. During the cold war, the supremacy of the world was contended by two counterposed ideologies and nobody was caring about the “shipwrecks” that the rush to the space dominance would provoke.

Unfortunately, if the high numbers of shipwrecks that studded the American shores never stopped the New World exploration, the huge amount of manmade debris originated by the human space activity since its earliest phases may well pose serious hazards to the near future space missions. As a proof of this, on February 10, 2009, for the first time in history two big space “cargoes” have crushed while orbiting the Earth: the defunct Russian communications satellite Cosmos 2251 collided with the operational U.S. commercial communications satellite Iridium [1]. Figure 1.1 sharply shows the formation of a so called debris cloud originated by the collision. The economic loss was surely remarkable (the revenue of one big communications satellite can reach 1 M$ per day!), however the attention of the worldwide scientific community was focused on something else: up to that moment a collision between two in-orbit spacecraft had been considered possible but highly unlikely to happen. On top of that, the incident

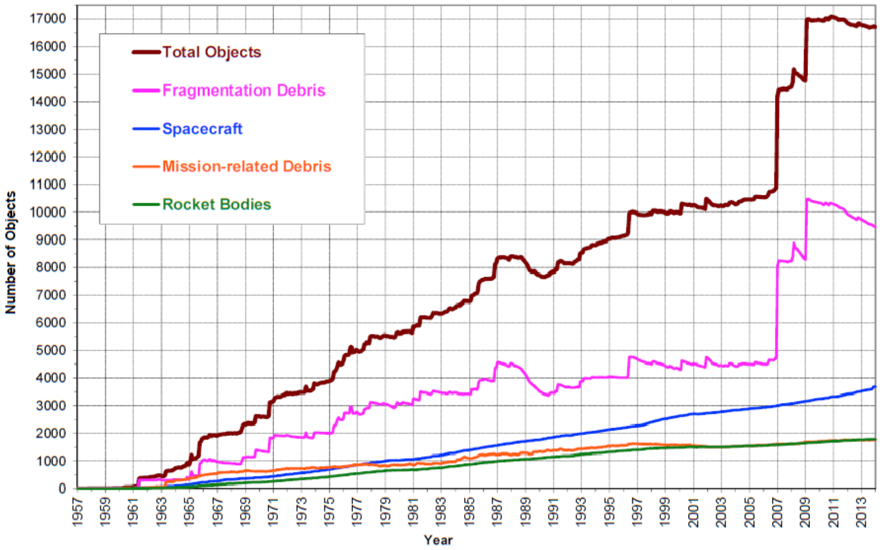

Figure 1.2: Historical evolution of manmade object orbiting the Earth.

originated a tremendous number of new space debris. Experts report that about 2000 pieces of debris measuring at least ten centimeters and many thousands of smaller objects were created after the collision. Figure 1.2 shows the evolution of the number of official manmade objects (both operational and idle) of >10cm size that are being tracked by the U.S. National Aeronautics and Space Administration (NASA). The hike of the fragmentation debris curve in 2009 due to the collision is well visible.

Another even more remarkable hike is sharply showed in Fig. 1.2 in correspondence of year 2007: the one due to the intentional self-destruction of a Chinese spacecraft. On 11 January 2007 an old Chinese meteorological spacecraft, Fengyun-1C, was hit and destroyed by a ground-to-space missile during an anti-satellite test [2]. Regardless of any common sense and prudence, the People's Republic of China intentionally provoked the explosion and destruction of one of its own satellite, giving birth to what is considered the most severe orbital debris cloud in History. Extending from 200 km to more than 4000 km in altitude, the debris originated by the test frequently transit the orbits of hundreds of operational spacecraft, including the human space flight regime, posing new risks to current and future space systems. On top of that, the majority of the debris were thrown by the explosion into long-duration orbits, with decay time measured in decades and even centuries. Two months after the test, more than 1200 debris had been officially cataloged by the U.S. Space Surveillance Network (SSN), and nearly 400 additional debris were being tracked. While the final tally of large (> 5 cm size) debris could well exceed 2000, the number of objects with a size of 1 cm or more is estimated to be as large as 35,000. Both values represent an increase of more than 15% of the known debris environment at the start of 2007. A hilarious sign of fate wanted that the Chinese anti-satellite test was conducted right one month before the United Nations Committee on the Peaceful Uses of Outer Space (COPUOS) adopted a set of space debris mitigation guidelines designed to contain the growth of debris orbiting the Earth....

The little story I wrote at the beginning of this introduction definitely does not want to have any moralizing purpose, indeed it was thought only to make the reader think about the "irresponsible" decisions (or, better said, non-decisions) that historically Human kind never missed to made when it came to ignore the possible future consequences of their actions in the name of immediate benefits, not only with respect to the New World and space exploration (what about the global warming?). Of course, this thesis is about manmade space debris, the hazards that they represent for future human space missions, and the strategies that we could undertake to mitigate their negative effects, so from now on we will focus only on these issues. Thus, I would like to propose an adapted form of the question that is at the beginning of the introduction: *how will the destiny of the Human space History evolve (involve?) if we do not take action to mitigate the hazards stemming from our own rubbish?* In the following sections the space debris issue is briefly presented along with the debris mitigation strategies that, in the last decade, the scientific community is trying to put into effect, with the aim of reducing the impact risks between operational spacecraft with the thousands idle objects of any dimensions that are orbiting the Earth uncontrolled.

1.1 No more space in space: the space junk issue

The total number of space launches from 1957 up to present date is not known precisely. Nonetheless, all available sources agree on the fact that more than 5000 launch vehicles have crossed (or tried to cross) the Karman line (about 100 km from sea level) bringing successfully into Earth orbit more than 7500 spacecraft. In particular, Space Launch Report archive lists 5424 total launches that took place between 4th October 1957 and 31st December 2014, of which 458 ended with a failure [3, 4]. The launch vehicle that was used (and still used!) the most is with no doubt the Russian Semyorka, which is better known as Soyuz: about 1700 total launches in 52 years, something like one every 11 days. The non-governmental website *www.claudelafleur.qc.ca* reports that to date, basing on trustworthy sources, the 59.05% (3216) of launches have been carried out by Russia, 29.56% (1610) by the United States, only 4.44% (242) by European countries, 3.97% (216) by China an the remaining 2.98% (162) by the rest of the world [6]. About 51% of the total launches have been for military use, most of them carried out by URSS and US during the cold war era. Figure 1.3 clearly depicts that after the fall of Berlin Wall and the subsequent dissolution of the Soviet Union and the end of the cold war the number of military launches drastically dropped to an average of about 20% of the total, leaving room to the raise of other governments missions along with commercial satellites. The number of the latter have experienced a remarkable hike between 2010 and 2014 mostly due to the viral diffusion of CubeSats and small satellites, meaning that in the next

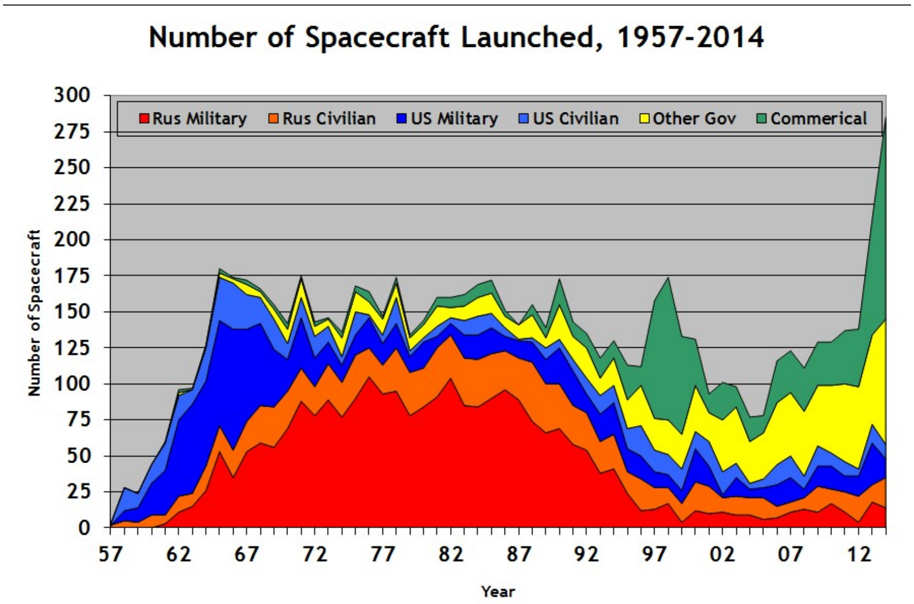

Figure 1.3: Evolution of the number of launched spacecraft from 1957 to date.

future the near-Earth space will most likely become more and more crowded with non-governmental satellites, starting an intense commercial exploitation of Earth orbits.

1.1.1 Space debris

One could wonder: what happened (happens) to all the spacecraft once their operational lives come to an end? When a spacecraft operational life ends it means that all its subsystems cease to function. In particular, the defunct satellite does not communicate with the groundstation and the navigation system does not control its orbit anymore. In brief, due to the (quasi)total absence of any dissipating force in space, a no-more operational satellite will maintain its kinetic energy intact and will be bound to wander uncontrolled around the Earth forever, and no way to make it stop! Actually, if the satellite orbit is low enough (let's say, below 600 km of altitude) the residual atmospheric drag will slowly deorbit into the Earth atmosphere within few decades. So, what exactly a space debris is? The answer is: every manmade object of any size that is orbiting uncontrolled the Earth is a space debris: dead satellites, fragments of satellites originated by disintegration, erosion, and collisions, launchers upper stages, dust from solid rocket motors and nuclear power plants coolant, etc. More than 23000 objects with size >10cm in Low Earth Orbit (LEO) and <0.5-1m in Geostationary orbit (GEO) are being regularly tracked by the U.S. Space Surveillance Network, of which 95% are space debris and the rest 5% are operational satellites. However, if smaller objects are considered, the number of space debris increase drastically.

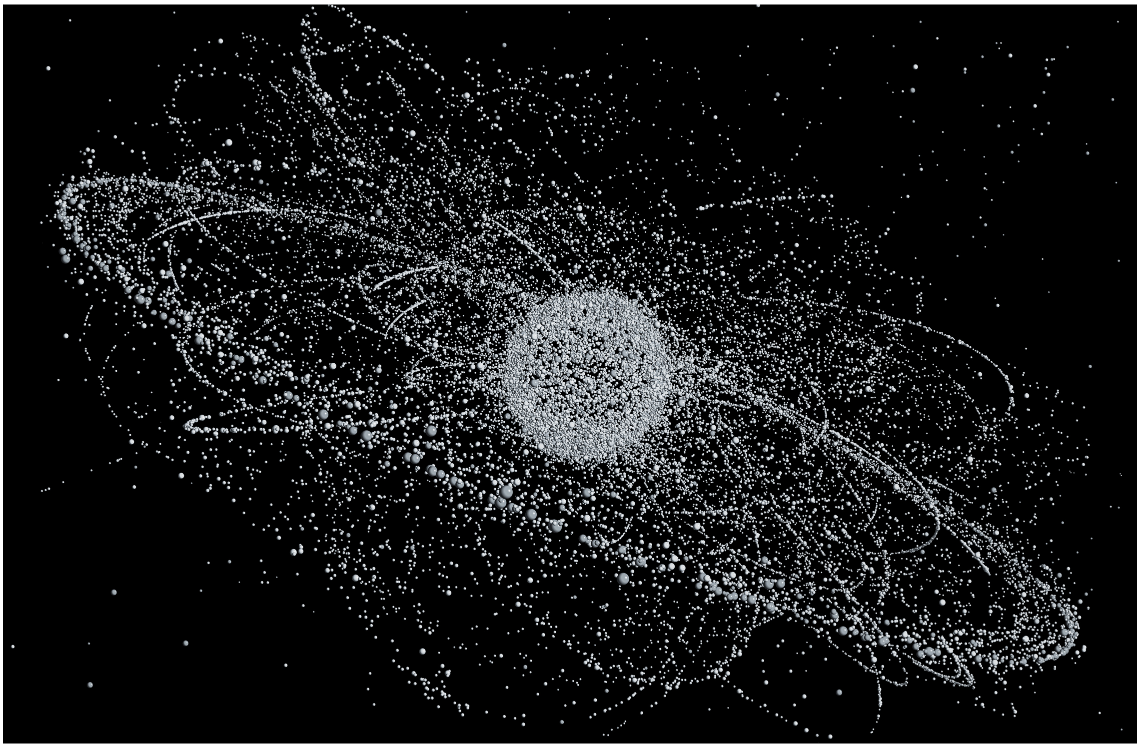

Figure 1.4: Space debris distribution around the Earth (European Space Agency).

According to NASA and ESA (the European Space Agency) there are 300000 objects larger than 1cm below 2000km of altitude. If the considered size is further decreased, experts estimate that there are something like 10 millions objects with size smaller than 1cm. [7]

Up to now only the relevant numbers of launches and space debris have been reported. The next step is to understand what happens when a small space debris (let's say, with size <10cm) hit an operational satellite. The short answer is: a hypervelocity impact happen. Now, the long answer. We deal with hipervelocity when an object velocity is so high that, in case of impact with another object, the inertial forces stemming from the impact are comparable or higher than the material strength. Roughly, the hypervelocity threshold can be set to the reference value of 2.5-3km/s for metals. In this regime, even the most resistant metal behaves like a fluid. Thus, the main consequence of a hypervelocity impact is usually the vaporization of the impactor and, under certain circumstances, of the target. The impact velocity of a space debris with an operational satellite can reach the 16 km/s. At this speed, a single event impact can cause the complete destruction of the satellite (even when space debris of very limited size are involved) if proper countermeasures are not taken. Figure 1.5 shows the result of a 10-km/s impact of a 1-cm diameter aluminum sphere on a 10-cm thick metal plate [8]. Note that the sphere that appears in the figure cannot be the one that impacted the plate: because the impactor must have been vaporized, we imagine

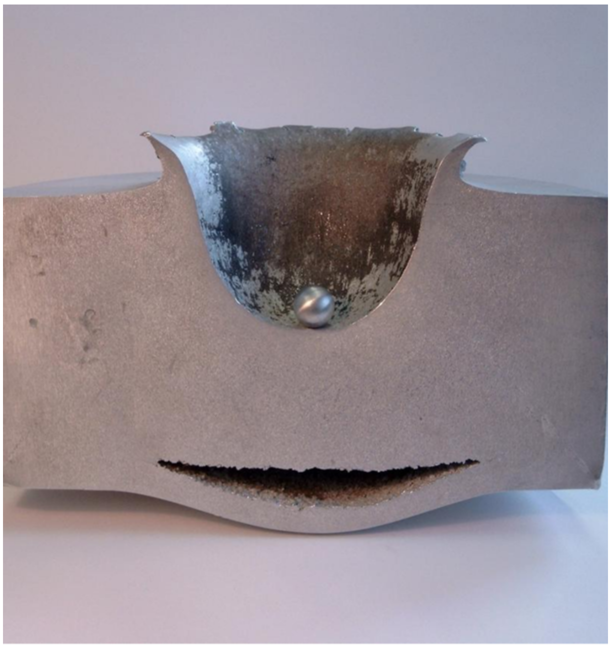

Figure 1.5: ESA space debris studies: hypervelocity impact sample.

that it was positioned inside the crater just to give an idea of its dimension. Thus, everyone can now understand that a space debris impact is “bad”.

Nevertheless, when a space debris impacts an operational satellite, the destruction (or damage) of the satellite is not the only consequence. In fact, a space debris impact usually produces other space debris (debris clouds) and, if we see the problem under a macroscopic point of view, we will notice that we could be dealing with a slow, yet relentless, chain reaction. This theory takes the name of *Kessler Syndrome* after the U.S. scientist Donald J. Kessler that in 1978 formulated it for the first time [9]. In brief, the Kessler syndrome is a realistic scenario in which the density of space debris has reached a certain threshold value that represents a point of no return, that, if passed, will lead to a cascade effect. Collision between objects would then cause other collisions, generating higher and higher number of space debris with no possibility to stop the chain reaction.

Clearly, we still did not reach the Kessler threshold but the two catastrophic events of 2007 and 2009 have made the scientific community to worry about it like never before. That’s why international strategies for the debris mitigation have been settled in 2007 and research groups started to work worldwide to find new viable techniques to mitigate the formation of new space debris.

1.1.2 International agreement on space debris mitigation

As it was already mentioned above, in February 2007 the Scientific and Technical Subcommittee (STSC) of the United Nations’ (UN) Committee on the Peaceful Uses of Outer Space (COPUOS) adopted by consensus a comprehensive set of space debris mitigation guidelines designed to curtail the growth of the Earth’s orbital debris population [10]. The new document culminates a multi-year work plan involving the review of space debris mitigation guidelines by the Inter-Agency Space Debris Coordination Committee (IADC) and the drafting of a similar set of guidelines for Member States of the UN and other international organizations. The document states that “Member States and international organizations should voluntarily take measures, through national mechanisms or through their own applicable mechanisms, to ensure that these guidelines are implemented, to the greatest extent feasible, through space debris mitigation practices and procedures. The STSC document lists seven guidelines.

Guideline 1: Limit debris released during normal operations Space systems should be designed not to release debris during normal operations. If this is not feasible, the effect of any release of debris on the outer space environment should be minimized.

Guideline 2: Minimize the potential for break-ups during operational phases Spacecraft and launch vehicle orbital stages should be designed to avoid failure modes which may lead to accidental break-ups. In the case that a condition leading to such a failure is detected, disposal and passivation measures should be planned and executed to avoid break-ups.

Guideline 3: Limit the probability of accidental collision in orbit In developing the design and mission profile of spacecraft and launch vehicle stages, the probability of accidental collision with known objects during the system’s launch phase and orbital lifetime should be estimated and limited. If available orbital data indicate a potential collision, adjustment of the launch time or an on-orbit avoidance maneuver should be considered.

Guideline 4: Avoid intentional destruction and other harmful activities Recognizing that an increased risk of collision could pose a threat to space operations, the intentional destruction of any on-orbit spacecraft and launch vehicle orbital stages or other harmful activities that generate long-lived debris should be avoided.

Guideline 5: Minimize potential for post-mission break-ups resulting from stored energy In order to limit the risk to other spacecraft and launch vehicle orbital stages from accidental breakups, all on-board sources of stored energy should be depleted or made safe when they are no longer required for mission operations or post-mission disposal.

Guideline 6: Limit the long-term presence of spacecraft and launch vehicle orbital stages in the low Earth orbit (LEO) region after the end of their mission Spacecraft and launch vehicle orbital stages that have terminated their operational phases in orbits that pass through the LEO region, should be removed from orbit in a controlled fashion. If this is not possible, they should be disposed of in orbits which avoid their longterm presence in the LEO region.

Guideline 7: Limit the long-term interference of spacecraft and launch vehicle orbital stages with geosynchronous (GEO) region after the end of their mission Spacecraft and launch vehicle orbital stages that have terminated their operational phases in orbits that pass through the GEO region should be left in orbits which avoid their long-term interference with the GEO region.

Though the STSC agreement do not obligate the subscribing Countries to follow the seven guidelines, it surely represent a fundamental step toward a significative reduction of hazards relative to the space debris issue.

1.1.3 End-of-life mitigation strategies

Apart from the mitigation strategies pinpointed by the STSC international agreement, several active space debris mitigation strategies have been studied in the last decade. They involve the use of end-of-life devices to deorbit a spacecraft once its operational life has come to an end. In the following we summaries, without claiming to be exhaustive, the most common and promising among them. [7]

1.1.3.1 Drag augmentation devices

A drag augmentation device deorbit efficacy relies on the possibility of drastically increasing the front area of the satellite. In fact, in low orbits the main cause of natural orbit decay is due to the energy dissipated by the airdrag. The decay rate is directly proportional to the area-to-mass ratio of the object, thus if the satellite cross-sectional area is intentionally increased the decay rate will also increase. Since the effectiveness of a drag augmentation device relies on the density of the residual atmosphere, this kind of deorbiting technique is particularly effective for orbits which altitude does not exceed, roughly, 700-800 km.

1.1.3.2 Solar sails

Solar sails utilizes the solar radiation pressure to thrust a satellite in a desired direction. Solar photons transfer their momentum to the sail by impinging on its surface and the efficiency of the momentum exchange process increases with the reflectivity of the material. However, if a solar sail attitude is left uncontrolled the decay effect averaged on one orbit would probably be close to null. Thus, an oriented planar solar sail is needed to provide a low but continuous thrust in the opposite direction of satellite velocity. This means that the deorbiting system should be able to determine and control the attitude of the sail, that is no easy task if low power and mass requirements have to be meet. Moreover, solar sails do not work well below 600-800 km because of the oxygen erosion and residual air drag.

1.1.3.3 Chemical propulsion

Chemical rockets is very old and thus reliable technology. They could be employed at the end of one satellite life to give one last ΔV to decrease its orbital energy and lower the perigee, thus drastically decreasing the satellite decay time. Unfortunately, their impact on the satellite mass (and power) budget are usually too high to be implemented when dealing with orbit altitude $>$ 600km.

1.1.3.4 Electrodynamic tethers

Multi-km electrodynamic tethers (EDTs) are deployed from the defunct satellite along the local vertical at the end of its life. They are made of conductive materials and are able to collect electrons from the ionospheric plasma by means of an anodic device, that may consists of a tip-probe located on one tether extremity or the bare tether can operate as anode itself. The collected electrons are re-emitted back to the ionosphere by plasma contactor (cathode), thus an electric current is made flow inside the tether. This in turn interacts with the Earth magnetic field and, according to Lorentz law, produces a drag force that make the mother satellite deorbit. The principal advantage of electrodynamic tethers is that, once deployed, it is completely passive and are able to deorbit satellite from whatever inclination and altitudes up to 1000 km, and more, in relatively short time.

Apart from end-of-life deorbit devices, several research teams all over the world are studying Active Debris Removal strategies which imply the use of dedicated space mission to rendezvous defunct satellites, capture them, and eventually deorbit them into the Earth atmosphere [11, 12, 13]. However, the treatment of these technologies go beyond the scope of this work.

1.2 In this thesis: bare electrodynamic tethers as deorbiting devices

The work that was carried out by the Author during his Ph.D. experience and that eventually led to the writing of this thesis was done in the framework of the FP7 "*BETs Project*" (BETs) funded by the European Commission in the 3-year-period 2012-2014 (project 262972) [14]. BETs project had the aim to research and develop a new technology based on electrodynamic tethers (EDTs) suitable to deorbit satellites at the end of their operational lives. The leading requirement of the investigation was to develop a reliable, competitive, and effective system. In this context, deployment control of tape-shaped tether was investigated, plasma-tether interaction models were validated in plasma chambers, an extensive test campaign on debris impacts and survivability of the tether was conducted, and prototypes of the key subsystems were built by the BETs team. To be successful in their mission, BETs partners had to solve a number of issues that characterize the electrodynamic tethers. In this context the BETs research team at University of

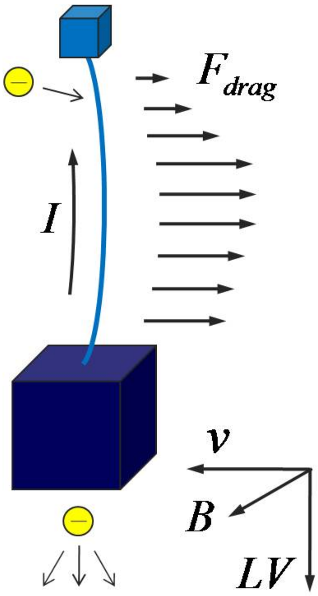

Figure 1.6: Operation scheme of a bare electrodynamic tether system.

Padova, of which I was part of, took care of the dynamical aspects of the tethered system.

An essential sketch of the operation of a bare electrodynamic tether (BET) is shown in Fig. 1.6. While moving along its orbit with a relative velocity $\mathbf{v}_{rel}$ with the surrounding ionospheric plasma, the bare tether continuously cuts the Earth magnetic field B. This results in a motional electric field E_m:

$$E_m = (\mathbf{v}_{rel} \times \mathbf{B}) \cdot \hat{\mathbf{u}}_{\mathbf{t}} \tag{1.1}$$

where $\hat{\mathbf{u}}_{\mathbf{t}}$ is the tether direction. The motional electric field generate an electric current I that flows through the tether: while the electrons are collected by the bare tether from the plasma ionosphere, a plasma contactor serve as a cathode that re-emit the electrons back to the ionosphere, thus closing the electrical circuit. The electric current, in turn, interacts with the Earth magnetic field producing electrodynamic forces F_{el} according to Lorentz law:

$$F_{el} = \int_l I(s)\, \hat{\mathbf{u}}_{\mathbf{t}} \times \mathbf{B} ds \tag{1.2}$$

where s is the arc-length along the tether. These forces are the responsible of the drag action of the BET. The amplitude of these force increases with increasing electric current that can be obtained with longer, thicker, wider tethers. Roughly, the decay time of the satellite is proportional to $\frac{r^6}{L^2 \cos^2 i}$, where r is the geocentric orbit radius, L is the tether length, and i is the orbit inclination.

A BETs system is composed of a passive reeling deployer from which a tethered tip mass is to be deployed with the aid of a low-thrust propulsion system located inside the tip mass itself (see Fig. 3.1). The deployer has a mechanical brake system positioned in the inner supporting ring utilized in a feedback loop to control the tether deploying velocity. Tether in-line thrusters are to be turned on at the beginning of the deployment maneuver to provide a continuous and stable unreeling force without transmitting sudden tugs to the relative high-inertia reel, which would occur in case of a spring-initiated deployment. Once the deployment maneuver has ended the conductive bare tether starts collect electrons from the Earth ionosphere, beginning the deorbiting phase. The tape-shaped tether configuration was preferred to the cylindrical one due to its lower mass and higher efficiency. The electron collection of an electrodynamic tether per unit length depends on the perimeter of its cross section, thus a tape-shaped tether produces the same electrical current of a cylindrical tether of the same perimeter but weights much less. Moreover, a recent study has highlighted that tape-shaped tethers have a much higher survivability to orbital debris impacts than cylindrical ones [19, 20].

Within the framework of the new debris mitigation policies, the technologies based on electrodynamic tethered system have gained a renewed interest, after the space missions in the 90s and 2000s, as they could provide (relatively) simple and low-cost solutions for propellantless end-of-life deorbiting subsystems. Unlike drag sails and balloons, EDTs function very effectively at higher altitudes in LEO where drag sails and balloons are very ineffective and chemical thrusters require a large mass of propellant for deorbiting. In the ‘90s and early ‘00s essential breakthroughs into tether dynamics and plasma physics in space was gained thanks to several space tethered missions, such as SEDS-I and II, TSS-1 and 1R, PMG and TiPS [17]. Moreover, reliable and light deployers were designed and tested successfully in orbits (e.g., SEDS-I and SEDS-II). Robust open and close loop control mechanisms have been designed and successfully employed for tether deployment [18].

Several studies on electrodynamics tethers dynamic have been carried out since early 2000s [20, 22]. One of the most severe dynamical issue that must be dealt with is the stability of the tether dynamics throughout the deorbit maneuver. The interaction between tether and plasmasphere, in fact, produces a continuous injection of energy into the system that increases the amplitude of the tether oscillations over time. This effect can produce a reduction of the system efficiency and, in the worst case, cause dynamic instability (e.g., tether rolling around the mother satellite) [21]. In the last two decades many authors studied the dynamic instabilities of space tethers and the countermeasures that could be employed to prevent them. In early ‘90s Beletsky and Levin proposed some possible ways of damping space tethers oscillations involving internal tether friction, active longitudinal damping, and active current control in the case of EDTs. Furthermore, they also proposed a way to optimize the libration damping with a movable boom modeling the tether as a continuum body (cfr. Chapter 7 of [22]). Levin treated space tether missions once more in 2007, yet without elaborating further on dynamic stabilization [23]. After Beletsky and Levin work many other authors continued the study of tether stabilization, overall by means of active control of the electric current in EDTs [24, 25, 26]. However, Peláez *et al.* studied the effect of a mechanical spring-dashpot for both longitudinal and lateral oscillation damping by modeling the electrodynamic tether as a rigid rod (dumbbell model) [19]. Lorenzini and Menon proposed independently to employ a rotational damper to damp transversal oscillations of an inert tether utilizing impedance-matching methods [27, 28]. The task of the work reported in Chapter 2 is to gain additional insights on the use of a mechanical damper, installed at the attachment point between tether and spacecraft, to dissipate part or the whole of the oscillation energy of the tether. Unlike what has been done up to now, we conduct the investigation utilizing a damped two-bar model: the first bar represents the damper (a few meters long fishing rod) whereas the second bar is the tether. The final goal of the investigation is to maximize the energy transfer from the electrodynamic tether into the damper and thus its dissipation.

The deployment of a tether in space has been a critical phase for past tethered mission. Some of them experienced failures or malfunctions in orbit, mostly due to malfunctioning of the deployer control subsystem or ejection mechanism (see Ref [29] for a list of tethered missions). In the ‘90s one of the two TSS NASA/ASI (Agenzia Spaziale Italiana) missions, which provided important information on tether dynamics and plasma physics, experienced a failure in the deployer subsystem [17]. The missions ATEX [30] and MAST [31] also developed problems early on deployment due to ejection mechanisms. The same happened to the Japanese CubeSat mission STARS [32], whereas the European YES2 achieved a full tether deployment but the swing-and-cut technique was not sufficiently accurate, likely due to a problem in the deployment control system, and the deorbited payload (FOTINO) was not recovered [33]. Nonetheless there have also been fully successful tethered space mission. Among all, the two NASA missions SEDS-1 and SEDS-2 that were specifically designed to test dedicated hardware and control strategies for the deployment of a multi-km tether from a non-spinning orbiting object (i.e., a DELTA-II second stage). In both missions a 20-km tether was deployed from a passive deployer with a spring-based release system. In particular, in SEDS-1 the tether was deployed through a librating maneuver and subsequently cut (hence the term swing-and-cut) to let the tip mass deorbit in the atmosphere following a pre-determined flight path that ended off the coast of Mexico. The prediction of the re-entry trajectory was sufficiently precise to allow the team personnel stationing at pre-selected sites to make photographic observations of the event [17]. The purpose of the work in Chapter 3 is to study the issues related to the deployment of a BETs system and to find simple and effective solutions. Building on the success of the SEDS-2 deployment (with a final libration amplitude of 4° out of a goal of 10°, [34]), we chose to utilize a strategy similar to the one implemented in that mission, that is to deploy the tip mass following a pre-determined flight path fed forward to a linear proportional-derivative closed-loop control operated by a brake system mounted on the deployer reel. This is to be done by controlling instantaneous tether length and velocity by means of a suitable set of sensors (e.g., incremental encoders) in order to force the tip mass to follow the reference trajectory. However, there are two principal differences between SEDS-2 and BETs systems. First, a BET system uses a tape-shaped tether that has to be stored in a reeling mechanism (that is with non-negligible inertia), whereas SEDS-2 utilized a spool with no moving parts. Second, as a consequence of the inertia of the reel, the release of the tip mass in a BET system cannot be done with springs, as it was in SEDS-2, and a low-thrust propulsion system must slowly initiate the deployment maneuver similarly to what was done with the TSS missions. [35, 36]

Finally, in Chapter 4 a new optimization process for BETs systems has been studied. Within *BETs Project*, bare electrodynamic tether systems have been studied overall to deorbit high-mass satellites, say of the order of 1000 kg. Investigation results on deorbiting performances suggest that BETs could be highly competitive on deorbiting mid-to-high mass satellites from high LEO (<1000 km) at every inclination. Instead, here we focused on the study of a scaled-down version of an EDT system suitable to provide deorbiting services to small satellites with mass in the 100-200 kg range. To do this a very common (and therefore densely populated by space debris) mission profile has been selected, that is a mid-LEO sun-synchronous orbit. Sun-synchronous orbits, in fact, represent one of the three high-ranking hotspots regions identified by ESA. The study was carried out by means of two software which were developed specifically for *BETs Project*. First, a preliminary analysis has been carried to find the optimized BET configuration for a given set of input variables such as orbit altitude, inclination, satellite mass, etc. Subsequently, the results thus obtained were used as input in an accurate tether simulator that utilizes a comprehensive model that takes into account both lateral and longitudinal motion of the tether along with all the latest environment routines. Results from the two software have shown to be comparable and this study points out that their combined use can be effective in finding an efficient and reliable configuration of BET systems used for deorbiting purposes.

Bibliography

[1] *Satellite Collision Leaves Significant Debris Clouds*, Orbital Debris Quarterly News, Vol. 13, No. 2, April 2009, pp. 1-3.

[2] *Chinese Anti-satellite Test Creates Most Severe Orbital Debris Cloud in History*, Orbital Debris Quarterly News, Vol. 11, No. 2, April 2007, pp. 2-3.

[3] Space Launch Report, URL: http://www.spacelaunchreport.com/logdec.html. (cited: 29 Jan 2015)

[4] Gunter's Space Page, URL: http://space.skyrocket.de/index.html. (cited: 29 Jan 2015)

[5] The Space Review, URL: http://www.thespacereview.com/article/1598/1. (cited: 29 Jan 2015)

[6] Spacecraft Encyclpedia, URL: http://claudelafleur.qc.ca/Spacecrafts-index.html. (cited: 29 Jan 2015)

[7] Klinkrad, H., Johnson, N.L., *Space debris environment remediation concepts*, Proceedings of 5th European Conference on Space Debris', Darmstadt (DE), 2009.

[8] Space Debris, ESA, URL: http://www.esa.int/Our_Activities/Operations/Space_Debris/Hypervelocity_impacts_and_protecting_spacecraft. (cited: 29 Jan 2015)

[9] Pelton, J.N., *Space Debris and Outer Threats from Outer Space*, "The Space Debris Threat and the Kessler Syndrome", pp. 17-23, SpringerBriefs in Space Development, 2013. doi: 10.1007/978-1-4614-6714-4_2

[10] United Nations Office for Outer Space Affairs, *Space Debris Mitigation Guidelines of the Committee on the Peaceful Uses of Outer Space*, Vienna, 2010.

[11] Ruiz, M., Urdampilleta, I., Bombardelli, C., Ahedo, E., Merino, M., and Cichocki, F., *The FP7 LEOSWEEP Project: improving low Earth orbit security with enhanced electric propulsion*, Space Propulsion Conference 2014, Köln, Germany, 19 - 22 May 2014.

[12] Reed, J., and Barraclough, S., *Development of harpoon system for capturing space debris*, 6th European conference on Space Debris, Darmstadt (DE), 2013.

[13] Zhai, G., and Zhang, J., *Space Tether Net System for Debris Capture and Removal*, 4th Conference on Intelligent Human-Machine Systems and Cybernetics, Nanchang (RC), 2012. doi: 10.1109/IHMSC.2012.71

[14] The Bare Electrodynamic Tethers Project, URL: http://www.thebetsproject.com. (cited: 29 Jan 2015)

[15] Khan, S.B., and Sanmartín, J., *Survival Probability of Round and Tape Tethers Against Debris Impact*, Journal of Spacecraft and Rockets, Vol. 50, No. 3, May 2013, pp. 603-608. doi: 10.2514/1.A32383

[16] Francesconi, A., Giacomuzzo, C., Branz, F., and Lorenzini, E.C., *Survivability to Hypervelocity Impacts of Electrodynamic Tape Tethers for Deorbiting Spacecraft in LEO*, Proceedings of 6th Conference on Space Debris, 2013, April 22-25, Darmstadt, Germany.

[17] Cosmo, M.L., and Lorenzini, E.C., *Tethers in Space Handbook*, 3rd ed., NASA Marshall Space Flight Center, 1997.

[18] Cosmo, M.L., Gullahorn, G.E., Lorenzini, E.C., and Grassi M., *Analysis of SEDS-1 dynamics from on board instrumentation*, Proceedings of the AIAA Space Programs and Technologies Conference and Exhibit, Huntsville, Alabama (USA) 1993.

[19] Peláez, J., Lorenzini, E. C., López-Rebollal, O., and Ruiz, M., *A New Kind of Dynamic Instability in Electrodynamic Tethers*, Journal of the Astronautical Sciences, Vol. 48, No. 4, 2000, pp. 449-476.

[20] Peláez, J., Ruiz, M., López-Rebollal, O., Lorenzini, E. C., *Two-Bar Model for the Dynamics and Stability of Electrodynamic Tethers*, Journal of Guidance, Control and Dynamics, Vol. 25, No. 6, 2002, pp. 1125-1135.

[21] Zanutto, D., Colombatti, G., and Lorenzini, E. C., *Electrodynamic Tethers For Deorbiting Maneuvers*, 3rd CEAS Air&Space Conference, Venice, Italy, 2011.

[22] Beletsky, V. V., Levin, E. M., *Dynamics of Space Tethers Systems*, American Astronautical Society, Advances in the Astronautical Sciences, Volume 83, 1993.

[23] Levin, E. M., *Dynamic Analysis of Space Tether Missions*, American Astronautical Society, Advances in the Astronautical Sciences, Volume 126, 2007.

[24] Williams, P., Watanabe, T., Blanksby, C., Trivailo, P., and Fujii, H. A., *Libration Control of Flexible Tethers Using Electromagnetic Forces and Movable Attachment*, Journal of Guidance, Control, and Dynamics, Vol. 27, No. 5, September-October 2004.

[25] Larsen, M. B., Blanke, M., *Passivity-Based Control of a Rigid Electrodynamic Tether*, Journal of Guidance, Control, and Dynamics, Vol. 34, No. 1, January-February 2011.

[26] Zhong, R., and Zhu, Z. H., *Libration Dynamics and Stability of Electrodynamic Tethers in Satellite Deorbit*, Celestial Mechanics and Dynamical Astronomy, Vol. 116, No. 3, 2013, 0923-2958.

[27] Lorenzini, E. C., Bombardelli, C., Cosmo, M., Harwit, M., Leisawitz, D., Farley, R., Rinehart, S., Quinn, D., and Miller, D., *Far-Infrared/Submillimeter Astronomical Interferometry with Spaceborne Tether Formations*, Astrophysics and Space Science, 2006. doi: 10.1007/s10509-006-9038-7

[28] Menon, C., and Bombardelli, C., *Self-Stabilizing Attitude Control for Spinning Tethered Formations*, Acta Astronautica, 2007, No. 60, pp. 828-833.

[29] Kruijff, M., *Tethers in Space. A Propellantless Propulsion In-Orbit Demonstration*, Ph.D. thesis, Technical University of Delft, 2011.

[30] Johnson, L., Estes, R.D., Lorenzini, E., Martínez-Sánchez, and M., Sanmartín, J., *Propulsive Small Expendable Deployer System*, Journal of Spacecraft and Rockets, Vol. 37, No. 2, pp. 173-176, 2000. doi: 10.2514/2.3563

[31] Sanmartín, J.R., Lorenzini, E.C., and Martínez-Sánchez, M., *Electrodynamic Tethers Applications and Constraints*, Journal of Spacecraft and Rockets, Vol. 40, No. 3, pp. 442-456, 2010. doi: 10.2514/1.45352

[32] Chen, Y., Huang, R., Ren, X., He, L., and He, Y., *History of the Tether Concept and Tether Missions: a Review*, ISRN Astronomy and Astrophysics, Vol. 2013, Article ID 502973, 7 pages, 2013. doi:10.1155/2013/502973

[33] Kruijff, M., Van Der Heide, E.J., and Ockels, W.J., *Data Analysis of a Tethered SpaceMail Experiment*, Journal of Spacecraft and Rockets, Vol. 46, No. 6, Nov.-Dec. 2009, pp. 1272-1287. doi: 10.2514/1.41878

[34] Lorenzini, E.C., Bortolami, S.B., Rupp, C.C., and Angrilli, F., *Control and Flight Performance of Tethered Satellite Small Expendable Deployment System-II*, Journal of Guidance, Control, and Dynamics, Vol. 19, No. 5, Sept.-Oct. 1996, pp. 1148-1156. doi: 10.2514/3.21757

[35] Dobrowolny, M., and Stone, N.H., *A Technical Overview of TSS-1: the First Tethered-Satellite System Mission*, Il Nuovo Cimento C, Vol. 17, No. 1, Jan.-Feb. 1994, pp. 1-12. doi: 10.1007/BF02506678

[36] [Stone, N.H., and Bonifazi, C., *The TSS-1R Mission: Overview and Scientific Context*, Geophysical Research Letters, Vol. 25, No. 4, Feb. 1998, pp. 409-412. doi: 10.1029/97GL02980

2 Passive Damping System for the Stabilization of BETs

The purpose of this study is to analyze by means of analytical and numerical tools the effects on the dynamics of space tethers system produced by the insertion of a mechanical spring-dashpot damping system. Ideally, the damper is to be applied at the interface between the tether and the spacecraft and it should be shaped like a long (on the order of 10 m) and thin rod, i.e. a deployable boom to be unfolded during the tether deployment phase. Previous works had highlighted that a rotational spring-dashpot damper can be useful at adsorbing the tether kinetic energy and thus at stabilizing its dynamic during the deorbiting maneuver. In this section I attack the same physical problem from an analytical point of view trying to answer in a more rigorous way the following driving questions:

- is a mechanical damping device effective in adsorbing the tether kinetic energy?

- does a mechanical spring-dashpot damper improve the dynamical stability of the tether system?

- if so, which is the optimal damper configuration that maximize the tether kinetic energy dissipation?

Provided that the first two questions get positive answers, the problem of choosing a correct configuration of the damper coefficients arises: which damping coefficient will provide the most efficient energy dissipation? Will the elastic element be useful to this scope? More in general, for given orbital, geometric and mass parameters values of the system I sought a function that can provide the best damper configuration:

$$(b^*, k^*) = \hat{f}\left(orbit,\, tether\, geometry,\, physical\, parameters\right) \tag{2.1}$$

where (b^*, k^*) is the optimal pair of damping-elastic coefficients of the dashpot device. As it will be shown in the next sections, from a linearized study it is possible to infer that the answers to the first two driving questions are positive and there actually is an optimization function $\hat{f}$ that can provide the optimal damper coefficients.

Table 2.1 reports the nomenclature used in this chapter according to [4].

Table 2.1: Nomenclature.

a	circular orbit radius
b	angular damping coefficient
b^*	optimal damping coefficient
b_d^*	damping coefficient @ max(TDE)
b_k^*	damping coefficient @ min(MKE)
cx	cos(x)
E_d	dissipated energy by damper
E_k	tether kinetic energy
k	angular elastic coefficient
k^*	optimal elastic coefficient
k_{cr}	critical elastic coefficient
L	sum of two bars lengths
L_i	length of bar i
m_B	tip mass
m_i	mass of bar i
n_{sim}	number of integrated orbits
MKE	Mean Kinetic Energy
sx	sin(x)
t	dimensional time
TDE	Total Dissipated Energy
$\mathbf{u_i}$	unit vector of bar i
α_i	real part of *i-th* eigenvalue
ϑ_i	in-plane angle of bar i
μ	Earth gravitational constant
ρ_{AL}	aluminum volumetric mass density
φ_i	out-of-plane angle of bar i
ω	orbital mean motion
ω_i	*i-th* system natural frequency
Ω_1	angular velocity of 1st bar

Non-dimensional variables and parameters

A	$\Lambda\,(3+\delta_1+3\delta_2)$
B	$(1-\Lambda)\,(2+\delta_2)$
D	$-\Lambda\,(2+\delta_2)$
E	$(1-\Lambda)\,(3+\delta_2)$
β	$b/\left(\omega m_B \Lambda L^2\right)$
δ_i	m_i/m_B
κ	$k/\left(\omega^2 m_B \Lambda L^2\right)$
κ^*	optimal elastic coefficient
κ_{cr}	critical elastic coefficient
η	$12/\left(4AE+9BD\right)$
τ	non-dimensional time ωt
$\hat{\tau}$	relaxation time
Λ	L_1/L

Superscripts

$\dot{x}$	dx/dt
$\ddot{x}$	d^2x/dt^2
x'	$dx/d\tau$
x''	$d^2x/d\tau^2$

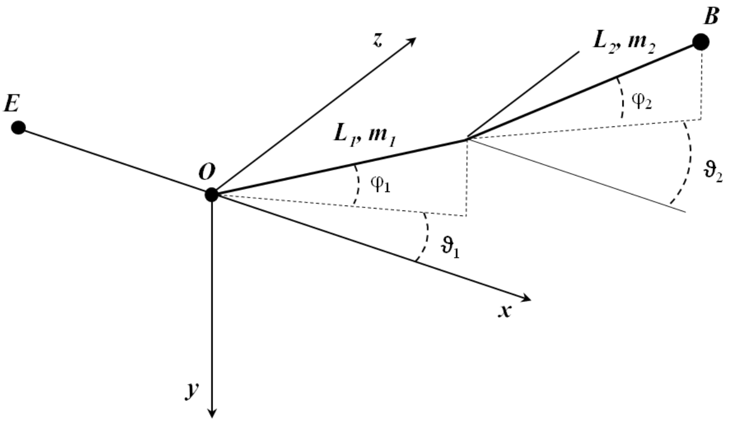

Figure 2.1: Synodic reference frame.

2.1 The damped two-bar model

The aim of the present study is to characterize the dynamics of space tether which lateral librations are damped by means of a rotational spring-dashpot damper. In the present study the tether system was modeled with a two-bar model: the first bar represents the damper, the second the electrodynamic tether (see Fig. 2.1). This model have been already studied by Pelàez *et al.* and we here took advantage of it using the same method to find the equation of motions of the two-bar model [1]. Figure 2.1 depicts the orbital reference frame $Oxyz$ (unit vectors **i**,**j**,**k**): the x axis is along the local vertical pointing the space, the z axis lays on the orbital plane positively oriented with the instantaneous spacecraft velocity and the y axis completes the orthonormal frame. The orbit is supposed to be circular with radius equal to the semi-mayor axis a, thus with a mean motion:

$$\omega = \sqrt{\frac{\mu}{a^3}}$$

In-plane angles ϑ_1 and ϑ_2 define the attitude of the two bars in the orbit plane and the out-of-plane angles φ_1 and φ_2 define the angular displacements orthogonally the orbit plane. The physical model can be described as follows: a damper of mass m_1, a conductive tether of mass m_2 and an end mass m_B are attached to the spacecraft and the total length of the system is $L = L_1 + L_2$. The bars are assumed to be individually rigid and that their masses are negligible with respect to the spacecraft mass, thus the center of mass of the system is in O. Previous studies have shown that the main instabilities associated with the tether libration arise through a coupling between the in-plane and the out-of-plane tether motions with the system going eventually unstable in the orbit plane. For this reason, in the present work the tether dynamics has been studied by first analyzing the in-plane motion and later the 3D coupled dynamics. Although an analytical study was carried out through the linearization of the in-plane equations of motion only, it is worth pointing out that the damping device works on both the in-plane and out-of-plane oscillations and thus it can also take energy out of coupled oscillations like a tether skip-rope motion. Peláez *et al.* derived the equations of motion of the two-bar model taking into account the gravitational forces together with a simplified model of the Lorentz forces. In order to investigate the free vibration response of the damped two-bar model the electrodynamics terms were removed from the equations of motion. In turn, derivative and proportional terms of the damping device were added (i.e. a spring-dashpot model). To find the complete two-bar equations of motion the correct Lagrangian equation and generalized forces must be calculated.

2.1.1 Lagrangian equation

In this paragraph the method used to find the Lagrangian equation of the damped two-bar model is reported. The procedure is the same that was utlized by Peláez *et al.* in [2] and [1], thus we will just report the main passages.

With respect to the synodic frame depicted in Fig. 2.1, a point mass m orbiting the Earth is subjected to:

1. gravitational attraction of the Earth;
2. the inertial forces deriving from the non-Newtonian nature of the synodic frame;
3. all other external forces.

The gravitational force acting on m is conservative, thus they can be represented with the potentinal V_g. This can be linearized in the neighboorhood of the center O of the synodic frame:

$$V_g = -\omega^2 \left[a^2 - xa + \frac{(2x^2 - y^2 - z^2)}{2} \right] \tag{2.2}$$

where ω is the orbital frenquency, a is the circular orbit radius, and (x, y, z) are the cartesian coordinates in the synodic reference frame. Also the inertial forces can be obtained from a velocity-dependent potential [4]:

$$V_i = \gamma^0 \cdot \mathbf{x} - \frac{\|\omega \times \mathbf{x}\|^2}{2} - \omega \cdot (\mathbf{x} \times \dot{\mathbf{x}}) \tag{2.3}$$

where, for a circular orbit, $\gamma^0 = -\omega^2 a\mathbf{i}$ is the acceleration of the reference frame origin and $\omega = -\omega\mathbf{j}$ is orbital angular velocity. Equation (2.3) thus becomes:

$$V_i = -\omega^2 \frac{2ax + z^2 + x^2}{2} + \omega\left(z\dot{x} - x\dot{z}\right) \tag{2.4}$$

The generalized coordinates vector $\mathbf{q}$ of the two-bar system can be defined considering the damper and tether attitude angles:

$$\mathbf{q} = (\vartheta_1, \varphi_1, \vartheta_2, \varphi_2)$$

The four coordinates are independent and do not contain the time explicity. These two properties, together with the fact that the gravitational and inertia forces are conservative, makes the system to be a *natural system*. Thus, the kinetic energy of the point mass m can be expressed as follows:

$$T=\frac{1}{2}m\sum_{r=1}^{n}\sum_{s=1}^{n}\frac{\partial \mathbf{x}}{\partial q_r}\cdot\frac{\partial \mathbf{x}}{\partial q_s}\dot{q}_r\dot{q}_s \tag{2.5}$$

where $n=4$ is the dimension of $\mathbf{q}$ and $\mathbf{x}$ is the position of the point mass m expressed in the synodic reference frame. The cartesian coordinates of m can be expressend in function of the in-plane and out-of-plane angles, in particular for a point mass located generally along the first bar the position vector becomes

$$\mathbf{x^1}=\left(lc\varphi_1 c\vartheta_1,-ls\varphi_1,lc\varphi_1 s\vartheta_1\right),\ 0<l<L_1 \tag{2.6}$$

In turn, the position vector of a point mass located along the second bar (point B in Fig. 2.1) is

$$\mathbf{x^2}=\left(L_1 c\varphi_1 c\vartheta_1+lc\varphi_2 c\vartheta_2,-L_1 s\varphi_1-ls\varphi_2,L_1 c\varphi_1 s\vartheta_1+lc\varphi_2 s\vartheta_2\right),\ 0<l<L_2 \tag{2.7}$$

In the two previous equations following notations, which maintain valid throughout the document, have been introduced:

$$\begin{aligned}\sin x &= sx\\ \cos x &= cx\end{aligned} \tag{2.8}$$

Once the potential and the kinetic terms of a generic point mass have been expressed as functions of its position and velocity, the contributions to the Lagrangian equation of damper, tether, and tip mass can be expressed in function of the generalized coordinates vector $\mathbf{q}$ using expressions (2.4) and (2.5). Before proceeding with the Lagrangian components, we define the following four functions:

$$\check{V}_{g,i}\left(l\right)=\frac{1}{2}\omega^2\left[2alc\varphi_i c\vartheta_i+l^2\left(1-3c^2\vartheta_i c^2\varphi_i\right)\right] \tag{2.9}$$

$$\check{V}_{a,i}\left(l\right)=\frac{1}{2}\omega\left[-2al\omega c\varphi_i c\vartheta_i-l^2c^2\varphi_i\left(\omega+2\dot{\vartheta}_i\right)\right] \tag{2.10}$$

$$\check{T}_i\left(l\right)=\frac{1}{2}l^2\left(\dot{\varphi}_i^2+\dot{\vartheta}_i^2c^2\varphi_i\right) \tag{2.11}$$

$$\check{\mathcal{L}}_i\left(l\right)=\frac{1}{2}l^2\left[c^2\varphi_i\left(3\omega^2c^2\vartheta_i+\left(\omega+\dot{\vartheta}_i\right)^2\right)+\dot{\varphi}_i^2\right] \tag{2.12}$$

Equations (2.9)-(2.12) are expressions of specific energies, [J/kg]. They will be very useful in defining potential, kinetic, and Lagrangian equations in the following paragraphs.

Damper Taking into consideration a point mass m^1located along the first bar (i.e. the damper), after taking $\mathbf{x} = \mathbf{x^1}$, the gravitional potentials and kinetic terms becomes:

$$
\begin{aligned}
V_g^1 &= m^1 \check{V}_{g,1}(l) = \frac{1}{2} m^1 \omega^2 \left[2alc\varphi_1 c\vartheta_1 + l^2\left(1 - 3c^2\vartheta_1 c^2\varphi_1\right)\right] \qquad (2.13)\\
V_a^1 &= m^1 \check{V}_{a,1}(l) = \frac{1}{2} m^1 \omega \left[-2al\omega c\varphi_1 c\vartheta_1 - l^2 c^2\varphi_1\left(\omega + 2\dot{\vartheta}_1\right)\right] \qquad (2.14)\\
T^1 &= m^1 \check{T}_1(l) = \frac{1}{2} m^1 l^2 \left(\dot{\varphi}_1^2 + \dot{\vartheta}_1^2 c^2\varphi_1\right) \qquad (2.15)
\end{aligned}
$$

Note that the gravitational potential V_g^1 has been normalized so that it is null in the center O of the synodic frame, that is $V_g^1\,(l = 0) = 0$. The Lagrangian equation of m^1 can thus be calculated as $\mathcal{L}^1 = T^1 - V_g^1 - V_a^1$:

$$
\mathcal{L}^1 = m^1 \check{\mathcal{L}}_1(l) = \frac{1}{2} m^1 l^2 \left[c^2\varphi_1\left(3\omega^2 c^2\vartheta_1 + \left(\omega + \dot{\vartheta}_1\right)^2\right) + \dot{\varphi}_1^2\right] \qquad (2.16)
$$

To calculate the Lagrangian equation $\mathcal{L}_1$ of the first bar we must integrate Eq. (2.16) over the whole damper length:

$$
\begin{aligned}
\mathcal{L}_1 &= \frac{1}{2L_1} m_1 \int_0^{L_1} s^2 \left[c^2\varphi_1\left(3\omega^2 c^2\vartheta_1 + \left(\omega + \dot{\vartheta}_1\right)^2\right) + \dot{\varphi}_1^2\right] ds\\
&= \frac{1}{3} m^1 \check{\mathcal{L}}_1(L_1) = \frac{1}{6} m_1 L_1 \left[c^2\varphi_1\left(3\omega^2 c^2\vartheta_1 + \left(\omega + \dot{\vartheta}_1\right)^2\right) + \dot{\varphi}_1^2\right] \qquad (2.17)
\end{aligned}
$$

Tether Similarly to what was done in the previous paragraph, we now consider a point mass m^2 that is positioned along the second bar (i.e., the tether). Substituting $\mathbf{x} = \mathbf{x^2}$ in Eqs. (2.2), (2.4), and (2.5) the energy contributions of the generic mass can be found to be as follows:

$$
\begin{aligned}
V_g^2 &= m^2\left[\check{V}_{g,1}(L_1) + \check{V}_{g,2}(l)\right] +\\
&\quad + m^2\omega^2 L_1 l \left[\left(c\varphi_1 c\varphi_2\left(c\left(\vartheta_1 - \vartheta_2\right) - 3c\vartheta_1 c\vartheta_2\right) + s\varphi_1 s\varphi_2\right)\right] \qquad (2.18)\\
V_a^2 &= m^2\left[\check{V}_{a,1}(L_1) + \check{V}_{a,2}(l)\right] +\\
&\quad + m^2\omega L_1 l \left[s\left(\vartheta_1 - \vartheta_2\right)\left(s\varphi_1 c\varphi_2 \dot{\varphi}_1 - s\varphi_2 c\varphi_1 \dot{\varphi}_2\right) + \right.\\
&\quad \left. - c\left(\vartheta_1 - \vartheta_2\right) c\varphi_1 c\varphi_2 \left(\dot{\vartheta}_1 + \dot{\vartheta}_2 + \omega\right)\right] \qquad (2.19)\\
T^2 &= m^2\left[\check{T}_1(L_1) + \check{T}_2(l)\right] +\\
&\quad + m^2 L_1 l \left[c\left(\vartheta_1 - \vartheta_2\right) c\varphi_1 c\varphi_2 \dot{\vartheta}_1 \dot{\vartheta}_2 + \right.\\
&\quad + \left(c\varphi_1 c\varphi_2 + c\left(\vartheta_1 - \vartheta_2\right) s\varphi_1 s\varphi_2\right) \dot{\varphi}_1 \dot{\varphi}_2 +\\
&\quad \left. + s\left(\vartheta_1 - \vartheta_2\right)\left(c\varphi_1 s\varphi_2 \dot{\vartheta}_1 \dot{\varphi}_2 - c\varphi_2 s\varphi_1 \dot{\vartheta}_2 \dot{\varphi}_1\right)\right] \qquad (2.20)
\end{aligned}
$$

where $0 < l < L_2$. The Lagrangian equation of a point mass along the second bar can then be calculated as usal taking the difference between the kinetic energy and the potentials:

$$\begin{aligned}
\mathcal{L}^2 &= m^2\left[\check{\mathcal{L}}_1(L_1)+\check{\mathcal{L}}_2(l)\right]+\\
&\quad m^2L_1l\left[\omega^2\left(3c\vartheta_1c\vartheta_2c\varphi_1c\varphi_2-s\varphi_1s\varphi_2\right)+\right.\\
&\quad +c\left(\vartheta_1-\vartheta_2\right)c\varphi_1c\varphi_2\left(\omega\left(\dot{\vartheta}_1+\dot{\vartheta}_2\right)+\dot{\vartheta}_1\dot{\vartheta}_2\right)+\\
&\quad -s\left(\vartheta_1-\vartheta_2\right)s\varphi_1c\varphi_2\left(\omega+\dot{\vartheta}_2\right)\dot{\varphi}_1+\\
&\quad +s\left(\vartheta_1-\vartheta_2\right)s\varphi_2c\varphi_1\left(\omega+\dot{\vartheta}_1\right)\dot{\varphi}_2+\\
&\quad +\left(c\left(\vartheta_1-\vartheta_2\right)s\varphi_1s\varphi_2+c\varphi_1c\varphi_2\right)\dot{\varphi}_1\dot{\varphi}_2 \qquad (2.21)
\end{aligned}$$

Integrating $\mathcal{L}^2$ over the whole length of the second bar it is possible to find the Lagrangian equation of the second bar:

$$\begin{aligned}
\mathcal{L}_2 &= \frac{1}{L_2}\int_0^{L_2}\mathcal{L}^2(s)\,ds=\\
&= m_2\left[\check{\mathcal{L}}_1(L_1)+\frac{1}{3}\check{\mathcal{L}}_2(L_2)\right]+\\
&\quad \frac{1}{2}m_2L_1L_2\left[\omega^2\left(3c\vartheta_1c\vartheta_2c\varphi_1c\varphi_2-s\varphi_1s\varphi_2\right)+\right.\\
&\quad +c\left(\vartheta_1-\vartheta_2\right)c\varphi_1c\varphi_2\left(\omega\left(\dot{\vartheta}_1+\dot{\vartheta}_2\right)+\dot{\vartheta}_1\dot{\vartheta}_2\right)+\\
&\quad -s\left(\vartheta_1-\vartheta_2\right)s\varphi_1c\varphi_2\left(\omega+\dot{\vartheta}_2\right)\dot{\varphi}_1+\\
&\quad +s\left(\vartheta_1-\vartheta_2\right)s\varphi_2c\varphi_1\left(\omega+\dot{\vartheta}_1\right)\dot{\varphi}_2+\\
&\quad +\left(c\left(\vartheta_1-\vartheta_2\right)s\varphi_1s\varphi_2+c\varphi_1c\varphi_2\right)\dot{\varphi}_1\dot{\varphi}_2 \qquad (2.22)
\end{aligned}$$

where $\mathcal{L}^2(s)$ is found starting from Eq. (2.21) taking the substitution $l \to s$ and $m^2 \to m_2$.

Tip mass In the two-bar model the tip mass is modeled like a point mass positioned at the end of the second bar. It is possible to calculate its gravitational and kinetic contribution by substituting the position vector (2.7) into Eqs. (2.2), (2.4), and (2.5) taking $l = L_2$:

$$\begin{aligned}
V_g^B &= m_B\left[\check{V}_{g,1}(L_1) + \check{V}_{g,2}(L_2)\right] + \\
&\quad + m_B\omega^2 L_1 L_2 \left[\left(c\varphi_1 c\varphi_2\left(c(\vartheta_1 - \vartheta_2) - 3c\vartheta_1 c\vartheta_2\right) + s\varphi_1 s\varphi_2\right)\right] \qquad (2.23)\\
V_a^B &= m_B\left[\check{V}_{a,1}(L_1) + \check{V}_{a,2}(L_2)\right] + \\
&\quad + m_B\omega L_1 L_2\left[s(\vartheta_1 - \vartheta_2)\left(s\varphi_1 c\varphi_2\dot{\varphi}_1 - s\varphi_2 c\varphi_1\dot{\varphi}_2\right) + \right.\\
&\quad \left. - c(\vartheta_1 - \vartheta_2)c\varphi_1 c\varphi_2\left(\dot{\vartheta}_1 + \dot{\vartheta}_2 + \omega\right)\right] \qquad (2.24)\\
T^B &= m_B\left[\check{T}_1(L_1) + \check{T}_2(L_2)\right] + \\
&\quad + m_B L_1 L_2\left[c(\vartheta_1 - \vartheta_2)c\varphi_1 c\varphi_2\dot{\vartheta}_1\dot{\vartheta}_2 + \right.\\
&\quad + \left(c\varphi_1 c\varphi_2 + c(\vartheta_1 - \vartheta_2)s\varphi_1 s\varphi_2\right)\dot{\varphi}_1\dot{\varphi}_2 + \\
&\quad \left. + s(\vartheta_1 - \vartheta_2)\left(c\varphi_1 s\varphi_2\dot{\vartheta}_1\dot{\varphi}_2 - c\varphi_2 s\varphi_1\dot{\vartheta}_2\dot{\varphi}_1\right)\right] \qquad (2.25)
\end{aligned}$$

Thus, the Lagrangian contribution of the tip mass is:

$$\begin{aligned}
\mathcal{L}_B &= m_B\left[\check{\mathcal{L}}_1(L_1) + \check{\mathcal{L}}_2(L_2)\right] + \\
&\quad m_B L_1 L_2\left[\omega^2\left(3c\vartheta_1 c\vartheta_2 c\varphi_1 c\varphi_2 - s\varphi_1 s\varphi_2\right) + \right.\\
&\quad + c(\vartheta_1 - \vartheta_2)c\varphi_1 c\varphi_2\left(\omega\left(\dot{\vartheta}_1 + \dot{\vartheta}_2\right) + \dot{\vartheta}_1\dot{\vartheta}_2\right) + \\
&\quad - s(\vartheta_1 - \vartheta_2)s\varphi_1 c\varphi_2\left(\omega + \dot{\vartheta}_2\right)\dot{\varphi}_1 + \\
&\quad + s(\vartheta_1 - \vartheta_2)s\varphi_2 c\varphi_1\left(\omega + \dot{\vartheta}_1\right)\dot{\varphi}_2 + \\
&\quad + \left(c(\vartheta_1 - \vartheta_2)s\varphi_1 s\varphi_2 + c\varphi_1 c\varphi_2\right)\dot{\varphi}_1\dot{\varphi}_2 \qquad (2.26)
\end{aligned}$$

The complete Lagrangian equation Once the three Lagrangian contributions of damper, tether, and tip mass have been calculated the complete Lagrangian equation of the two-bar model is found by adding these three contributions:

$$\begin{aligned}
\mathcal{L} &= \mathcal{L}_1 + \mathcal{L}_2 + \mathcal{L}_B = \\
&= \frac{1}{6}\left(m_1 + 3(m_2 + m_B)\right)L_1^2\left[c^2\varphi_1\left(3\omega^2 c^2\vartheta_1 + \left(\omega + \dot{\vartheta}_1\right)^2\right) + \dot{\varphi}_1^2\right] + \\
&\quad + \frac{1}{6}(m_2 + 3m_B)L_2^2\left[c^2\varphi_2\left(3\omega^2 c^2\vartheta_2 + \left(\omega + \dot{\vartheta}_2\right)^2\right) + \dot{\varphi}_2^2\right] + \\
&\quad + \frac{1}{2}(m_2 + 2m_B)L_1 L_2\left\{c\varphi_1 c\varphi_2 c(\vartheta_2 - \vartheta_1)\left[\dot{\vartheta}_1\dot{\vartheta}_2 + \omega\left(\dot{\vartheta}_1 + \dot{\vartheta}_2\right)\right] + \right.\\
&\quad + s\left(\dot{\vartheta}_1 - \dot{\vartheta}_2\right)s\varphi_2 c\varphi_1\left(\omega + \dot{\vartheta}_1\right)\dot{\varphi}_2 - s\left(\dot{\vartheta}_1 - \dot{\vartheta}_2\right)s\varphi_1 c\varphi_2\left(\omega + \dot{\vartheta}_2\right)\dot{\varphi}_{1+} \\
&\quad + \left[c(\vartheta_1 - \vartheta_2)s\varphi_1 s\varphi_2 + c\varphi_1 c\varphi_2\right]\dot{\varphi}_1\dot{\varphi}_2 + \\
&\quad \left. + \omega^2\left(3c\vartheta_1 c\vartheta_2 c\varphi_1 c\varphi_2 - s\varphi_1 s\varphi_2\right)\right\} \qquad (2.27)
\end{aligned}$$

2.1.2 Damper viscous and elastic terms

The end mass is placed at the end of the tether. In a realistic mission scenario involving an electrodynamic tether system for deorbiting purposes the end mass is used to enhance the system stability by increasing the restoring gravitational forces and also for assisting the system deployment. However, in order to keep the deorbiting device competitive from a mass point of view, the end mass is usually much lighter than the spacecraft to be deorbited. Since the dissipated energy in a dashpot device is a function of the relative velocity between two bodies, the damper is thought to be installed on the spacecraft, whose attitude, considering its relative high inertia, can be assumed in a first-order analysis to be fixed with respect to the orbital frame. The rotational spring-dashpot device used in this work is modeled as a spherical damper [5]. The elastic contribution of the spherical damper is linearly proportional to the angle γ between the unit vector $\mathbf{i}$ and the unit vector $\mathbf{u_1}$ of the first bar:

$$\mathbf{u_1} = (c\varphi_1 c\vartheta_1, -s\varphi_1, c\varphi_1 s\vartheta_1) \tag{2.28}$$

The overall elastic torque tends to restore the position of the first bar along the local vertical (x axis), thus its direction is always perpendicular to the plane defined by vectors $\mathbf{i}$ and $\mathbf{u_1}$:

$$\mathbf{M_k} = k\gamma \frac{\mathbf{u_1} \times \mathbf{i}}{\|\mathbf{u_1} \times \mathbf{i}\|} = k f_k (\mathbf{u_1} \times \mathbf{i}) \tag{2.29}$$

where:

$$\mathbf{u_1} \times \mathbf{i} = (0, c\varphi_1 s\vartheta_1, s\varphi_1)$$

$$f_k(\vartheta_1, \varphi_1) = \frac{\gamma}{\sin\gamma} = \frac{\sin^{-1}(\|\mathbf{u_1} \times \mathbf{i}\|)}{\|\mathbf{u_1} \times \mathbf{i}\|} = \frac{\sin^{-1}\left(\sqrt{1 - c^2\vartheta_1 c^2\varphi_1}\right)}{\sqrt{1 - c^2\vartheta_1 c^2\varphi_1}}$$

The viscous torque component in a spherical damper is proportional to the instantaneous angular velocity (relative to the orbital frame) of the first bar and its direction is the opposite of that defined by the angular velocity vector. Consequently, the damping torque is simply:

$$\mathbf{M_b} = -b\mathbf{\Omega_1} \tag{2.30}$$

In Eqs. (2.29) and (2.30) b and k are the dimensional damping and elastic coefficients, with dimension $[kg \cdot m/s^2]$ and $[kg \cdot m^2/s^2]$ respectively. Equation (2.31) yields the first bar angular velocity $\mathbf{\Omega_1}$ with respect to the orbital frame:

$$\begin{aligned} \Omega_1 &= \mathbf{u_1} \times \dot{\mathbf{u}}_\mathbf{1} = \\ &= \left(s\vartheta_1\dot{\varphi}_1 - c\varphi_1 s\varphi_1 c\vartheta_1\dot{\vartheta}_1\right)\mathbf{i} - c^2\varphi_1\dot{\vartheta}_1\mathbf{j} - \left(c\vartheta_1\dot{\varphi}_1 + c\varphi_1 s\varphi_1 s\vartheta_1\dot{\vartheta}_1\right)\mathbf{k} \end{aligned} \tag{2.31}$$

Considering the very low torsional stiffness of long tethers, the motion about the longitudinal axis was neglected. Equation (2.32) defines the virtual work done by the generalized forces expressed in terms of the generalized coordinates:

$$dW = \mathbf{M} \cdot \mathbf{\Omega_1} dt = Q_{\vartheta_1} d\vartheta_1 + Q_{\varphi_1} d\varphi_1 \tag{2.32}$$

Thus, the generalized forces associated with the proportional and derivative terms of the damping system are computed by means of Eqs. (2.33) and (2.34) and then added to the right-hand side of the equations of motion (see Par. 2.1.3):

$$\begin{aligned} Q_{b,q_i} &= \mathbf{M_b} \cdot \frac{\partial \mathbf{\Omega_1}}{\partial \dot{q}_i} = -\frac{b}{2} \frac{\partial \left\| \mathbf{\Omega_1} \right\|^2}{\partial \dot{q}_i} & (2.33) \\ Q_{k,q_i} &= \mathbf{M_k} \cdot \frac{\partial \mathbf{\Omega_1}}{\partial \dot{q}_i} = k f_k \left(\mathbf{u_1} \times \mathbf{i} \right) \cdot \frac{\partial \mathbf{\Omega_1}}{\partial \dot{q}_i} & (2.34) \end{aligned}$$

The in-plane and out-of-plane components of the viscous terms are:

$$\begin{aligned} Q_{b,\vartheta_1} &= -bc^2 \varphi_1 \dot{\vartheta}_1 \\ Q_{b,\varphi_1} &= -b\dot{\varphi}_1 \end{aligned} \tag{2.35}$$

The same components of the elastic terms are:

$$\begin{aligned} Q_{k,\vartheta_1} &= -k f_k s\vartheta_1 c\varphi_1 \\ Q_{k,\varphi_1} &= -k f_k s\varphi_1 c\vartheta_1 \end{aligned} \tag{2.36}$$

2.1.3 Equations of motion

The Lagrangian equations that describe the dynamic of the damped two-bar model are shown in Eqs. (2.38)–(2.41). They have been written in a more compact non-dimensional form making use of the non-dimensional parameters defined in the Nomenclature at the beginning of this Chapter. Briefly, the equations of motion were first obtained in dimensional form starting from the undamped two-bar Lagrangian function by adding the terms listed in Eqs. (2.35) and (2.36) to the right hand side of the equations:

$$\frac{d}{dt}\left(\frac{\partial \mathcal{L}}{\partial \dot{q}_i}\right) - \frac{\partial \mathcal{L}}{\partial q_i} = Q_{b,q_i} + Q_{k,q_i} \tag{2.37}$$

The four equations thus obtained are very long and not easy to deal with. We can partially remedy to this fact manipulating them algebrically with the aim to reduce their length and presente them in a more intelligible form. First, the non-dimensional time is adopted in the derivative terms such as:

$$\frac{dx}{dt} = \omega \frac{dx}{d\tau}, \; \frac{d^2x}{dt^2} = \omega^2 \frac{d^2x}{dt^2}$$

At this point, it is possible to substitute all dimensional mass and geometry parameters with their non-dimensional equivalent (i.e., δ_i and Λ factors). Subsequentially, the equations relative to first and second bar are divided for the common factors $\omega^2 m_B \Lambda L^2$ and $\omega^2 m_B (1-\Lambda) L^2$, respectively. These three passages are sufficient to make the equations of motion non-dimensional, nevertheless it will turn out to be much useful to carry on one last passage, that is to group together all similar geometry and mass factors by means the A, B, D, and E parameters. In this manner the equations of motion of the damped two-bar model assume a shorter and a little bit more handy form. Moreover, all these measures will be useful in the subquent analytical study. At last, note that from now on also the damping and the elastic coefficients assume non-dimensional form taking advantage of β and κ coefficients. Concluding, the four equations of motion are reported in the following paragraphs.

Equation of motion relative to the first bar, in-plane dynamics

$$
\begin{aligned}
A c\varphi_1 \vartheta_1^{''} &+ \frac{3}{2} B c\left(\vartheta_1-\vartheta_2\right) c\varphi_2 \vartheta_2^{''} + \frac{3}{2} B s\left(\vartheta_1-\vartheta_2\right) s\varphi_2 \varphi_2^{''} \\
&- 2 A s\varphi_1 \varphi_1^{'}\left(1+\vartheta_1^{'}\right) - 3 B c\left(\vartheta_1-\vartheta_2\right) s\varphi_2 \varphi_2^{'}\left(1+\vartheta_2^{'}\right) \\
&+ \frac{3}{2} B s\left(\vartheta_1-\vartheta_2\right) c\varphi_2\left(\vartheta_2^{'2}+2\vartheta_2^{'}+\varphi_2^{'2}\right) \\
&+ 3 s\vartheta_1\left(A c\vartheta_1 c\varphi_1+\frac{3}{2} B c\vartheta_2 c\varphi_2\right) + 3\left(\beta c\varphi_1 \vartheta_1^{'} + \kappa f_k s\vartheta_1\right) = 0
\end{aligned}
\tag{2.38}
$$

Equation of motion relative to the first bar, out-of-plane dynamics

$$
\begin{aligned}
A\varphi_1^{''} &+ \frac{3}{2} B\left[c\varphi_1 c\varphi_2 + c\left(\vartheta_1-\vartheta_2\right) s\varphi_1 s\varphi_2\right]\varphi_2^{''} \\
&- \frac{3}{2} B s\left(\vartheta_1-\vartheta_2\right) s\varphi_1 c\varphi_2 \vartheta_2^{''} + 3 B s\left(\vartheta_1-\vartheta_2\right) s\varphi_1 s\varphi_2 \varphi_2^{'}\left(1+\vartheta_2^{'}\right) \\
&+ A s\varphi_1 c\varphi_1 \vartheta_1^{'}\left(2+\vartheta_1^{'}\right) + \frac{3}{2} B c\left(\vartheta_1-\vartheta_2\right) s\varphi_1 c\varphi_2\left(\vartheta_2^{'2}+2\vartheta_2^{'}+\varphi_2^{'2}\right) \\
&- \frac{3}{2} B s\varphi_2 c\varphi_1 \varphi_2^{'2} + c\varphi_1\left(\frac{3}{2} B s\varphi_2 + A s\varphi_1\right) \\
&+ 3 s\varphi_1 c\vartheta_1\left(A c\vartheta_1 c\varphi_1+\frac{3}{2} B c\vartheta_2 c\varphi_2\right) + 3\left(\beta c\varphi_1 \varphi_1^{'} + \kappa f_k c\vartheta_1 s\varphi_1\right) = 0
\end{aligned}
\tag{2.39}
$$

Equation of motion relative to the second bar, in-plane dynamics

$$\begin{aligned}
&Ec\varphi_2\vartheta_2^{''} - \frac{3}{2}Dc\left(\vartheta_1 - \vartheta_2\right)c\varphi_1\vartheta_1^{''} + \frac{3}{2}Ds\left(\vartheta_1 - \vartheta_2\right)s\varphi_1\varphi_1^{''} \\
&\quad - 2Es\varphi_2\varphi_2^{'}\left(1 + \vartheta_2^{'}\right) + 3Dc\left(\vartheta_1 - \vartheta_2\right)s\varphi_1\varphi_1^{'}\left(1 + \vartheta_1^{'}\right) \\
&\quad + \frac{3}{2}Ds\left(\vartheta_1 - \vartheta_2\right)c\varphi_1\left(\vartheta_1^{'2} + 2\vartheta_1^{'} + \varphi_1^{'2}\right) \\
&\quad + 3\left(Es\vartheta_2c\vartheta_2c\varphi_2 + \frac{3}{2}Ds\vartheta_2c\vartheta_1c\varphi_1\right) = 0 \qquad (2.40)
\end{aligned}$$

Equation of motion relative to the second bar, out-of-plane dynamics

$$\begin{aligned}
&E\varphi_2^{''} - \frac{3}{2}D\left[c\varphi_1c\varphi_2 + c\left(\vartheta_1 - \vartheta_2\right)s\varphi_1s\varphi_2\right]\varphi_1^{''} \\
&\quad - \frac{3}{2}Ds\left(\vartheta_1 - \vartheta_2\right)c\varphi_1s\varphi_2\vartheta_1^{''} + 3Ds\left(\vartheta_1 - \vartheta_2\right)s\varphi_1s\varphi_2\varphi_1^{'}\left(1 + \vartheta_1^{'}\right) \\
&\quad - \frac{3}{2}Dc\left(\vartheta_1 - \vartheta_2\right)c\varphi_1s\varphi_2\left(\vartheta_1^{'2} + 2\vartheta_1^{'} + \varphi_1^{'2}\right) \\
&\quad + Es\varphi_2c\varphi_2\left[3c^2\vartheta_2 + \left(1 + \vartheta_2^{'}\right)^2\right] + \frac{3}{2}Ds\varphi_1c\varphi_2\left(\varphi_1^{'2} - 1\right) \\
&\quad - \frac{9}{2}Dc\vartheta_1c\varphi_1c\vartheta_2s\varphi_2 = 0 \qquad (2.41)
\end{aligned}$$

2.2 Analytical study

The equations of motion of the two-bar model are strongly non-linear, as it can be seen by inspection of Eqs. (2.38)-(2.41). For this reason, it is not possible to carry out an analytically study on the complete equations of motion (i.e., the 3D case). To enable it, it is necessary to reduce the two-bar dynamics to a bi-dimensional case and linearize the equations. As it was already stated in the previous sections, when we deal with electrodynamic tethers it has been highligthed that the main instabilities associated with the tether libration cause the system to go eventually unstable (i.e., libration amplitude growing more and more) in the orbit plane. Thus, the in-plane dynamics was selected to study, in a first stage, the behaviour of the damped two-bar model. For the sake of completeness the same study was conducted also on the out-of-plane dynamics, returning very similar results as in the in-plane case. For this reason the out-of-plane case (2D case) will not be treated in this work. In turn, the out-of-plane dynamics was obviously taking into account in the numerical study considering the complete dynamics equations (2.38)-(2.41).

2.2.1 In-plane linearized equations

The in-plane equations of the damped two bar model can be found by setting the out-of-plane angles (and their derivatives) to zero, that is $\varphi_i = \varphi_i^{'} = \varphi_i^{''} = 0$, $i =$

$1, 2$. Equations (2.42) and (2.43) can then be referred as the *in-plane equations*:

$$\begin{aligned} &A\vartheta_1'' + \frac{3}{2}Bc\left(\vartheta_1 - \vartheta_2\right)\vartheta_2'' + \frac{3}{2}Bs\left(\vartheta_1 - \vartheta_2\right)\vartheta_2'\left(2 + \vartheta_2'\right) \\ &\quad + 3s\vartheta_1\left(Ac\vartheta_1 + \frac{3}{2}Bc\vartheta_2\right) + 3\left(\beta\vartheta_1' + \kappa\vartheta_1\right) = 0 \end{aligned} \tag{2.42}$$

$$\begin{aligned} &E\vartheta_2'' - \frac{3}{2}Dc\left(\vartheta_1 - \vartheta_2\right)\vartheta_1'' + \frac{3}{2}Ds\left(\vartheta_1 - \vartheta_2\right)\vartheta_1'\left(2 + \vartheta_1'\right) \\ &\quad + 3\left(Es\vartheta_2 c\vartheta_2 + \frac{3}{2}Ds\vartheta_2 c\vartheta_1\right) = 0 \end{aligned} \tag{2.43}$$

Equations (2.42) and (2.43) are associated with the corrispective 3D equations of motion (2.38) and (2.40), whereas equations (2.39) and (2.41) do not enter in the linearized study since they describe the out-of-plane dynamics. In order to obtain a set of two linear second-order differential equations Eqs. (2.42) and (2.43) must be linearized about the local vertical ($\vartheta_1 = \vartheta_2 = 0$). Thus, the *linearized in-plane equations* for small oscillations are found to be as follows:

$$\begin{cases} \vartheta_1'' + \eta E\left[\beta\vartheta_1' + \left(A + \dfrac{3}{2}B + \kappa\right)\vartheta_1 + \dfrac{3B}{4E}\left(3D - 2E\right)\vartheta_2\right] = 0 \\ \vartheta_2'' + \dfrac{3}{2}\eta D\left[\beta\vartheta_1' + \left(A + \dfrac{3}{2}B + \kappa\right)\vartheta_1 + \dfrac{A}{3D}\left(2E - 3D\right)\vartheta_2\right] = 0 \end{cases} \tag{2.44}$$

The linearized damper contributions were obtained by linearizing the expressions of Q_{b,ϑ_1} and Q_{k,ϑ_1} in Eqs. (2.35) and (2.36) considering that:

$$\lim_{(\vartheta_1,\varphi_1)\to\mathbf{0}} f_k = \lim_{\gamma\to 0}\frac{\gamma}{\sin\gamma} = 1$$

An inspection of Eq. (2.44) shows a coupling between the dynamics of the two bars. This coupling accounts for a continuous exchange of energy between the two bars that can be exploited by the damper. The goal then is to search for the pair of values (β^*, κ^*) that maximizes the transfer of kinetic energy from the tether to the damper where the energy is dissipated.

2.2.2 System stability and eigenfrequencies

The set of equations (2.44) can be analytically solved by means of Laplace transform thus enabling the investigation of how the damping and elastic coefficients affect the natural frequencies and the stability of the damped two-bar system. Taking the Laplace transform of the set of equations (2.44) yields:

$$\begin{bmatrix} s^2 + E\left(\beta_1 s + \kappa_1\right) & -\dfrac{3}{4}B\kappa_2 \\ \dfrac{3}{2}D\left(\beta_1 s + \kappa_1\right) & s^2 + \dfrac{A}{2}\kappa_2 \end{bmatrix}\begin{pmatrix}\Theta_1 \\ \Theta_2\end{pmatrix} = \mathbf{v} \tag{2.45}$$

where:

$$\kappa_1 = \eta\left(A + \frac{3}{2}B + \kappa\right),\ \kappa_2 = \eta\left(2E - 3D\right),\ \beta_1 = \eta\beta$$

and $\mathbf{v} = \mathbf{v}\left(\vartheta_{10}, \vartheta_{20}, \vartheta_{10}^{'}, \vartheta_{20}^{'}\right)$ is a constant terms vector. In order to study the system dynamic response the eigenvalues of the coefficients matrix in (2.45) must be evaluated by setting its determinant equal to zero:

$$det = s^4 + E\beta_1 s^3 + \left(E\kappa_1 + \frac{A}{2}\kappa_2\right)s^2 + \frac{3}{2\eta}\beta_1\kappa_2 s + \frac{3}{2\eta}\kappa_1\kappa_2 = 0 \tag{2.46}$$

The resulting polynomial is a quartic function that can be solved analytically. Before doing that, we can study the stability of the system taking advantage of Routh–Hurwitz stability criterion.

Asymptotic stability: the critical elastic coefficient The Routh-Hurwitz tabular matrix relative to the polynomial (2.46) can be built as follows:

$$\left|\begin{array}{ccc} 1 & E\kappa_1 + \frac{A}{2}\kappa_2 & \frac{3}{2\eta}\kappa_1\kappa_2 \\ E\beta_1 & \frac{3}{2\eta}\beta_1\kappa_2 & 0 \\ \Delta_{11} & \Delta_{12} & \\ \Delta_{21} & & \\ \Delta_{12} & & \end{array}\right. \tag{2.47}$$

where

$$\begin{aligned} \Delta_{11} &= E\kappa_1 + \frac{\kappa_2}{2}\left(A - \frac{3}{E\eta}\right) \\ \Delta_{12} &= \frac{3}{2\eta}\kappa_1\kappa_2 \\ \Delta_{21} &= \frac{3}{2\eta}\beta_1\kappa_2 - E\beta_1\frac{\Delta_{12}}{\Delta_{11}} \end{aligned}$$

The Routh-Hurwitz stability criterion states that if all elements of the first column of matrix (2.47) have the same sign, then the system associated with determinant (2.46) is asymptotically stable. After some manipulation and several algebric passages, it is possible to state that:

> *the linear time invariant system described by the set of equations* (2.44) *is asymptotically stable if* $\kappa_1 > 0$.

More precisely, the system is asymptotically stable if the damper elastic coefficientκ is greater than a particular value called *critical elastic coefficient* κ_{cr}. Ultimately, the condition of asymptotic stability is defined by the following condition (2.48):

$$\kappa > \kappa_{cr} = -\left(A + \frac{3}{2}B\right) = -\left[3 + \Lambda\delta_1 + \frac{\delta_2}{2}(3 - \Lambda)\right] \tag{2.48}$$

By inspection of (2.48) it is possible to state that κ_{cr} is always negative:

$$\kappa_{cr} < 0 \tag{2.49}$$

In other words, Eq. (2.48) tells us that, to have a stable system, we could choose a negative value of the elastic coefficient, provided that it is still greater than κ_{cr}. At a first glance this fact could raise some doubts: what does negative elastic coefficient means? And why doesn't it lead the system to immediate instability? The answer is actually simple: the value of κ_{cr} is negative unlike in a classical spring-dashpot system, for which negative values of the elastic coefficient imply instability, because the term $\kappa\vartheta_1$ in Eq. (2.44) is not the only restoring force acting on the two-bar system. The total restoring force is indeed a sum of terms associated with the gravitational gradient (i.e., the tether tension) and the spring elastic coefficient of the damper. Virtually, we could define a *system total elastic coefficient*

$$\kappa_{tot} = A + \frac{3}{2}B + \kappa \tag{2.50}$$

where the parameters A and B, defined in the Nomenclature, are positive by definition and are associated with the gravitational gradient. It is worth to point out that, from a quick inspection of A and B, it is possible to state that the absolute value of κ_{cr} increases when the system mass parameters as well as the overall tether length L increase.

System eigenvalues Concerning the nature of the system eigenvalues, in general there are two cases of interest [4]. In the first case there are two solutions which are complex conjugates of each other:

$$\begin{aligned} s_{1,2} &= \alpha_1 \pm i\omega_1 \\ s_{3,4} &= \alpha_2 \pm i\omega_2 \end{aligned}$$

We may refer to this case as *underdamped* case. In the second case there are two real solutions and two complex conjugates solutions:

$$\begin{aligned} s_{1,2} &= \alpha_1 \pm i\omega_1 \\ s_3 &= \alpha_{21} \\ s_4 &= \alpha_{22} \end{aligned}$$

We refer to the second case as *overdamped* case. More in general, solving the fourth-order polynomial (2.46) yields the eigenvalues of the system:

$$\begin{aligned} s_{1,2} &= U + \sqrt{T+S} \pm \sqrt{2T - S + \frac{R}{\sqrt{T+S}}} \\ s_{3,4} &= U - \sqrt{T+S} \pm \sqrt{2T - S - \frac{R}{\sqrt{T+S}}} \end{aligned} \tag{2.51}$$

where R, S, T, and U are constants that are functions of the system mass and geometry properties and also of the damping and elastic coefficients. Unluckily, these constants are far too complex to allow an analytical evaluation of the roots (see the Appendix of [4] for an explicit formulation). Nonetheless, after several algebraic manipulations and with the aid of a computational software program we found results of general validity as reported in the following. Note that the results reported below are valid for every pair of $(\beta, \kappa) \in I \subset \mathbb{R}^2$ with $\beta > 0$ and $\kappa > \kappa_{cr}$.

1. For all solutions described in Eq. (2.51) the real part is $U \pm \sqrt{T+S}$ whereas the imaginary part is $\sqrt{2T - S \pm \frac{R}{\sqrt{T+S}}}$.
2. The real parts associated with both the first eigenfrequency ($s_{1,2}$) and the second eigenfrequency ($s_{3,4}$) are always negative. This fact is another proof that *the damped two-bars system is asymptotically stable for any pair of* $(\beta, \kappa) \in I$.
3. The imaginary part $i\omega_1 = \sqrt{2T - S + \frac{R}{\sqrt{T+S}}}$ is practically always equal to $\sqrt{3}$ and is equal to the first in-plane librational natural frequency ω_1 (adimensionalized by the orbital rate ω) as found by Peláez *et al.* [1, 2]:
$$\omega_1 \cong \sqrt{3}\; \forall\, (\beta, \kappa) \in I$$
4. The quantity $\sqrt{2T - S - \frac{R}{\sqrt{T+S}}}$ represents the (nondimensional) second natural frequency of the system, ω_2. For a given value of the elastic coefficient κ there exists a value of the damping coefficient, the *critical damping coefficient* β_{cr}, above which ω_2 disappears and the quantity above becomes real. The value of β_{cr} depends on the mass and geometric system characteristics and the elastic coefficient:
$$\sqrt{2T - S - \frac{R}{\sqrt{T+S}}} \in \mathbb{R}\; for\; \beta > \beta_{cr}\,(\delta_1, \delta_2, \Lambda, \kappa)$$
5. As it was mentioned above, similarly to what happens in a classic spring-dashpot system, for values of the damping coefficient lower than the critical one we can say that the system is *underdamped*. If the damping coefficient is higher than β_{cr} the system will be *overdamped*.

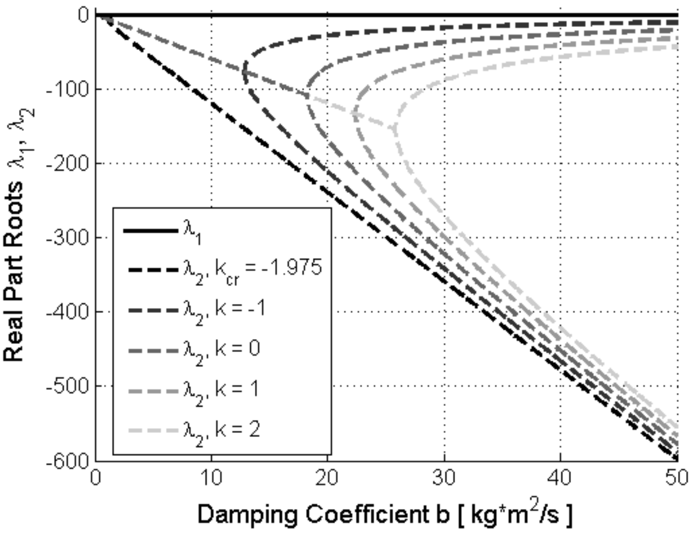

Figure 2.2: Eigenvalues real part as a function of the damping coefficient.

6. For given values of the system mass and geometric parameters along with the elastic coefficient, the second natural frequency ω_2 is a function of the damping coefficient: it decreases from a maximum value $\omega_{20} = \omega_2(0)$ down to $\omega_2(\beta_{cr}) = 0$ for $\beta = \beta_{cr}$.

By means of Eq. (2.51) it is possible to evaluate numerically the trends of real and imaginary parts of the system eigenvalues and thus investigate the system stability and natural frequencies. To do this we assigned to the mass and geometry parameters typical values, that is, $L_1 = 10m$, $L_2 = 3000m$, a damper mass equal to $1kg$ and a tether mass of $4kg$. Figure 2.2 shows the real parts of the system eigenvalues as a function of b for different values of k utlizing dimensional damper parameters. The first eigenvalue real part α_1 is very small compared to α_2, thus only one curve were included. See Fig. 2.3 for a more detailed plot of α_1 trends. Note that for $b \geq b_{cr}$, α_2 splits in two real components α_{21} and α_{22}. The first important result that must be pointed out here is that for any $b > 0$ all the real parts are negative (α_1 is also negative even though much close to zero). As it was stated above, this fact let us infer that the damped two-bar model is always asymptotically stable. Concerning the system eigenfrequencies, Figure 2.4 shows the imaginary parts as a function of b. Note that the first natural frequency ω_1 is always equal to $\sqrt{3}$ for any value of the damping coefficient, whereas ω_2 decreases for increasing values of b and becomes null at b_{cr}. For increasing values of the elastic coefficient the critical damping coefficient increases and, with it, the second natural frequency ω_{20}.

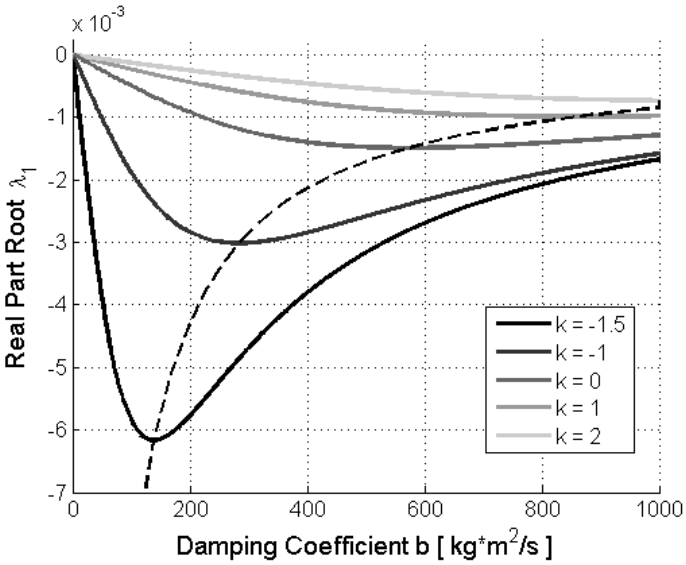

Figure 2.3: First mode of vibration decay constant in function of the damping coefficient. The dashed line fits the maximum (in absolute value) values of λ_1 for different values of the elastic coefficient.

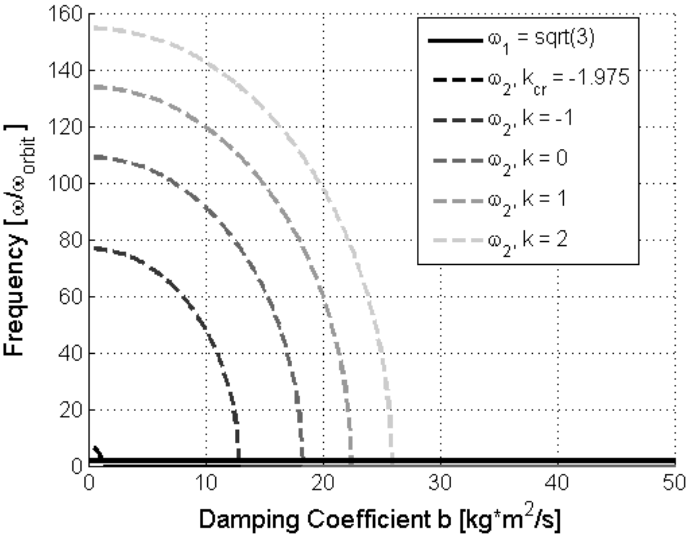

Figure 2.4: Eigenvalues imaginary part (natural frequencies) as a function of the damping coefficient.

2.2.3 Analytical solution and damper optimization

The set of differential equations (2.44) was solved by means of Laplace transform. In order to study the system energy trends it was decided in the present work to perturb the equilibrium position of the two-bar system (i.e., the local vertical) by adopting an initial angular velocity $\dot{\vartheta}_{20} \neq 0$. Considering this, the solutions of Θ_1 and Θ_2 in the frequency domain are found as follows [with $\mathbf{v} = \left(0, \dot{\vartheta}_{20}\right)$]:

$$\begin{cases} \Theta_1(s) = & \dfrac{3B\kappa_2}{4\,det}\dot{\vartheta}_{20} \\ \Theta_2(s) = & \dfrac{s^2 + E\beta_1 s + E\kappa_1}{det}\dot{\vartheta}_{20} \end{cases} \tag{2.52}$$

After some manipulations, the solutions can be rewritten in the compact form:

$$\begin{cases} \Theta_1(s) = \dfrac{3}{4}B\kappa_2\dot{\vartheta}_{20}\displaystyle\sum_{i=1}^{4}\left[\frac{1}{(s-s_i)}\cdot\prod_{j=1}^{4}\frac{1}{(s_i-s_j)}\right] \\ \Theta_2(s) = \vartheta_{20}\displaystyle\sum_{i=1}^{4}\left[\frac{s_i^2 + Es_i\beta_1 + E\kappa_1}{(s-s_i)}\cdot\prod_{j=1}^{4}\frac{1}{(s_i-s_j)}\right] \\ \qquad j \neq i \end{cases} \tag{2.53}$$

Equations (2.53) were rewritten in a convenient form to calculate their Laplace anti-transform. Thus, taking the anti-transform we get the solutions of the damped two-bar model in the time domain:

$$\begin{cases} \vartheta_1(\tau) = \dfrac{3}{4}B\kappa_2\dot{\vartheta}_{20}\displaystyle\sum_{i=1}^{4}\left[e^{s_i\tau}\cdot\prod_{j=1}^{4}\frac{1}{(s_i-s_j)}\right] \\ \vartheta_2(\tau) = \dot{\vartheta}_{20}\displaystyle\sum_{i=1}^{4}\left[e^{s_i\tau}\left(s_i^2 + Es_i\beta_1 + E\kappa_1\right)\prod_{j=1}^{4}\frac{1}{(s_i-s_j)}\right] \\ \qquad j \neq i \end{cases} \tag{2.54}$$

The real parts of solution s_3 and s_4 are always negative and it is true that $|\Re(s_{3,4})| \gg |\alpha_1|$ for every $\beta > 0$. For this reason the contribution associated with the exponential terms $e^{s_{3,4}}$ can be safely neglected without loss of accuracy. Thus, after many further manipulations it is possible to obtain the in-plane linearized solutions of the damped two-bar model in the form as in the following Eq. (2.55):

$$\begin{cases} \vartheta_1(\tau) = & A_{11}e^{\alpha_1\tau}\sin(\omega_1\tau + \xi_{11}) \\ \vartheta_2(\tau) = & A_{21}e^{\alpha_1\tau}\sin(\omega_1\tau + \xi_{21}) \end{cases} \tag{2.55}$$

In an overdamped system, that is the case of interest in this study, we have:

$$\begin{aligned}
A_{11} &= \frac{3}{4}\frac{\dot{\vartheta}_{20}}{\omega_1}B\kappa_2 \cdot \sqrt{\frac{1}{Q_1}} \\
A_{21} &= \frac{\dot{\vartheta}_{20}}{\omega_1} \cdot \sqrt{\frac{P_1}{Q_1}} \\
\xi_{11} &= -\tan^{-1}\left(\frac{(\alpha_{21}-\alpha_1)(\alpha_1-\alpha_{22})+\omega_1^2}{(\alpha_{21}+\alpha_{22}-2\alpha_1)\,\omega_1}\right) \\
\xi_{21} &= -\tan^{-1}\left(\frac{P_2}{Q_2}\right)
\end{aligned}$$

where

$$\begin{aligned}
P_1 &= \left[\alpha_1^2 + E(\alpha_1\beta_1+\kappa_1)+\omega_1^2\right]^2 + \left(E^2\beta_1^2 - 4E\kappa_1\right)\omega_1^2 \\
Q_1 &= \left[(\alpha_1-\alpha_{21})^2+\omega_1^2\right]\cdot\left[(\alpha_1-\alpha_{22})^2+\omega_1^2\right] \\
P_2 &= (\alpha_1-\alpha_{21})(\alpha_1-\alpha_{22})\left(\alpha_1^2+E\alpha_1\beta_1+E\kappa_1\right)+2\alpha_1^2 \\
&\quad -\alpha_1(\alpha_{21}+\alpha_{22}-E\beta_1)-\alpha_{21}(\alpha_{22}+E\beta_1)-E(\alpha_{22}\beta_2+\kappa_1) \\
Q_2 &= \omega_1\left[\alpha_1^2(\alpha_{21}+\alpha_{22}+E\beta_1)+2\alpha_1(E\kappa_1-\alpha_{21}\alpha_{22})\right. \\
&\quad \left.-E(\alpha_{21}\alpha_{22}\beta_1+\kappa_1(\alpha_{21}+\alpha_{22}))+(\alpha_{21}+\alpha_{22}+E\beta_1)\,\omega_1^2\right]
\end{aligned}$$

With the aid of numerical analysis it is possible to demonstrate that all coefficients appearing in Eq. (2.55), with the only exception of α_1, are essentially independent of the damping and elastic coefficients β and κ. In Eq. (2.55), α_1 is the decay constant of the first mode of vibration system that determines the relaxation time of the damped oscillation $\hat{\tau} = |1/\alpha_1|$. In other words, the more negative α_1 is the quicker the oscillation damps out. The decay constant is strongly dependent on the damping and elastic coefficients:

$$\alpha_1 = U + \sqrt{T+S} = f_1(\delta_1, \delta_2, \Lambda, \beta, \kappa) \tag{2.56}$$

This fact provides an opportunity to control its value through the values of β and κ. Specifically, given a certain value of the elastic coefficient κ, we can analyze the partial derivative of Eq. (2.56) with respect to the damping coefficient and look for a global minimum of the function (see Appendix in [5] for the explicit formulation):

$$\frac{\partial\alpha_1}{\partial\beta} = U + \sqrt{T+S} + \frac{\dot{S}}{2\dot{U}} = f_2(\delta_1, \delta_2, \Lambda, \beta^*, \kappa) = 0 \tag{2.57}$$

Equation (2.57) was analyzed to find that a value β^* does exist and is unique in $\mathbb{R}^+$. Figure 2.5 shows the trend of the decay constant as function of β and κ obtained by solving Eq. (2.57) for several values of κ. The black dashed line in

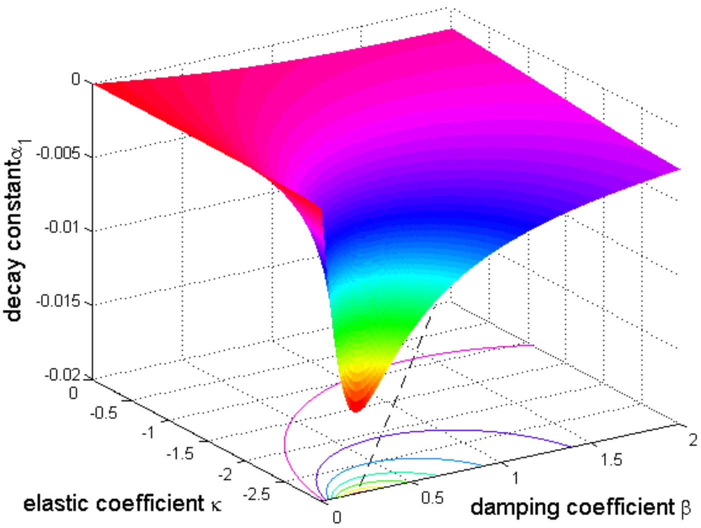

Figure 2.5: Decay constant as a function of non-dimensional damping and elastic coefficients. The black dashed line fits the points defined by the pairs of (β^*, κ) values.

the figure fits the points defined by the pairs of (β^*, κ) values. Figure 2.5 shows that higher (in absolute value) decay constant values are obtained for negative elastic coefficients, hence the more negative the value of κ the higher α_1. These considerations let us to conclude that tether oscillations are damped out faster for negative values of k with the relaxation time vanishing as k tends to k_{cr} (see Fig. 2.6). However, the negative value of κ cannot be decreased at will because the damper dynamics becomes unstable when $\kappa \leq \kappa_{cr}$. Thus, it is true that the optimal κ is

$$\kappa^* = \lim_{\kappa \to \kappa_{cr}^+} \kappa$$

but for κ very close or equal to κ_{cr} the system becomes unstable independently of the value of β. This means that the best dissipation is indeed attained for negative values of κ which are slightly higher (less negative) than κ_{cr}. Consequently, the best (β^*, κ) pair is a tradeoff between dissipation efficiency and dynamics stability requirements. Figure 2.7 shows the trends of b^* and b_{cr} as functions of the elastic coefficient. Note that the optimized system is always overdamped (see the damping ratio curve ζ in Fig. 2.7).

As a further proof of the positive effects of a damper device in a two-bar model, Fig. 2.8 shows that the adoption of an optimal damping coefficient yields the fastest relaxation time. In fact, the solid black line in the figure is associated with $b = b^*$ and, being the steepest curve, it implies that the system is damped in the quickest time. Moreover, Fig. 2.9 shows how the elastic coefficient affects the damping mechanism. As it was already stated above, the more negative k the faster the damping of oscillations. The fastest damping occurs for $k = k^* \cong$

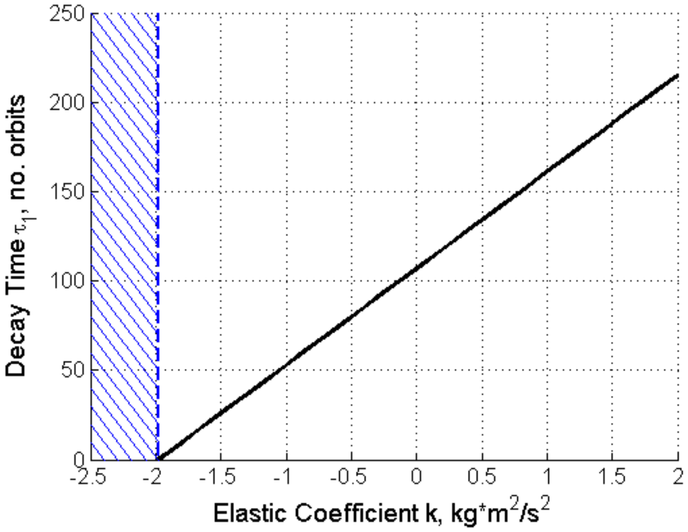

Figure 2.6: Oscillation relaxation time as a function of the elastic coefficient. The instability area (blue striped area) marks the $k \leq k_{cr}$ zone. For the case taken into account in this paper $k_{cr} \cong -1.975$.

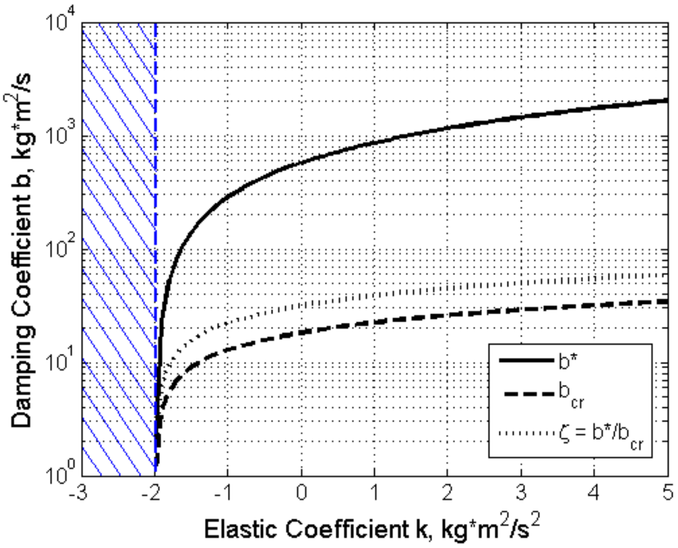

Figure 2.7: Optimal and critical damping coefficients as functions of the elastic coefficient. The ζ curve represents the damping ratio between optimal and critical damping coefficients.

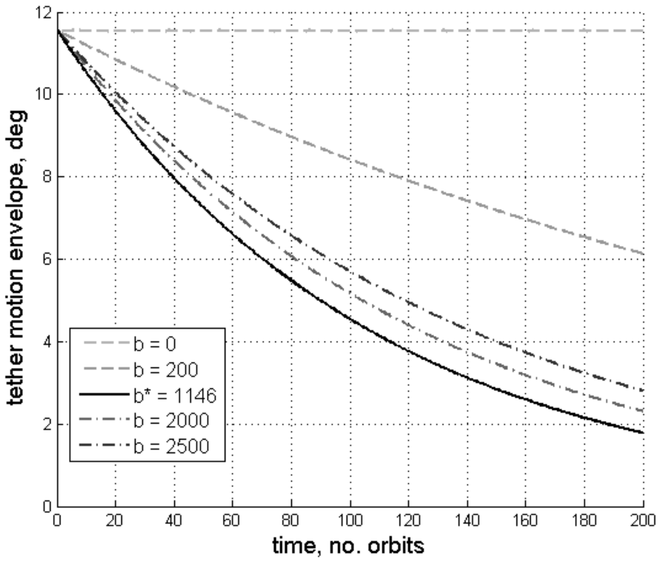

Figure 2.8: Tether oscillation decay envelopes for different values of the damping coefficient assuming $k = 0$.

$-1.975\, kg \cdot m^2/s^2$ (actually for a value slightly higher than k^* to avoid damper instability). Note that the curves in Fig. 2.9 refer to the optimized cases where the optimal values of b were found by solving the implicit Eq. (2.57).

2.3 Numerical results and comparison

In this section the results that were obtained by taking advantage of the analytical solutions reported in Eqs. (2.55) and (2.57) are compared with those resulting from the numerical integration of the 3D equations of motion. In order to study the free vibration response of the damper two-bar system the initial in-plane angular rate was set to 0.02 °/s. The value of the initial angular velocity has been chosen taking into account that to get realistic oscillation amplitudes the in-plane angle (and also the out-of-plane in the 3D case) should not exceed the 90°. Please note that for oscillations going beyond this threshold the system would not go necessarily unstable. The 90° value, in fact, is just a physical constraint of the tether system: ideally, when the attitude angles reach this value it would mean that the tether is touching the mother spacecraft, thus introducing a perturbation on the system dynamic which effects go beyond the purposes of this study. Furthermore it is useful to remind that the primary scope of all the work presented here is to research and develop innovative concepts and technology devoted to stabilize an electrodynamic tether around the local vertical, thus well far from the 90° limit.

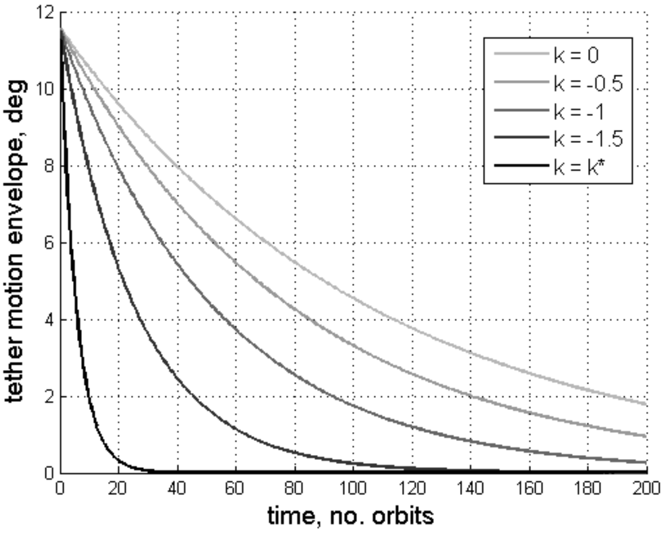

Figure 2.9: Tether oscillation decay envelopes for different values of the elastic coefficient (for $b = b^*$).

2.3.1 Oscillation envelopes

In this subsection we compare the time envelopes of damper and tether oscillation. The time envelopes have been built joining the peaks of the periodic oscillations, providing a simple and clear way to depict how fast the libration decay with time. Figure 2.10 depicts the envelopes of the oscillations of both the damper and the tether for different values of the elastic coefficient. It is worth pointing out that all curves were constructed assuming $b = b^*$ (dimensional in this section), with values given by Eq. (2.57). The dashed and solid lines are associated with the analytical solution and the 3D equations integration, respectively, whereas darker colors characterize more negative elastic coefficients. The oscillations decay from an initial value to zero in different time spans depending on the value of the elastic coefficient. The initial tether oscillation amplitude is always around 12° whereas the damper, as it could be expected, experiences increasing initial amplitudes for decreasing values of the elastic coefficient. In fact the negative spring acts on the first bar enhancing its oscillation proportionally to the absolute value of the elastic coefficient. Through the inspection of Fig. 2.10 it is possible to compare the analytical and 3D results. First of all, the trends of the two models are very similar (in some cases they are superimposed). The major differences can be spotted in the damper plot (Fig. 2.10-left) for the most negative elastic coefficients. This can be ascribed to the nonlinear contribution in the 3D equations that can become significant for high values of the oscillation (the small angles hypothesis is no longer valid). Another important difference is that the value of k_{cr} for the 3D nonlinear case is lower than for the linearized case (-1.46 against -1.975). This mean that 3D damper system goes unstable for less negative values of the elastic coefficients and thus the benefits coming from the use of a negative spring are

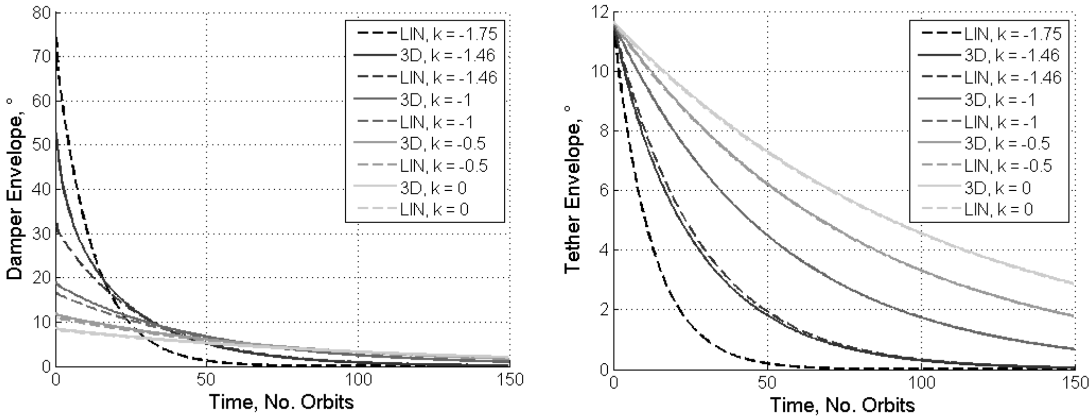

Figure 2.10: Damper (left) and tether (right) oscillation decay envelopes vs. time for different values of the elastic coefficient (for $b = b^*$).

more restrained than for the linearized system. However, this is true only at a first glance. In fact, while it is true that the linearized system is asymptotically stable for any $k > k_{cr}$, it is also possible to note that for $k = -1.75$ the damper initial in-plane angle is about 80°, that is very close to the limit condition of $\vartheta_1 = 90°$. This in turns means that values lower than $k \approx -1.75$ are not practical. Aside from the differences between the two mathematical models, the results reported in Figure 2.10 let us make two important conclusion:

1. By adopting a value of $b = b^*$ the tether oscillations are dissipated efficiently by the damper, thus providing stability to the system.

2. For decreasing (more negative) values of the elastic coefficient the tether oscillations damp out more quickly. The fastest damping occurs for values of k slightly higher than k_{cr} (note that for $k = k_{cr}$ the damper system is unstable).

2.3.2 An energy approach

In this subsection the analytical and numerical results are compared under an energetic point of view. In fact, assuming that the damper is effective in adsorbing the tether kinetic energy and that there exists an optimal configuration of the damper parameters it is reasonable to state that:

1. the optimal (b^*, k) pair is the one that minimize the tether kinetic energy;

2. the optimal (b^*, k) pair is the one that maximize the dissipated energy.

The optimal damper configuration should be the one for which the tether kinetic energy is minimized and the dissipated energy is maximized at the same time. To carry on such a study we introduced two new parameters, that is the *Mean*

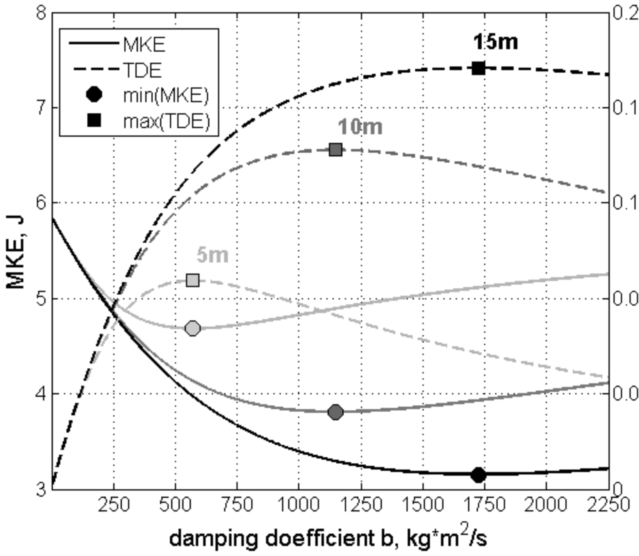

Figure 2.11: Typical energy trends as functions of the damping coefficient for different values of L_1: 5, 10, and 15 m. Curves were obtained setting $k = 0$ and $n_{sim} = 50$.

Kinetic Energy (MKE):

$$MKE = \frac{\int_0^{T_{sim}} E_k d\tau}{T_{sim}} \tag{2.58}$$

and the *Total Dissipated Energy* (TDE):

$$TDE = \frac{\int_0^{T_{sim}} E_d d\tau}{n_{sim}} \tag{2.59}$$

Equation (2.58) defines the MKE that is the kinetic energy of the second bar (i.e. the tether) averaged over a given number of orbits n_{sim} that corresponds to a simulation non-dimensional time equal to $T_{sim} = 2\pi n_{sim}$. Equation (2.59) defines the TDE that is the amount of energy dissipated by the damping device per orbit. Theoretically, as stated above, the minimum value of relaxation time should corresponds to a minimum of the MKE and a maximum of the TDE. In fact, a faster decay time means that in the time span considered the oscillations of the tether are smaller and, consequently, that the damper is working in the most efficient way.

2.3.2.1 Linearized model typical energy trends

Figure 2.11 depicts the typical trends of MKE and TDE in function of the damping coefficient obtained by means the analytical solution of the in-plane linearized model. It can be noted from Fig. 2.11 that the MKE and TDE graphs exhibit global minima and maxima, respectively, in correspondence of the same value of

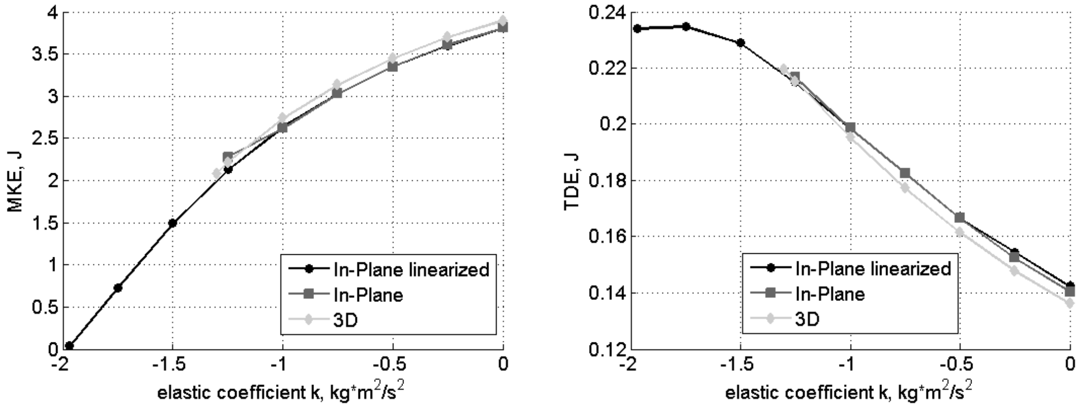

Figure 2.12: *MKE* (left) and *TDE* (right) levels as a functions of the damper's elastic coefficient (for $b = b_k^*$ and $b = b_d^*$, respectively).

the damping coefficient (1146 $kg \cdot m^2/s$ for the system under study, $L_1 = 10m$, assuming $k = 0$) as it was expected. This value of the damping coefficient coincide exactly with the optimal one found by means Eq. (2.57), meanings that the statements 1 and 2 of Par. 2.3.2 are true for the linearized case. Also, longer dampers (i.e, increasing L_1) implies higher energy dissipation efficiency along with lower kinetic energy levels, while the optimal damping coefficient moves toward higher values. On the contrary, variations of the damper mass coefficient δ_1 does not lead to appreciable changes neither in energy levels nor in the value of the damping optimal coefficient.

2.3.2.2 Non-linear models energy trends

What about the non-linear cases? To investigate if statements 1 and 2 of Par. 2.3.2 hold true also in the in-plane and 3D non-linear models we carried out several simulations adopting different values of k, each one providing the curves for *MKE* and *TDE* as in Fig. 2.11. For all simulations we recorded four parameters:

1. the damping coefficient in correspondence of the *MKE* global minimum (b_k^*);
2. the minimum value of *MKE*;
3. the damping coefficient in correspondence of the *TDE* global maximum (b_d^*);
4. the maximum value of *TDE*.

Combining these parameters in different ways it was possible to draw Figures 2.12 and 2.13. Figure 2.12 shows the trends of the minimum values of *MKE* (left) and the maximum values of *TDE* (right) for different values of the elastic coefficient. It is possible to observe that negative values of the elastic coefficient lead to lower

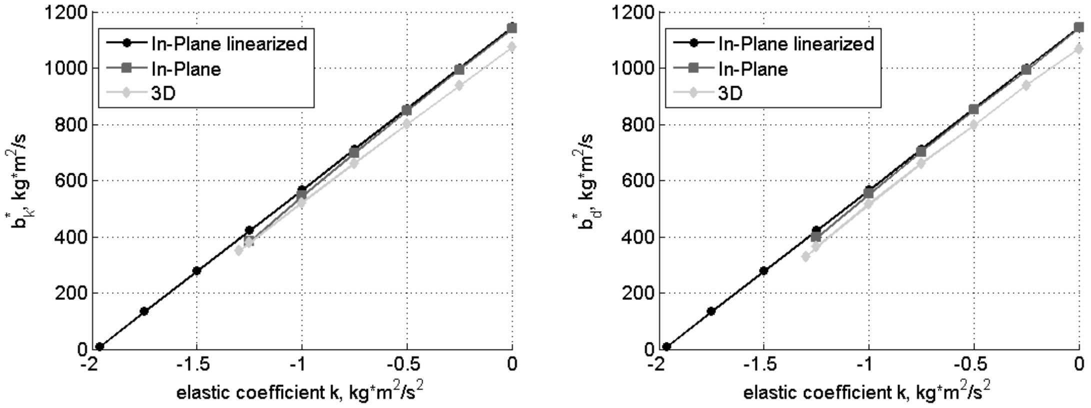

Figure 2.13: Optimal damping coefficients b_k^* (left) b_d^* (right) vs. elastic coefficient.

levels of kinetic energy (down to 45-50%) and higher levels of dissipated energy (up to 60%). Therefore, we can infer that adopting negative values of k improves simultaneously the kinetic energy transfer from the tether to the damper and its dissipation due to viscous damping. Note that for the 3D case initial angular velocities were set to $\dot{\vartheta}_{20} = \dot{\varphi}_{20} = \sqrt{2} \cdot 0.01\, deg/s$ to let the initial kinetic energy be the same as in the in-plane cases. At last, Figure 2.13 shows the pairs of values (b^*, k) considering the b_k^* and b_d^* values respectively [items (1) and (3) in the previous list]. The in-plane linearized curves in Figures 2.12 and 2.13 are obtained by solving the implicit Eq. (2.57). All results reported in this paragraph clearly show how the information on the damped two-bar system derived from the linearized model through analytical computation are consistent with those obtained from the non-linear models obtained through numerical simulations. The 3D case exhibits some differences with respect to the 2D models. For example, the optimal values of damping coefficients b_k^* and b_d^* are, with the elastic coefficient being equal, always slightly smaller (about 5%) than for the 2D cases. Also note that for all non-linear models the value of the critical elastic coefficient k_{cr} has shown to be higher (less negative) than in the linearized model: -1.25 and -1.3 $kg \cdot m^2/s^2$ for the in-plane and 3D cases, respectively. However, the trends of all results are very similar. Consequently we can conclude that the linearized model provides reliable information on the dynamic response of the damped two-bar model and indeed this model was instrumental in optimizing the pair (b, k) that provides an efficient energy dissipation.

2.4 Preliminary results from lump masses model simulations

Within the *BETs Project* a Simulator was developed at University of Padova to simulate the deorbiting of a generic spacecraft from a generic Low Earth orbit

Table 2.3: Configuration of EDT tether system for the preliminary Simulator survey.

Parameter	Value
Conductive tether length	3000m
Inert tether length	3000m
Conductive tether mass	8.1kg
Inert tether mass	3.15kg
Tether width	2cm
Tether thickness	50µm
Spacecraft mass	1000kg
Tip mass	20kg

by means of a bare electrodynamic tether. It utilizes a lump masses model and takes into account in-orbit realistic environment conditions, such as Earth magnetic field, Earth gravitational field, thermal fluxes, plasma characteristics etc. [6, 7]. In this section we report the first results obtained integrating the damper equations in the Simulator code. The pictures that will follow will be presented two by two: the plots on the left refer to the case without damper, whereas the graphs on the right are relative to the simulations carried out taking into account the damper. The elastic and damping coefficients have been set to optimal values taking advantage of the analytical study reported in the previous sections. Table 2.3 summarizes the main system variables that were used as input in the simulations.

2.4.1 Selection of damper coefficients

The analysis conducted by means the linearization of the equations of motion reported in Par. 2.2.3 gives us a powerful tool to determine the optimal damper configuration. Through Eq. (2.57), in fact, we can easily find the optimal damping coefficient b in function of the physical system parameters and of the elastic coefficient k. From previous work we are aware of some tether configurations that are suitable to deorbit heavy-class spacecraft (in the order of 1000 kg) [6, 7]. The values in Table 2.3 describe one of this standard configuration that has proven to be effective in deorbiting a 1000kg-class spacecraft from LEO orbits at every inclination. Thus, replotting Fig. 2.6 using the new mass and geometry values listed in Table 2.3 we get the updated Fig. 2.14. As it was said in Par. 2.3.1, the three-dimensional model (both in-plane and out-of-plane motion) experiences a lower value of the critical elastic coefficient k_{cr} (about 15% less). The red dashed line has been plotted taking advantage of data extrapolation from numerical sim-

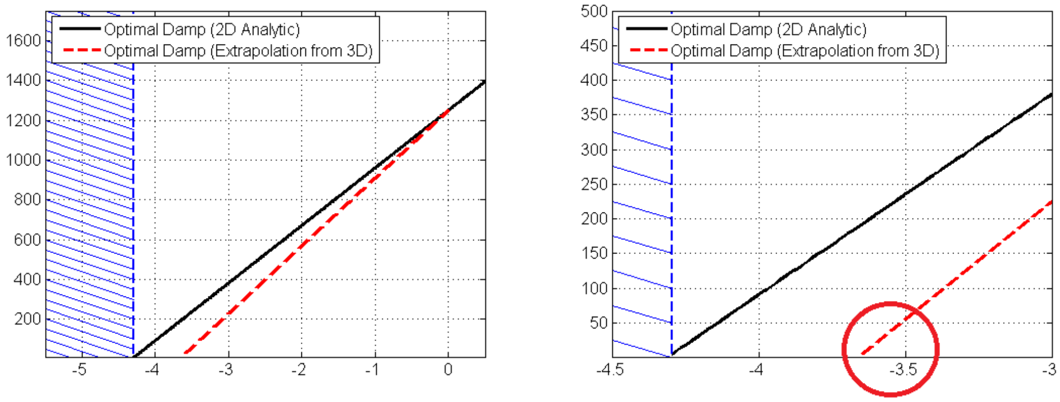

Figure 2.14: optimal damping coefficient vs. elastic coefficient for the tether configuration displayed in Table 2.3. The black solid line comes from the analytical solution (Eq. (2.57)), whereas the dashed red line was plotted making use of extrapolation data obtained from 3D model numerical simulations. The values of the elastic and damping coefficients used in the preliminary Simulator study was chosen between those contained in the red circle.

ulations of the 3D model and represents the actual $k - b^*$ curve of the damped two-bar model. Figure 2.14 (right) reports the detail of the extrapolated $k - b^*$ curve in the neighbourhood of the 3D critical elastic coefficient. After a numerical optimization process we have found that the best damper configuration, for the case under study described by Table 2.3, is as follows:

$$\begin{aligned} k &= -3.6\, kg \cdot m^2/s^2 \\ b &= 50\, kg \cdot m^2/s \end{aligned} \tag{2.60}$$

In Par. 2.3.1 it was explained how a negative elastic coefficient could lead to have, during the deorbit, damper attitude angles bigger than the 90° limit imposed by the actual system configuration. It was also explained that the passing of this practical limit does not necessarily mean that the system is undergoing a dynamical instability. After some preliminary simulations, however, we decided to adopt an angular stop for the damper in order to limit its oscillation to a precise value to avoid any problem linked to the above mentioned practical limit. Due to numerical issues that goes beyond the scope of this work we opted for a "soft stop", that is the elastic coefficient goes from negative to high positive values in a finite range. In the simulations which results are reported below this range was set to 18-23°, with the elastic coefficient going from -3.6 to 50 $kg \cdot m^2/s^2$.

2.4.2 Simulations results

In this paragraph the results obtained by means the Simulator are displayed. The pictures are shown two by two: pictures on the left refer to the no-damper case, whereas pictures on the right are related to the damped case.

2.4.2.1 Deorbit profiles

The main advantage that comes with adopting a rotational damper is clear in this first comparison: without damper the deorbit ends with a dynamical instability at about 650 km of altitude, whereas the simulation with damper completes successfully the deorbit maneuver (final altitude less than 200 km). By close inspection of Fig. 2.15 it can also be seen that the damped case has a slightly higher decay rate.

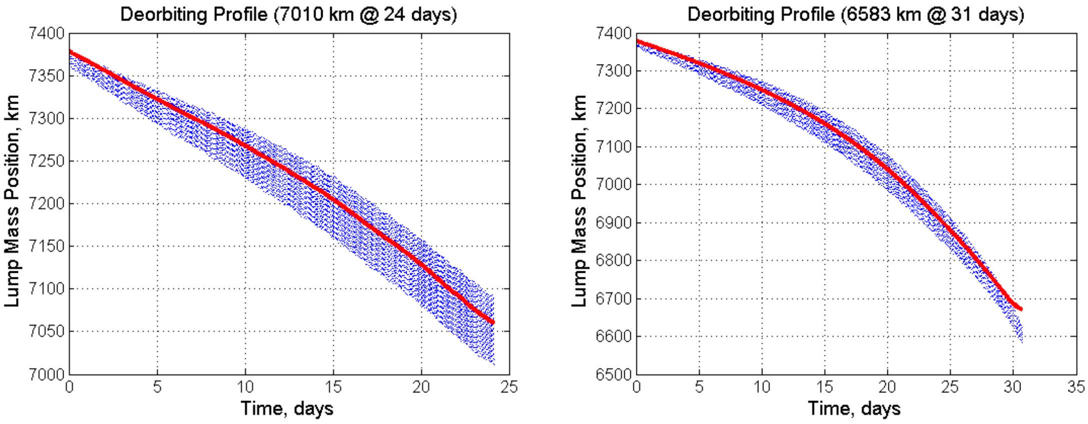

Figure 2.15: Deorbit time profiles. The solid red line is the theoretical decay profile calculated taking into account the EDT forces. (Left: no damper case, right: damped case)

2.4.2.2 Damper and tether attitude

Figures 2.16 and 2.17 depict the in-plane and out-of-plane attitude angles of both the rigid rod (plots on the right) and the spacecraft-tip mass segment. It can be seen that the librational oscillations are slightly lower in the damped case, overall in the out-of-plane. The “soft stop” behavior adopted for the damper is well visible in Fig. 2.16-right.

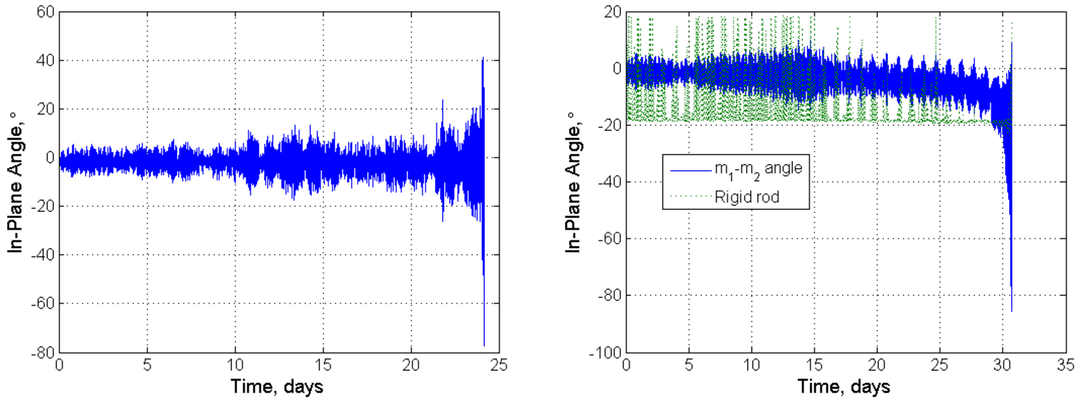

Figure 2.16: In-plane attitude angles time profiles. (Left: no damper case, right: damped case)

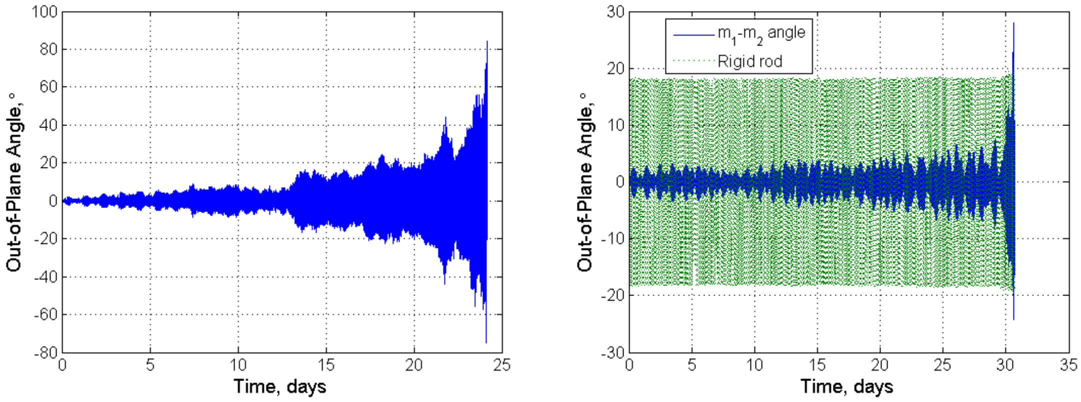

Figure 2.17: Out-of-plane attitude angles time profiles. (Left: no damper case, right: damped case)

2.4.2.3 Lump masses displacements

Figure 2.18 depicts the linear distance calculated from the spacecraft to the tip mass. This gives a good measure on how much the system is experiencing longitudinal oscillations due to the tension peaks generated by the electrodynamic forces. Longitudinal oscillations are coupled with lateral libration and vibrations and in the long run they can induce dynamical instability (as it probably happened in the no-damper case). Figures 2.19 and 2.20 depict the deflections from the local vertical of each lump masses throughout the deorbit maneuver. As it was already told in the previous paragraph, the damper produces a “smoothing” action of both in-plane and out-of-plane motions, the dynamics in fact appear to be much more regular with respect to the no-damper case.

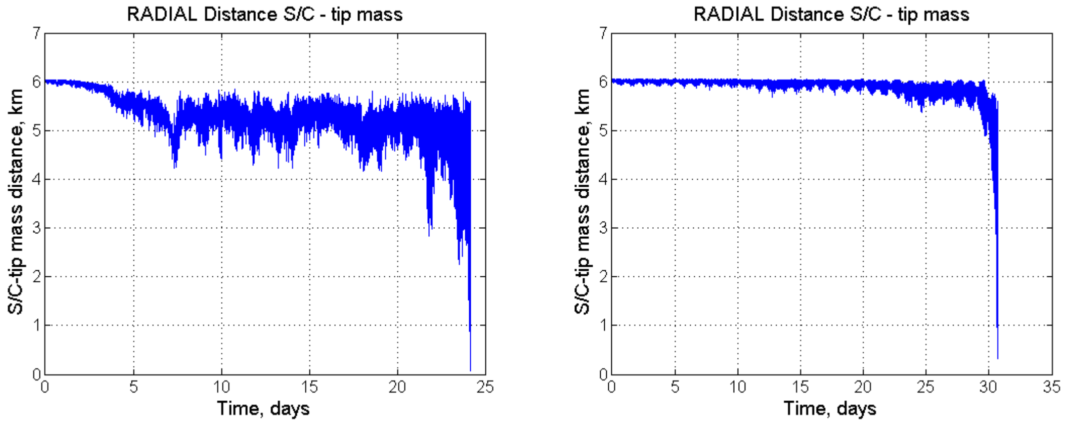

Figure 2.18: Distance between spacecraft and the tip mass. (Left: no damper case, right: damped case)

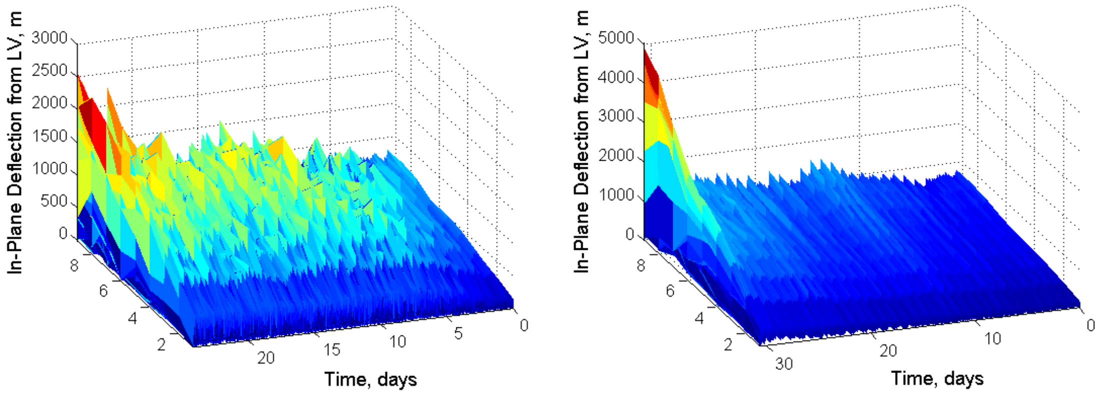

Figure 2.19: displacements of lump masses from the local vertical (x-axis) measured in the in-plane. The, x coordinate is time, y coordinate is the number of the lump masses (8 lump masses + 1 tip mass) and the z coordinate is the displacement. (Left: no damper case, right: damped case)

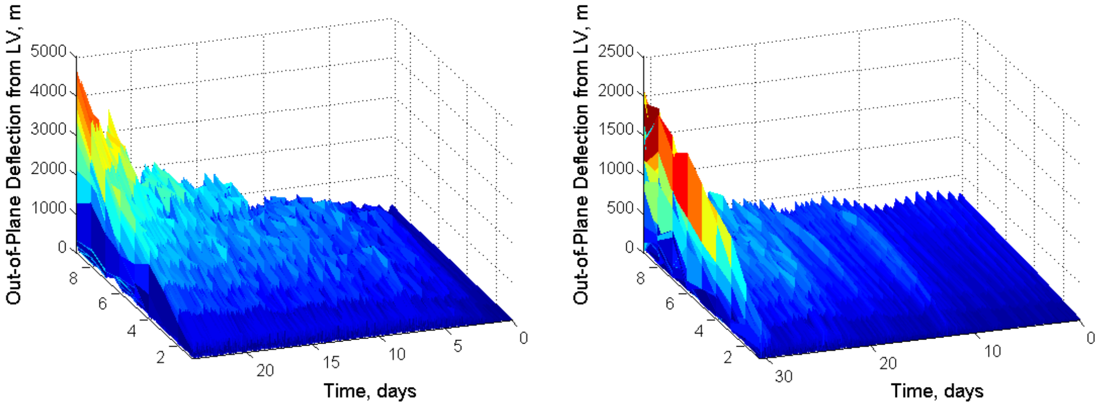

Figure 2.20: displacements of lump masses from the local vertical (x-axis) measured in the out-of-plane. The, x coordinate is time, y coordinate is the number of the lump masses (8 lump masses + 1 tip mass) and the z coordinate is the displacement. (Left: no damper case, damper: damped case)

2.4.2.4 Frequencies spectrum

The Fast Furier Transform (FFT) of both in-plane and out-of-plane motions are reported in Figures 2.21 and 2.22 for two different positions along the tether, that is in correspondence of the half of the tether and of the tip mass (the end of the tether). While performing the numerical simulations, data was saved on hard disk with a sample time of 200 s for limited memory resources reasons. Data sampling, in turn, limits the analyzed frequency spectrum to about 15 times the orbital frequency. This fact does not allow us to individuate the first longitudinal mode of vibration of the tether, which is in the order of some hundreds times the orbital frequency. In any case, sampled data allow us to study the frequencies of tether lateral motions which are responsible of dynamic mechanism that lead the system to dynamical instability, such as librational motion and the skip-rope motion. Figure 2.21 shows the FFT of lateral motions in correspondence of the half of the tether. The stabilizing action of the damper is quite clear: the damping system "clean" the spectrum removing most of the frequencies leaving only some orbital frequency multiples, such as the orbital frequency itself (ω), the first out-of-plane mode of vibration (2ω), the first in-plane mode of vibration (between ω and 2ω) and the frequencies associated with lateral vibrations (about 7ω). The same could be said about Fig. 2.22.

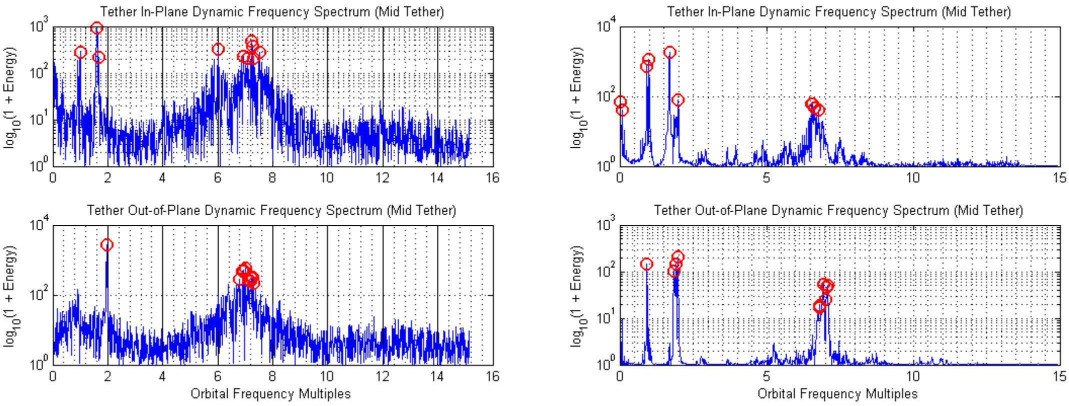

Figure 2.21: frequency spectrum analysis of in-plane and out-of-plane motions in correspondence of mid-tether. (Left: no damper case, right: damped case)

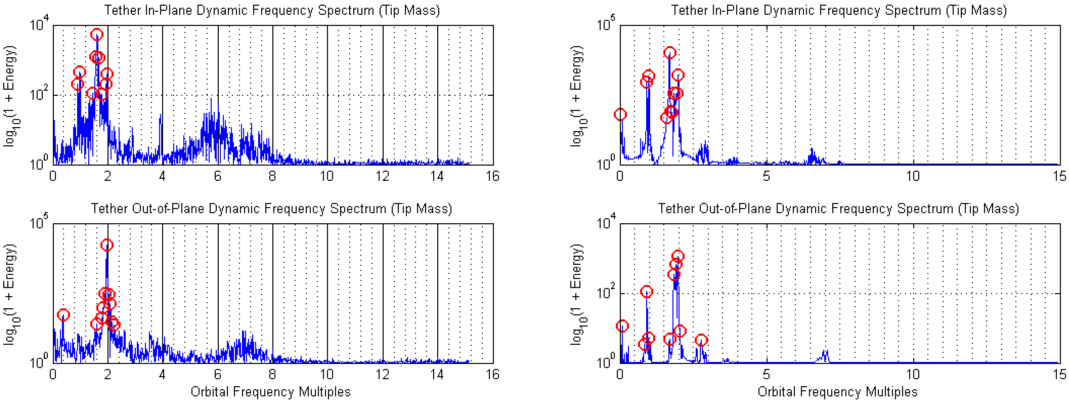

Figure 2.22: frequency spectrum analysis of in-plane and out-of-plane motions in correspondence of the end of the tether (tip mass). (Left: no damper case, right: damped case)

2.5 Conclusions

The free-vibration response of a system consisting of a long tether and a damper has been investigated by means of different mathematical models with the goal of finding an optimal configuration of the damper device aimed at minimizing the tether oscillations. The damped model is a natural evolution of the undamped two-bar model used by several authors to study the lateral dynamics of an electrodynamic tether driven by Lorentz forces. The analytical solution of the linearized equations of motion in the orbit plane has highlighted the existence of an optimal combination of damping and elastic coefficients that minimize the tether kinetic energy and simultaneously maximize its dissipation through the viscous damper. Thus, we can state that an optimization equation like $\hat{f}$ does exists and it is in an implicit form. Moreover, results obtained through numerical simulations have shown a good match between the analytical model and the non-linear models (both in 2D and 3D). The transfer of energy from the tether to the damper device has proven to be effective when the appropriate values of the elastic and damping coefficients are adopted.

Bibliography

[1] Peláez, J., Ruiz, M., López-Rebollal, O., Lorenzini, E. C., *Two-Bar Model for the Dynamics and Stability of Electrodynamic Tethers*, Journal of Guidance, Control and Dynamics, Vol. 25, No. 6, 2002, pp. 1125-1135.Peláez, J., Lorenzini, E. C., López-Rebollal, O., and Ruiz, M., *A New Kind of Dynamic Instability in Electrodynamic Tethers*, Journal of the Astronautical Sciences, Vol. 48, No. 4, 2000, pp. 449-476.

[2] Peláez, J., Lorenzini, E. C., López-Rebollal, O., and Ruiz, M., *A New Kind of Dynamic Instability in Electrodynamic Tethers*, Journal of the Astronautical Sciences, Vol. 48, No. 4, 2000, pp. 449-476.

[3] Landau, L., and Lifshitz, E., *Mecanique*, Vol. 1, Cours de Physique Theorique, Mir, Moscow, 1982, p. 192.

[4] Mantellato, R., Pertile, M., Colombatti, G., and Lorenzini, E.C., *Analysis of Passive System to Damp the Libration of Electrodynamic Tethers for Deorbiting*, AIAA Space 2013 Conference & Exposition, 10-12 September 2013, San Diego, CA, 10.2514/6.20132-5390.

[5] Mantellato, R., Pertile, M., Colombatti, G., Valmorbida, A., and Lorenzini, E.C., *Two-bar Model for Free Vibrations Damping of Space Tethers by Means of Spring-Dashpot Devices*, CEAS Space Journal, Vol. 6, No. 3, 2014, pp. 133-143. doi: 10.1007/s12567-014-0065-x

[6] Zanutto, D., Colombatti, G., and Lorenzini, E. C., *Electrodynamic Tethers For Deorbiting Maneuvers*, 3rd CEAS Air&Space Conference, Venice, Italy, 2011.

[7] Zanutto, D., Lorenzini, E. C., Mantellato, R., Colombatti, G., and Sanchez-Torres, A., *Orbital Debris Mitigation Through Deorbiting with Passive Electrodynamic Drag*, 63rd International Astronautical Congress, IAF, Naples, Italy, 2012.

3 Tether Deployment Strategies

The study of the dynamics of a tether during deployment operations within BETs Project was firstly started by my predecessor (Zanutto D., see [1]). In his work all mayor issues concerning the deployment of a tether from an orbiting spacecraft were introduced and analyzed. A librating deployment has been preferred to a spinning one and a passive reeling deployer equipped with a brake system was designed and prototyped at DLR-Bremen in their Work Package. Deployment is carried out with the help of a low-thrust propulsion system mounted on the tip mass which is necessary to unwind the tether out of the deployer keeping it constantly taut. Two kinds of software were developed to find out the best way to deploy a multi-kilometer tether in space. The first one was used to study and derive tether reference trajectories during deployment through a numerical optimization (REference TRajectories Optimization tool, RETRO) Reference trajectories provide tether length and speed time profiles to be implemented in the second software (Deployment Dynamic Simulator, DDS), that simulates the deployment maneuver taking into consideration as much as possible the actual mechanical system (e.g., reel, brake system, friction) as well as possible attitude errors at the beginning of the deployment maneuver and external perturbations acting on the deploying tether. With respect to previous work, RETRO was optimized and improved allowing for faster and more effective numerical trajectories optimization. Thanks to this, a new family of reference trajectories were found that allow for complete deployment of 6-km and 10-km tether in less than 1.5 hours with residual librations very close to zero. In the DDS software the inertia equation of the reel has been added along with an Archimedean spiral model to simulate the tether unwinding from the reel. A Proportional-Derivative feedback brake system control has been implemented. An extensive error sensitivity analysis was carried out to monitor the effectiveness of the control system when the tether system is subjected to errors/perturbations. The results show that the PD control that utilize the new reference trajectories is very robust when the deployment starts with an in-plane angle equal to 40° (measured from the local vertical toward the orbital velocity vector direction). Simulations have also underlined that the forces due to the gravity gradient can be sufficient to complete the deployment with the propulsive system turned off after a well-determined time from the deployment start. This in turn means that the thruster is used for a shorter time span during deployment thus reducing the propellant mass required for a complete deployment maneuver.

3.1 BETs Project system configuration summary

In this section I summarize the main characteristics of BETs system that are crucial for the study of tether deployment. Please note that the subsystems configuration that are described hereafter refer to the last available Deliverables handed in by the BETs consortium (February 2014, [2, 3])

3.1.1 Dumbbell model

Like in previous deployment survey, I modeled the tether as a rigid rod (dumbbell model) with time-varying length. It is worth to remind that this assumption is valid because the tether, during deployment process, is kept taut by the tension due to the brake friction on one side and by the thrust force acting on the tip mass together with gravity gradient on the opposite side. Furthermore, simulations show that deployment is always carried out in less than one orbit period thus not allowing enough time for lateral oscillations to be excited.

3.1.2 Librating deployment

A tether librating deployment from a non-spinning spacecraft has been preferred to a spinning deployment because it can be used in a wider range of spacecraft classes. Most likely, the deployer will be attached at one of the outer side of the spacecraft. In this study I assume that deployment operations start from a spacecraft in which the attitude is (at least in the early stage of deployment) 3-axis stabilized by the satellite attitude control system. The initial tether attitude, in fact, significantly influences the tether dynamic at the end of deployment: final residual librations proved to be quite sensible to initial spacecraft attitude conditions with a minimum encountered at a specific tether angle (see later on).

3.1.3 Low-thrust propulsion subsystem

A low-thrust propulsion system will act on the tip mass along the tether longitudinal axis (see Fig. 3.1). Thus, the tether will be unwinded taking advantage of both gravity gradient (that is very weak at the beginning of the maneuver) and thruster action. The propulsion system should be selected taking into account the long hibernation period before it is activated. Most likely, the propulsion system will consist of a tank containing pressurized gas connected to a certain number of nozzles arranged in a proper geometry to guarantee a directional thrust stability around the tether longitudinal axis.

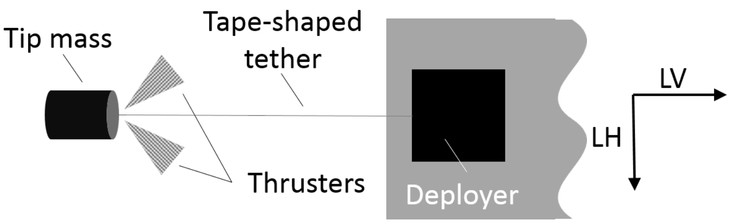

Figure 3.1: sketch of a possible deployment system configuration.

3.1.4 Passive deployer

The deployer has been designed and prototyped by DLR-Bremen (Fig. 3.2). It is a passive non-motorized reeling mechanism equipped with a brake system. The configuration is the result of a trade-off between mass, reliability and simplicity requirements.

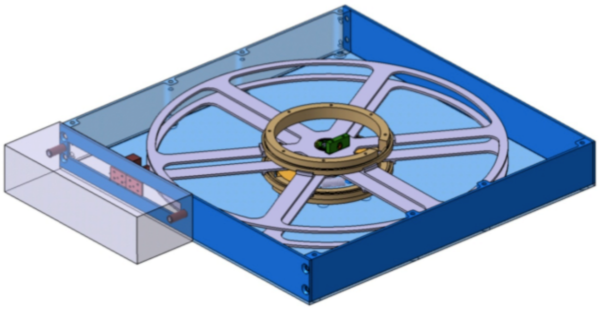

Figure 3.2: section of the deployer prototype. In evidence the reel inside the box around which the tape tether is to be rolled up.

3.1.5 Brake control system

The deployer is equipped with a brake mechanism which is used to indirectly (i.e., through friction) control the tether exit velocity (Fig. 3.3). The brake control system is necessary to ensure a proper end-of-deployment tether residual libration, that we want to be as small as possible. The brake action will be commanded by the PD Control Law.

3.1.6 PD control law

The feedback control loop that controls the brake action is a linear Proportional-Derivative law based on errors with respect to the length and length rate time profiles provided by the reference trajectory. The proportional term is dependent on the difference between actual and reference length time profile, while the derivative term is proportional to the difference between actual and reference exit speed time profile. During in-orbit operations, instantaneous tether length and

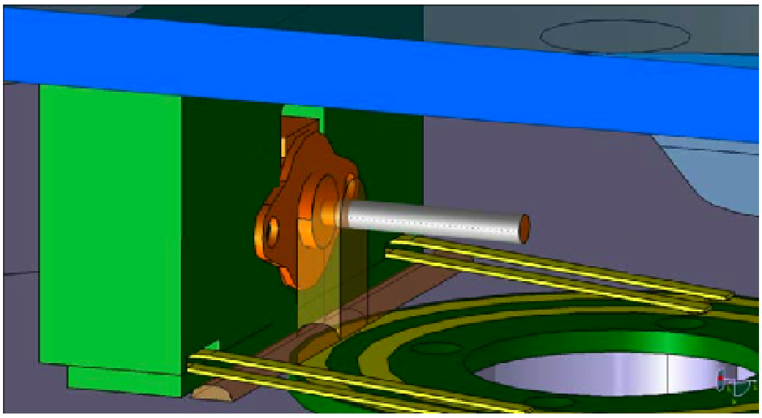

Figure 3.3: a detail of the brake system.

speed must be measured and provided to the brake control subsystem by a proper set of sensors (e.g., incremental encoder coupled with the reel shaft).

3.2 Reference trajectories

3.2.1 Why do we need reference trajectories?

The answer to this question is simple: we need to find good reference trajectories because they provide the information (i.e., length and speed time profiles vs time) that the tether must follow to reach the desired final dynamic state (e.g., small libration angle and low longitudinal velocity) starting from given initial conditions. Although the dumbbell model equations are relatively compact, they are strongly non-linear. A linearized analysis can provide useful information only under the assumptions of small librations and a constant tether length, hence it is not applicable to deployment. For this reason, I carried out by means of our software RETRO a numerical optimization of the deployment maneuver and solved a boundary problem for a non-linear dynamic system to find the best trajectory that the tether must follow to be deployed in space. The reference trajectory is then used by the brake feedback control; when the control works properly it guarantees a correct deployment of the tether, ideally following exactly the reference trajectory.

3.2.2 Reference trajectory numerical optimization

Reference trajectories were found by means of a numerical optimization process (see Fig. 3.4 for the conceptual scheme). Referring to [1, 2, 4], below I briefly explain how this process works.

1. The optimization software takes as input the first iteration (attempt) of the brake friction profile defined by a certain number of pivot points, the system parameters (e.g., tether length, thickness, width), the attitude of the tether

system at the beginning of deployment and the desired tether attitude at the end of deployment (e.g., aligned with local vertical and in stationary conditions). The pivot points define the brake friction profile in function of the tether length (i.e., $T = T(l)$) in a discretized way. Subsequently the finite number of friction values are interpolated with a spline to provide a continue function to the numerical integrator.

2. The numerical optimization is carried out by means of a Multidimensional Unconstrained Non-Linear Minimization, that utilizes the Nelder-Mead Matlab routine (FminSearch). The algorithm tries to minimize a linear function (the "Cost Function") that depends on non-linear differential equations and a certain number of variables, for instance each pivot point of the brake profile is a variable. The algorithm also does not pose any other constrains to the search of the minimum (hence the term "Unconstrained"). Consequently, if any constrains are to be added (i.e., brake force always positive) they must be written manually in the code.

3. Nelder-Mead algorithm simply tries to minimize a determined cost function which depends on the tether dynamics during deployment maneuver:

$$\begin{aligned} F &= C_1 \left(l_{end} - l_{goal}\right)^2 + C_2 \left(\dot{l}_{end} - \dot{l}_{goal}\right)^2 + \\ &\quad + C_3 \left(\vartheta_{end} - \vartheta_{goal}\right)^2 + C_4 \left(\dot{\vartheta}_{end} - \dot{\vartheta}_{goal}\right)^2 \end{aligned} \tag{3.1}$$

   The cost function was designed to be dependent on the square of the difference between the actual and the goal values of tether length, speed, in-plane angle and in-plane angular velocity at the end of deployment. Each component is multiplied by a constant weight factor. Varying the four weights the importance of each component in the numerical minimization is changed. In particular, the components associated with the tether in-plane angle and in-plane angular velocity have shown to be crucial for obtaining good reference trajectories. The C_3 and C_4 weights must be greater than C_1 and C_2 by some orders of magnitude to take into account the different scales among the variables. The algorithm modifies at each iteration the previous brake friction profiles changing the value of only one pivot point at a time, integrates the dynamic equations to obtain the new iteration values of end-of-deployment length, length rate, in-plane angle and in-plane angular velocity and calculates the new cost function value. The out-of-plane dynamics was not included in the cost function because during deployment it does not affect significantly the end-of-maneuver tether attitude.

4. When the cost function variation falls under a predefined tolerance the software returns the optimal trajectory and it saves the length and the speed time profiles which will be used later on in the DDS.

There is a problem with using an unconstrained numerical optimization: there are thousands of local minimum of the cost function. As a consequence, the final

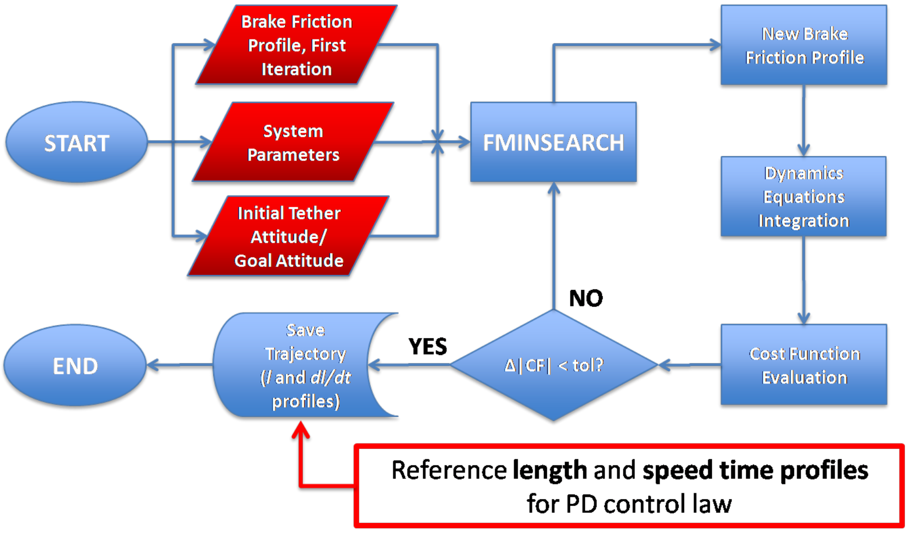

Figure 3.4: conceptual scheme of RETRO.

trajectory is highly dependent on the first brake friction iteration, on the cost function weights, which must be very carefully defined through many attempts, and on the number of pivot points.

3.2.3 Deployment dynamics equations

The equations of motion of a tether during deployment from an orbiting spacecraft can be found utilizing the Lagrangian equation of the system in a similar fashion as reported in [5]. Considering a length-varying dumbbell model the generalized coordinates vector becomes:

$$\bar{q}_d = (\vartheta, \varphi, l) \tag{3.2}$$

The Synodic reference frame used in this section is the same ad in Fig. 2.1. Following the procedure described in [5], the kinetic energy, the gravitational potential, and the potential associated with apparent forces of a point mass can be found:

$$T_d = \frac{1}{2} m_B \left[\dot{l}^2 + l^2 \left(c^2\varphi \dot{\vartheta}^2 + \dot{\varphi}^2\right)\right] \tag{3.3}$$

$$V_{g,d} = \frac{1}{2} m_B \omega^2 l \left[2ac\vartheta c\varphi + l\left(1 - 3c^2\vartheta c^2\varphi\right)\right] \tag{3.4}$$

$$V_{i,d} = -\frac{1}{2} m_B \omega^2 l \left[2ac\vartheta c\varphi + lc^2\varphi \left(1 + 2\frac{\dot{\vartheta}}{\omega}\right)\right] \tag{3.5}$$

Thus the Lagrangian equation of the point mass at the end of the tether being deployed is:

$$\mathcal{L}_{B,d} = \frac{1}{2} m_B \dot{l}^2 + \frac{1}{2} m_B l^2 \left[c^2\varphi \left(\left(\omega + \dot{\vartheta}\right)^2 + 3\omega^2 c^2\vartheta\right) + \dot{\varphi}^2\right] \tag{3.6}$$

The Lagrangian equation of a length-varying bar is calculated integrating Eq. (3.6) over the whole tether length:

$$\mathcal{L}_{bar,d} = \frac{1}{2}\rho l \dot{l}^2 + \frac{1}{6}\rho l^3 \left[c^2\varphi \left(\left(\omega + \dot{\vartheta} \right)^2 + 3\omega^2 c^2\vartheta \right) + \dot{\varphi}^2 \right] \tag{3.7}$$

Finally, the complete Lagrangian equation of the varying-length dumbbell model is the sum of Eq. (3.6) and (3.7):

$$\mathcal{L}_d = \frac{1}{2}\left(m_B + \rho l\right) \dot{l}^2 + \frac{1}{6} l^2 \left(3m_B + \rho l\right) \left[c^2\varphi \left(\left(\omega + \dot{\vartheta} \right)^2 + 3\omega^2 c^2\vartheta \right) + \dot{\varphi}^2 \right] \tag{3.8}$$

The equations of motions are eventually calculated from the Lagrangian $\mathcal{L}_d$ as described in Par. 2.1.3 (see Eq. (2.37)). The resulting three equations of motions are reported in (3.9)-(3.11):

$$\ddot{\vartheta} = -3\frac{2m_B + \rho l}{3m_B + \rho l}\left(\omega + \dot{\vartheta} \right)\frac{\dot{l}}{l} + 2\left(\omega + \dot{\vartheta} \right)\dot{\varphi}\tan\varphi - 3\omega^2 s\vartheta c\vartheta \tag{3.9}$$

$$\ddot{\varphi} = -3\frac{2m_B + \rho l}{3m_B + \rho l}\dot{\varphi}\frac{\dot{l}}{l} - s\varphi c\varphi\left[3\omega^2 c^2\vartheta + \left(\omega + \dot{\vartheta} \right)^2 \right] \tag{3.10}$$

$$\begin{aligned} \ddot{l} = & -\frac{\rho \dot{l}^2}{2\left(m_B + \rho l\right)} + l\frac{2m_B + \rho l}{2\left(m_B + \rho l\right)}\left[c^2\varphi \left(\left(\omega + \dot{\vartheta} \right)^2 + 3\omega c^2\vartheta \right) + \dot{\varphi}^2 \right] \\ & + \frac{F_{thrust} - F_{brake} - F_0}{\left(m_B + \rho l\right)} \end{aligned} \tag{3.11}$$

Equation (3.9) describes the in-plane motion, Eq. (3.10) the out-of-plane motion, and Eq. (3.11) describes the motion along the tether longitudinal axis, that is the motion of the tether being unrolled. Taking into consideration the last equation, it can be seen by inspection that the first term is proportional to $\rho\dot{l}^2$and it represents the *convective term* associated with the tether mass flowing out of the deployer. The contribution of this term is very small in this study and its role is equivalent to a small increase of the brake force. If properly rearranged, the terms inside the square brackets can be clearly associated to the different contributions:

$$\overbrace{\omega^2\left[\left(1 + 3c^2\vartheta \right) c^2\varphi - 1 \right]}^{gravity\,gradient} \overbrace{+2\omega\dot{\vartheta}c^2\varphi}^{Coriolis} \overbrace{+c^2\varphi\dot{\vartheta}^2 + \dot{\varphi}^2}^{centrifugal}$$

The gravity gradient and the centrifugal terms are always positive, whereas Coriolis term is negative/positive when in-plane angular velocity is negative/positive. The last term on the right side of Eq. (3.11) represents the contributions of the external forces, i.e. the propulsion system thrust, the brake force, and the intrinsic friction originated inside the reeling mechanisms.

3.2.4 Reference trajectories

Now let us concentrate on the reference trajectories. In this study we considered different system configurations with respect to the initial in-plane angle and the tether length. First of all, both BETs "standard" lengths of 6km and 10km were considered. Concerning the initial in-plane angle, it is the direction which the deployment device should be pointing at the beginning of the deployment maneuver, more precisely the angle ϑ in the xz plane from the local vertical. During the present study we derived reference profiles for the 0°, 20°, 40° and 60° cases. A preliminary sensitivity analysis sharply highlighted that the tether system experiences a minimum in the errors/perturbations sensibility around the initial in-plane angle value of 40°. For the sake of clarity, therefore, in this section only the results of the most representative case are going to be reported: the 0° case as a reference case and the best case at 40° (see Table 3.1). The 20° and 60° cases results are reported in Appendix of [2].

Table 3.2 lists the main system parameters which are common for all cases. The thruster and the reel friction forces have been assumed to be equal to 250mN and 100mN, respectively. Tether cross section is the standard 2cm x 50µm, the ballast mass is equal to 20kg and the initial orbital height is equal to 1000km.

Table 3.3 shows the initial tether attitude for the analyzed cases. The initial tether attitude is given as an input in the numerical optimization. All variables at the initial time (beginning of deployment) are equal to zero except for the initial in-plane angle: deployment in CASE 1 and CASE 3 start with the tether aligned along the local vertical ($\vartheta_0 = 0°$) while CASE 2 and CASE 4 start at 40° with respect to the local vertical toward the orbital motion. At the end of the deployment, we always want the tether to be aligned with the local vertical with zero velocity (i.e., with zero residual libration). Consequently, the final attitude variables are all set to zero (see Table 3.4), with the only exception for the final length, which must be 6 km or 10 km, according to the cases.

In Figs. 3.5-3.8 results for each cases listed in Table 3.1 are shown. In every figure four plots are reported:

- Figure A: Reference Trajectory. This plot shows the reference trajectory in space of the tip mass throughout the deployment maneuver. The coordinates are expressed in the Synodic frame and we report only the trajectory in the orbital plane, as the libration in the out-of-plane is small and does not pose any problem for the tether stability. The abscissa corresponds to the Synodic x axis that is parallel to the local vertical (LV). The ordinate corresponds to the Synodic z axis that is parallel to the local horizon (LH). The blue circle indicates the position of the tip mass at the end of deployment, that is when the tether length reaches the goal value (6 km or 10 km).

- Figure B: Brake Tension Profile. The brake profile shows the values in Newtons of the brake friction in correspondence to the 25 (16) pivot points (in red) which are uniformly distributed along the deployed tether length.

Table 3.1: deployment reference cases summary.

	CASE 1	CASE 2	CASE 3	CASE 4
Initial in-plane angle ϑ_0	0°	40°	0°	40°
Tether length L	6 km	6 km	10 km	10 km

Table 3.2: common tether system parameters.

F_{thrust}	F_0	Tether Width	Tether Thickness	Ballast Mass	Orbit Altitude
250 mN	100 mN	2 cm	50 µm	20 kg	1000 km

Table 3.3: tether attitude state vector at the beginning of the deployment. In-plane angle is equal to 0° for CASES 1 and 3 and 40° for CASE 2 and 4.

ϑ_0	$\dot{\vartheta}_0$	φ_0	$\dot{\varphi}_0$	l_0	$\dot{l}_0$
0°/40°	0 °/s	0°	0 °/s	0 m	0 m/s

Table 3.4: goal tether attitude state vector at the end of the deployment. Final length is equal to 6km for CASE 1 and 2 and 10km for CASES 3 and 4.

ϑ_{end}	$\dot{\vartheta}_{end}$	φ_{end}	$\dot{\varphi}_{end}$	l_{end}	$\dot{l}_{end}$
0°	0 °/s	0°	0 °/s	6/10 km	0 m/s

In the optimization algorithm the brake profile is fixed for each iteration at a discrete number of points. Since the dynamics equations integration needs to know the brake friction value in a much higher number of points, these are provided by means of cubic spline interpolation. The spline is plotted with the black solid line.

- Figure C: Tether Attitude. The upper subplot reports the in-plane libration of the tether throughout deployment, while the bottom subplot shows the tether in-plane angular velocity. A good deployment trajectory implies that both of these variables take a value close to zero at the end of deployment.
- Figure D: PD Time Profiles. Length and length rate time profiles that represent the actual output of the optimization process. They will be used by the PD Brake Control as reference profiles to be compared to the actual values computed in the DDS.

Reference Trajectory: CASE 1

Table 3.5: summary of reference CASE 1.

Initial in-plane angle ϑ_0	Tether length L	Deployment time
0°	6 km	67.02 min (64% of T_{orb})

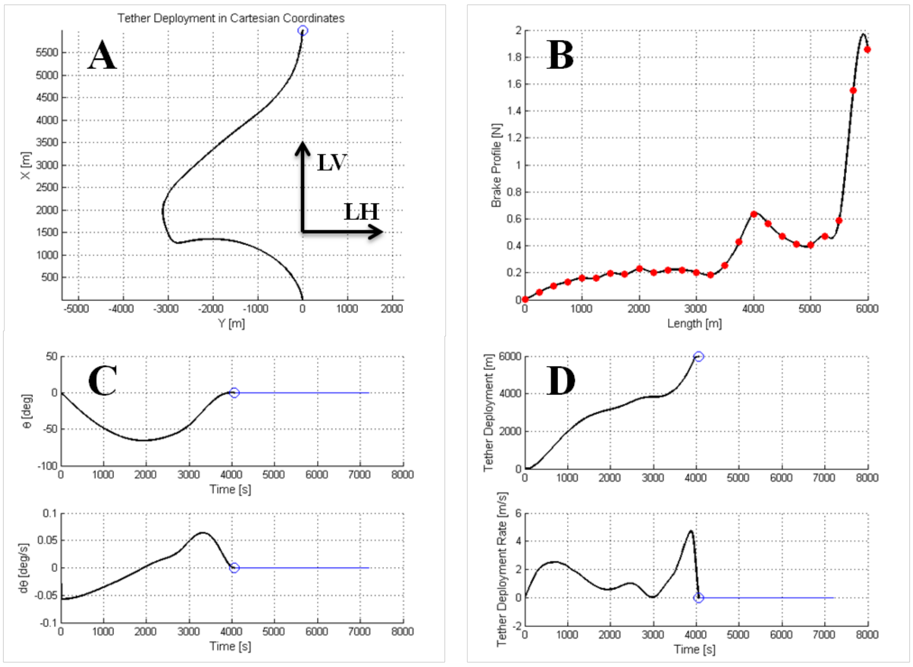

Figure 3.5: CASE 1 optimization results: A) reference trajectory; B) brake tension profile; C) tether attitude; D) PD tether length and length rate profiles.

Reference Trajectory: CASE 2

Table 3.6: summary of reference CASE 2.

Initial in-plane angle ϑ_0	Tether length L	Deployment time
40°	6 km	85.32 min (81% of T_{orb})

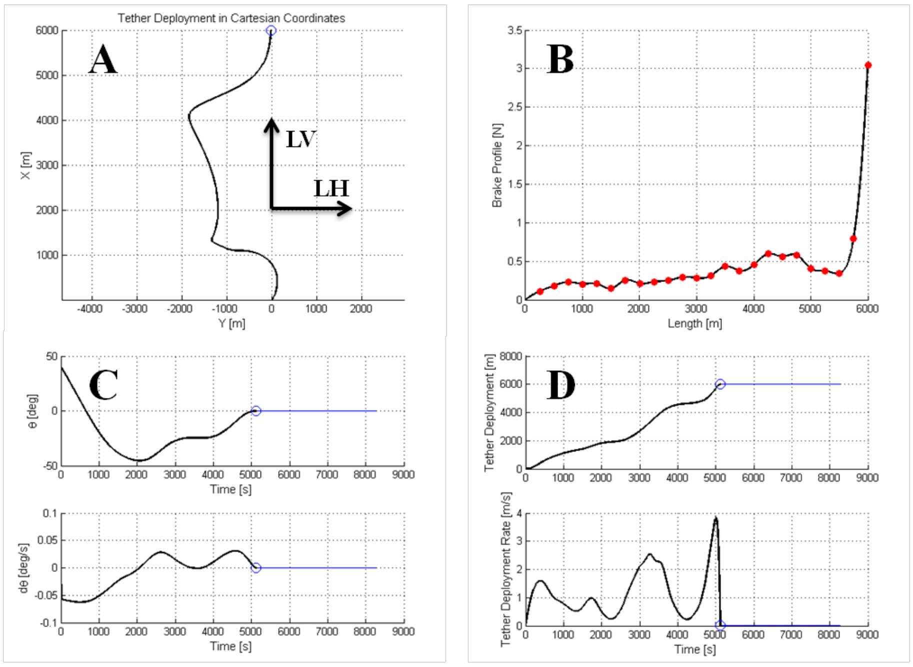

Figure 3.6: CASE 2 optimization results: A) reference trajectory; B) brake tension profile; C) tether attitude; D) PD tether length and length rate profiles.

Reference Trajectory: CASE 3

Table 3.7: summary of reference CASE 3.

Initial in-plane angle ϑ_0	Tether length L	Deployment time
0°	10 km	81.4 min (77% of T_{orb})

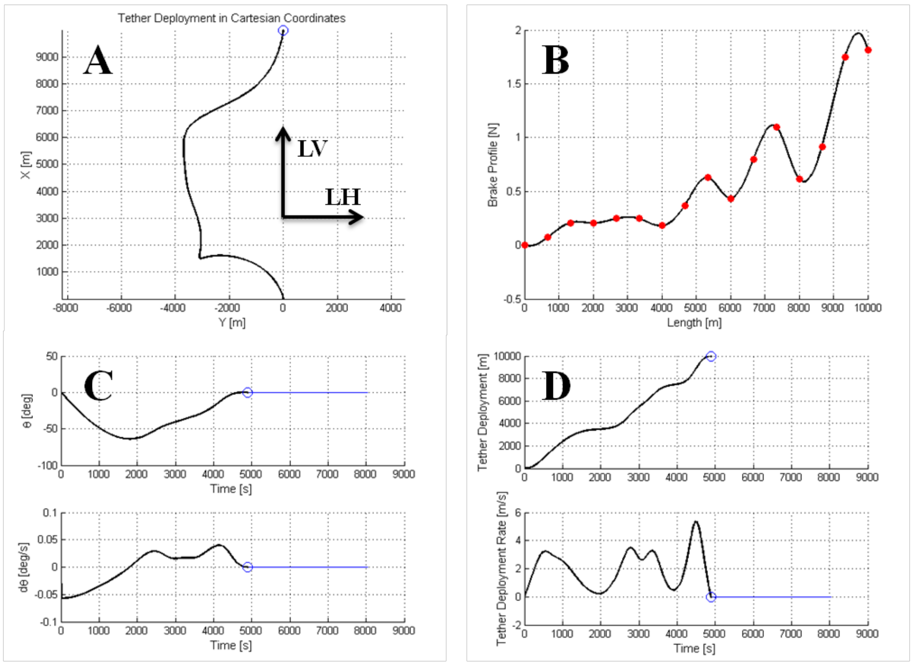

Figure 3.7: CASE 3 optimization results: A) reference trajectory; B) brake tension profile; C) tether attitude; D) PD tether length and length rate profiles.

Reference Trajectory: CASE 4

Table 3.8: summary of reference CASE 4.

Initial in-plane angle ϑ_0	Tether length L	Deployment time
40°	10 km	73.77 min (70% of T_{orb})

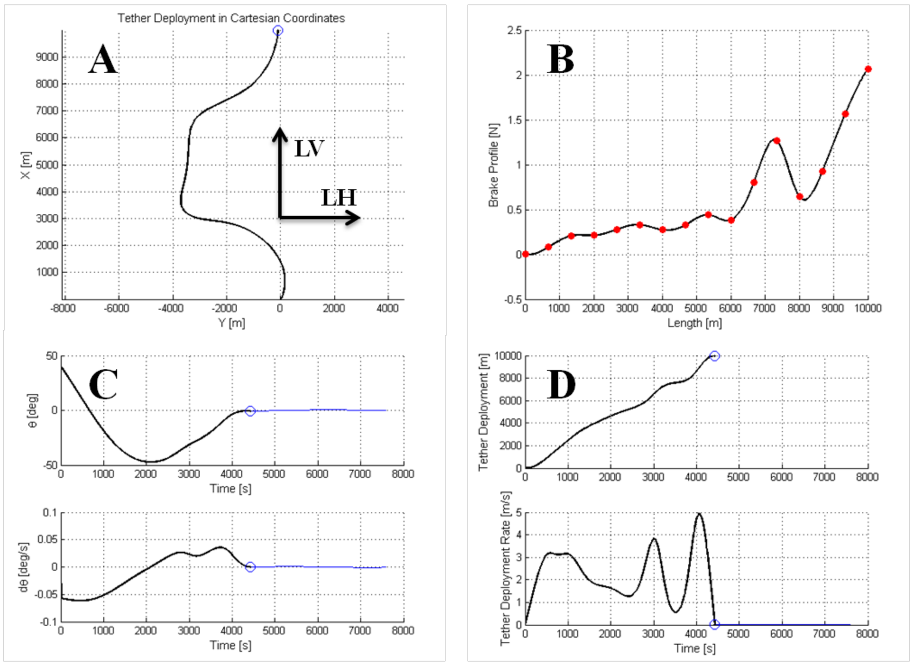

Figure 3.8: CASE 4 optimization results: A) reference trajectory; B) brake tension profile; C) tether attitude; D) PD tether length and length rate profiles.

3.2.5 Results interpretations

As it can be seen by inspection of Figs. 3.5-3.8, the end-of-deployment conditions are exactly as desired, that is in-plane angle and in-plane velocity equal to zero. This means that the tether ends its deployment perfectly aligned with the local vertical and it remains still in that position until the electrodynamic effect begins to excite lateral oscillations. In all cases the deployment time remains below one orbital period and always below 1.5 hours. This is quite good because it means that the deorbiting operations can start within a short time after the spacecraft has deployed the tether. Moreover, the low deployment time also avoids that the external perturbations excite the tether motion during the deployment. There are some important differences between the $\vartheta_0 = 0°$ and the $\vartheta_0 = 40°$ that are worth noting. The brake profiles in the former cases are much more irregular than in the latter cases. Furthermore, the minimum value of the tether longitudinal velocity considerably increases in CASES 2 and 4: this is an improvement with respect to CASES 1 and 3 because it means that the length rate of the tether is always well far away from zero. In fact, if the length rate should decrease to zero or, worse, to negative values the tether deployment would be interrupted. However, the most important difference between the $\vartheta_0 = 0°$ and the $\vartheta_0 = 40°$cases is surely the fact that in the former cases the libration amplitude can reach or even go beyond -60° in the in-plane. It is worth reminding here that the libration instability would occur when the one of the tether attitude angle reaches the limit of ± 90°, hence leading to a mission failure because the tether would start to roll around the spacecraft. In addition, the ± 90° limit is a theoretical limit: simulations have highlighted that libration instability can be predicted when the tether attitude angles reach an even lower value. Thus in the 0° cases the margin from instability conditions is much less than 30°. On the contrary, the deployment trajectories in the 40° cases experiences a more limited maximum libration amplitude, that is between -40° and 40°, considerably increasing the stability margin. In the section dedicated to the error sensitivity analysis it will be shown that ejecting the tip mass at 40° toward the orbital velocity direction can bring many additional improvements concerning libration stability during deployment.

3.3 Closed-Loop Brake Control

3.3.1 Reel inertia and Archimedean Model

The reel inertia has been included in the dynamics equations to simulate more accurately the tether unwinding process. Referring to Fig. 3.9, the reel moment of inertia is given by Eq. (2.37):

$$I_{reel} = \frac{1}{2} m_o \left(r_0^2 + r_{ext}^2\right) + \frac{1}{2} l_{rol} \rho \left(r_0^2 + r_{rol}^2\right) \tag{3.12}$$

where $l_{rol}$and r_{rol} are functions of the reel position angle ψ (see Eqs. (3.14) and

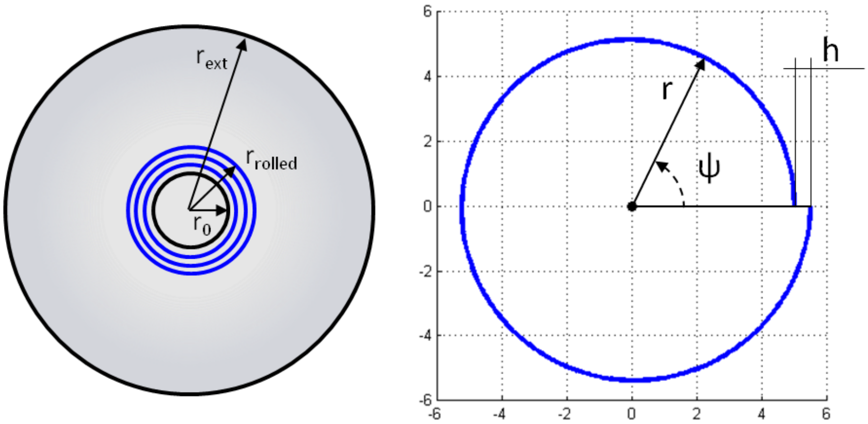

Figure 3.9: definition of reel geometric parameters (left) and Archimedean spiral model for rolled tether (right).

(3.15)), m_o is the inert reel mass and ρ is the tether linear density. Since the reel loses mass as the tether is unwinded the moment of inertia is a time-dependent function of ψ. Please note that the reel position angle is equal to zero when the tether is completely unrolled. Equation (3.13) describes the rotational motion of the reel subjected to the external torques:

$$I_{reel}\ddot{\psi} = T_{dyn} + T_{thrust} + T_0 + T_{brake} \tag{3.13}$$

where T_{dyn} is the torque due to gravitational gradient, convective, Coriolis, and centrifugal terms, T_{thrust} is the torque originated by the propulsion system acting on the tip mass, T_0 is the torque due to the reel mechanism friction, and T_{brake} is the control torque stemming from the brake action commanded by the PD feedback control. Figure 3.9 sketches the Archimedean spiral used to model the rolled tether in which ψ is the reel angular position. The general Archimedean equation is reported in Eq. (3.14) along with the specific equation that suits the case of a thin tether rolled around a reel:

$$r(\psi) = a + b\psi \;\Rightarrow\; r_{rol}(\psi) = r_0 + \frac{h}{2\pi}\psi \tag{3.14}$$

Once the radius is known as a function of the position angle also the rolled portion length of the tether can be related to ψ:

$$\begin{aligned} l_{rol}(\psi) &= \int_0^{\psi} \sqrt{r(\psi)^2 + \dot{r}(\psi)^2}\, d\psi = \\ &= \frac{1}{4\pi h}\left[(c_0 + h\psi)\sqrt{(c_0 + h\psi)^2 + h^2} - c_0\sqrt{h^2 + c_0^2} + \right. \\ &\quad \left. + h^2 \ln\left(\frac{c_0 + h\psi + \sqrt{(c_0 + h\psi)^2 + h^2}}{c_0 + \sqrt{h^2 + c_0^2}}\right)\right] \end{aligned} \tag{3.15}$$

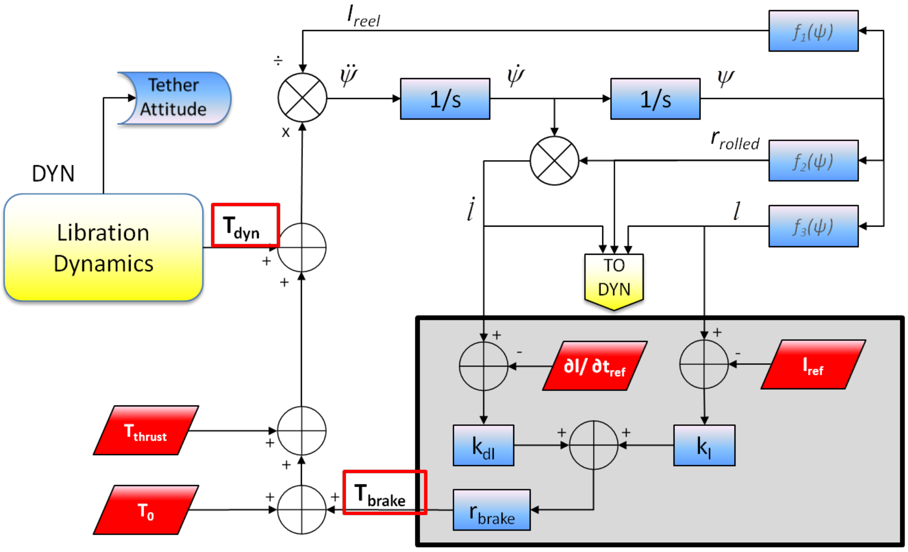

Figure 3.10: operational scheme of DDS. In evidence, the PD brake control feedback loop (gray block).

where $c_0 = 2\pi r_0$ and h is the tether thickness. The tether length rate during deployment can be easily calculated through Eq. (3.16):

$$\dot{l} = r_{rol}\dot{\psi} = \left(r_0 + \frac{h}{2\pi}\psi\right)\dot{\psi} \tag{3.16}$$

In this manner it is possible to express both the length and the speed of the tether as functions of the reel position angle and its derivative. Consequently, in the dynamics equations of the reference trajectories, l and $\dot{l}$ will be substituted with ψ and $\dot{\psi}$, respectively.

3.3.2 Proportional-Derivative feedback loop

Figure 1.6 shows the scheme of the PD brake control feedback loop that has been implemented in the DDS. The loop is based on the reel dynamics integration. Once the integrator has provided the actual reel position angle and the reel angular velocity, the instantaneous value of tether length and speed can be calculated through Eqs. (3.15) and (3.16). In Fig. 1.6 these equations are ideally contained in the three blocks labeled with $f_1(\psi)$, $f_2(\psi)$, and $f_3(\psi)$. When l and $\dot{l}$ have been calculated, libration dynamics is computed (inside the yellow block) to provide the actual tether attitude. At the same time, instantaneous length and speed of the tether are used in the feedback block (the light gray block) to compare them with the reference time profiles provided by the reference trajectories, that are represented in the figure by the input red parallelogram-shaped block. In this block, the brake control system will generate the T_{brake} torque following the linear control law given in Eq. (3.20). This component will be added to all other external torques, that is the reel friction, the propulsion system thrust, and gravitational and inertial components. The sum of all external torques is then divided by the instantaneous reel inertia providing to the integrator the instantaneous reel angular acceleration. The loop continues until the deployment is completed. Worth to be underlined is the fact the PD feedback only uses the length and the length rate time profiles obtained through the reference trajectories optimization while it does not use the brake friction reference time profile, which was used in the numerical optimization only as input for the Nelder-Mead algorithm. Equations (3.17)-(3.20) provide the external torques computed at each integration step:

$$\begin{aligned} T_{dyn} &= \frac{l\,(2m_B+\rho l)-\rho\dot{l}^2}{2\,(m_B+\rho l)}\left[c^2\varphi\left(\left(\omega+\dot{\vartheta}\right)^2+3\omega c^2\vartheta\right)+\dot{\varphi}^2\right]\cdot r_{rol} && (3.17)\\ T_{thrust} &= F_{thrust}\cdot r_{rol} && (3.18)\\ T_0 &= F_0\cdot r_{bearing} && (3.19)\\ T_{brake} &= \left[k_l\,(l-l_{ref})+k_{dl}\left(\dot{l}-\dot{l}_{ref}\right)\right]\cdot r_{break} && (3.20) \end{aligned}$$

where l and $\dot{l}$ are previously computed by means of Equations (3.15) and (3.16). The rolled radius is given by Eq. (3.14), $r_{bearing}$ and r_{break} are constants that depend on the deployer geometry, l_{ref} and $\dot{l}_{ref}$ are from the reference trajectories and k_l and k_{dl} are the proportional and derivative gains of the PD control. Their values were chosen as follows:

$$\begin{aligned} k_l &= 10^{-2}\,kg/s^2\\ k_{dl} &= 5\cdot 10^{-1}\,kg/s \end{aligned}$$

Let us spend a few words on the PD control gains. In this work their values have been chosen as the minimum values that guarantee the controlled trajectories to have a good tracking of the reference trajectories. This procedure is suitable for this preliminary study. A more rigorous procedure should take into account the transfer function of the brake system that, at the present time, is not available. However, the values used in this work are in line with those adopted in [4] in which an analysis of the control system response over the deployment phase was conducted A perturbation term was introduced in the in-plane libration dynamics equation to simulate a thruster misalignment with the longitudinal tether axis. In Eq. (3.21) α is the periodic component, β is the secular component of the misalignment:

$$M_{thrust}=F_{thrust}\cdot l\sin\left(\alpha\sin\left(\omega_{trhust}\cdot t\right)+\beta\right) \tag{3.21}$$

where M_{thrust} is the torque generated by the thruster misalignment which arm is equal to the instantaneous tether length l and ω_{thrust} is the frequency of the periodic oscillation. These two variables will be used in the error sensitivity analysis. It must be pointed out that the only way to have a secular component in the misalignment term is to have the tip mass not spinning about the longitudinal line. Considering that a long tether does not have any torsional stiffness, this condition is very unlikely to happen. A very small external perturbation or a small thruster misalignment will be sufficient to make the tip mass spinning about its longitudinal axis, thus averaging out the effects of all thruster misalignment. Anyway, regardless to the fact that β angle is not an issue, we studied its potential effect on the deployment libration stability. After all the steps described through equations from (3.12) through (3.21), the dynamics set of Equations (3.9)-(3.11) used in the RETRO tool have been transformed as reported in the followings:

$$\ddot{\vartheta} = \left(\omega + \dot{\vartheta}\right)\left[2\dot{\varphi}\tan\varphi - 3\frac{\dot{l}}{l}\frac{(2m_B + \rho l)}{(3m_B + \rho l)}\right] - 3\omega^2 s\vartheta c\vartheta + \frac{3M_{thrust}}{l^2(3m_B + \rho l)c^2\varphi} \tag{3.22}$$

$$\ddot{\varphi} = -3\frac{2m_B + \rho l}{3m_B + \rho l}\dot{\varphi}\frac{\dot{l}}{l} - s\varphi c\varphi\left[3\omega^2 c^2\vartheta + \left(\omega + \dot{\vartheta}\right)^2\right] \tag{3.23}$$

$$\ddot{\psi} = \frac{(T_{dyn} + T_0 + T_{thrust} + T_{brake})}{I_{reel}} \tag{3.24}$$

Equations (3.22) and (3.23) represent the libration dynamics whereas the last Eq. (3.24) describes the reel angular motion.

3.3.3 Controlled trajectories: reference cases (zero-error cases)

In this section the results obtained with the DDS simulator are reported. In particular, the zero-error cases are considered, that is assuming the same conditions as in the four reference cases listed in Table 3.1. Before analyzing the system sensitivity to external perturbations/errors, in fact, we need to know if the PD control can guarantee a correct tether deployment under ideal conditions, precisely under the reference cases conditions with no external perturbations nor initial attitude errors. In Figure 3.11 the black points represent the tip mass end-of-deployment position in the PD-controlled cases, whereas the blue circles represent the tip mass final positions in the reference trajectories. As it can be noted, the black points are always inside the blue circles. This means that the PD brake control law works very well in all reference conditions.

Figure 3.12 shows various results obtained from DDS simulations of CASE 4. The solid black lines (PD-controlled) are always superimposed to the dashed blue lines (references), with the only exceptions of the length rate and brake friction profiles. Nevertheless, this does not represent an issue: the fact that the deployment ends with a speed not perfectly equal to zero can be easily solved by making the brake to increase its friction action while deploying the last hundreds meters of the tether. The controlled brake time profile differs from the reference one for two reasons: first, the equations implemented in RETRO do not take in account that the arm of the unwinding torque changes during the deployment (solid black line of Fig. 3.12-C); second, the brake profile in RETRO was given through a spline interpolation of a discrete number of pivot points, whereas in the

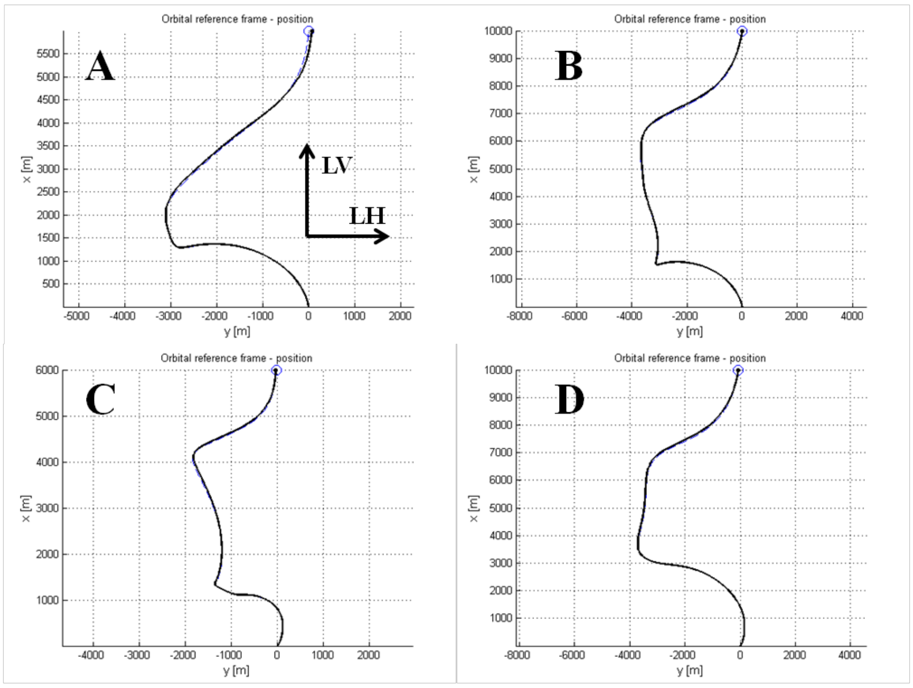

Figure 3.11: results from zero-errors condition simulations. The four plots report the controlled trajectories together with the respective reference trajectories for all the reference cases (in order, A - case 1, B - case 2, C - case 3, D - case 4). The solid black line is the PD-controlled trajectory, the dashed blue line is the reference trajectory.

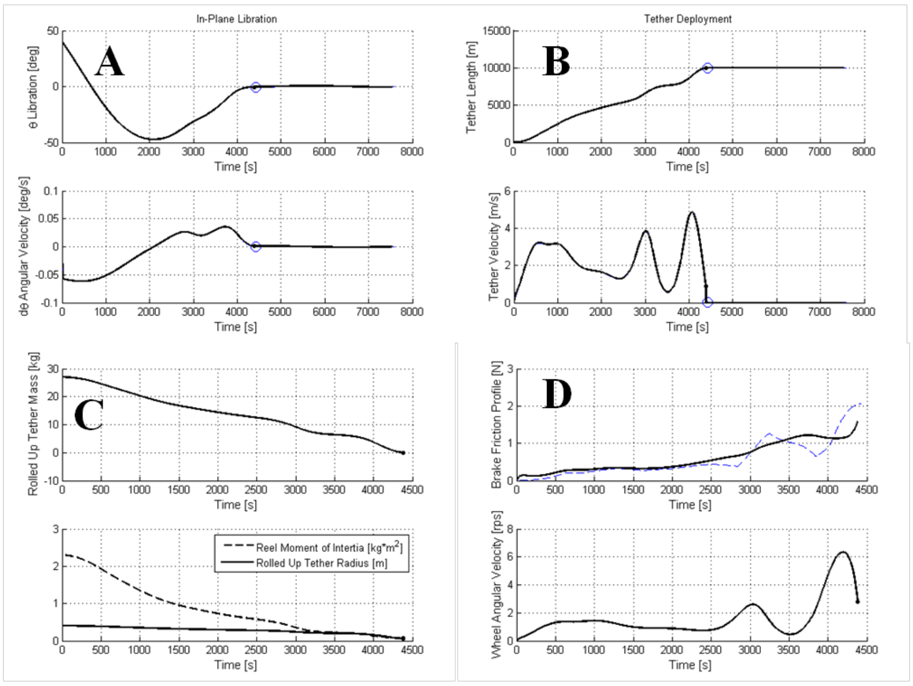

Figure 3.12: time profiles from PD-controlled simulations for CASE 4, solid black lines refers to PD-controlled trajectory, dashed blue line referes to reference trajectories. A) tether attitude; B) tether length and speed profiles; C) reel mass and geometrical parameters; D) brake friction and reel angular velocity time profiles.

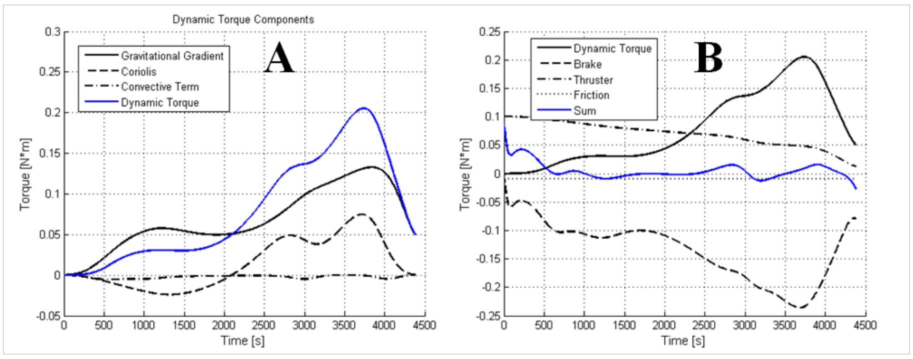

Figure 3.13: external torques time profiles: A) dynamic torque components; B) all torques.

deployment simulator it is computed at each integration step. Furthermore, the brake time profile is not used in the feedback loop, thus the difference between reference and PD-controlled brake profiles does not represent a problem. Figure 3.13 shows the trends of the dynamic torque (panel A) and of all external torques (panel B). Something interesting is here evidenced: as already stated above, the convective term produces a negligible torque, the gravitational and the centrifugal terms are always positive whereas the Coriolis term is negative at the beginning of the maneuver. Although the sum of all dynamic components is always positive it can be noted that when the Coriolis term become positive after about 2000s from the start of deployment the dynamic torque grows quickly and considerably. This change in the dynamic torque profile is in correspondence of the first "curve" in the trajectory. This is a critical point of the deployment maneuver because at this point the length of unwinded tether is still not enough to guarantee a strong gravity gradient force and the in-plane libration angle is large. Figure 3.13-B also shows that after 2000s the dynamic torque becomes about five times higher than the reel friction value. In summary, we can speculate that after the tip mass has undergone its first "sudden curve" along its trajectory, that is about after 2000-2500 s from the beginning of the maneuver, the gravity gradient could be sufficient to carry out deployment without the aid of the in-line thruster. This, in turn, could lead to a significant saving of propellant mass. This hypothesis was preliminary validated through some dedicated simulations, the results of which are reported in Section 3.5.

3.4 Error Sensitivity Analysis

In this section the most important results of the error sensitivity analysis are reported. The analysis was conducted on the main system parameters and is divided in two parts. In the first part an error on one reference variable at a time was introduced. More precisely, the conditions of the tether at end of the deployment were studied in the case one variable among those listed below was altered with respect to the reference conditions (Table 3.1):

- initial in-plane angle ϑ_0: spacecraft attitude control pointing errors were assumed not to exceed the conservative value of 5°;
- initial out-of-plane angle φ_0: same as for ϑ_0;
- propulsion thrust F_{thrust}: a thrust error up to -50% was assumed;
- reel friction F_0: reel friction is very relevant to deployment dynamics; to be conservative, deployment maneuver was studied when a friction force error up to 50% is introduced;
- periodic thruster misalignment α: up to 20°;

- secular thruster misalignment β: as discussed in the previous Section 3.3.2 this variable is not going to be an issue in an operative mission; for this reason a maximum variation of ±3° was considered.

In the second part of the error sensitivity analysis all the previous variable errors were combined in a reasonable “worst case” set of errors/perturbations.

3.4.1 Single-variable error analysis

In the following tables the results of the error sensitivity analysis are reported. In each table it is possible to compare the final attitude conditions in the $\vartheta_0 = 0°$ and the $\vartheta_0 = 40°$ cases, first for the 6-km cases and then for the 10-km cases. The results reported in Table 3.9 and Table 3.10 are the maximum in-plane amplitudes (in degrees) reached by the tether after the deployment is completed, i.e. the so-called *residual libration*. This measure gives us an idea on the quality of the deployment process: if the maximum in-plane angle after deployment is close to zero it means the maneuver ended with a correct attitude of the tether. The out-of-plane angle was not taken into account because the motion on this plane is much more stable than in the in-plane and, moreover, by ejecting the tip mass in the orbital plane (with errors) the out-of-plane dynamics is almost negligible. The *REF* column shows the maximum angles for the zero-error cases which are taken here as reference values. Analyzing the results, it can be firstly noticed that the 10-km cases are in general less sensitive to errors and external perturbations than the 6-km cases. This is because in the 10-km cases the tether has a longer time to acquire a correct attitude after the first critical “curve”. Apart from this, the results show that the final tether attitude conditions have a significant sensitivity to only two perturbations: the initial in-plane ejection angle error $\Delta\vartheta_0$ (Figures 3.14 and 3.15) and the secular thruster misalignment β (Figures 3.16 and 3.17). However, the latter one is only a theoretical error, as it was previously stated. On the contrary, the errors on initial out-of-plane angle $\Delta\varphi_0$, thrust error ΔF_{thrust}, reel friction error ΔF_0, and the periodic thruster misalignment α do not influence noticeably the final tether attitude.

The most important result, in any case, is the fact that if the deployment begins with an initial ejection in-plane angle of 40° (CASES 2 and 4) the sensitivity of the tether to any error or external perturbations is reduced almost to zero. As it has been stated above, simulations were also carried out for initial in-plane angle values of 20° and 60° but the results obtained were not as good as in the 40° case (see [2]). This result is also consistent with the fact that the sensitivity is higher for negative errors of initial in-plane angle ϑ_0: a qualitative explanation is that in the first part of the deployment (more or less during the first 2000-2500s) the in-plane angle becomes negative with respect to the initial angle and, consequently, if the tip mass is ejected at +40° with respect to LV this negative values is significantly reduced. Concerning the β angle, tether sensitivity to this parameter is very high because it introduces a significant constant perturbation torque throughout deployment. Although the things are much better in the 40°-

Table 3.9: **single variable error analysis results for 6-km long tethers (CASES 1 and 2)**

$\Delta\vartheta_0$	-5°	-3°	-2°	-1°	REF	+1°	+2°	+3°	+5°
CASE 1	31.18	13.92	8.00	3.35	0.70	3.46	5.99	8.08	11.3
CASE 2	1.16	0.82	0.64	0.46	0.29	0.14	0.18	0.36	0.79

(a) residual libration for initial in-plane angle errors.

$\Delta\varphi_0$	-5°	-2°	-1°	REF	+1°	+2°	+5°
CASE 1	0.66	0.40	0.13	0.00	0.13	0.40	0.66
CASE 2	0.28	0.28	0.29	0.29	0.29	0.28	0.28

(b) residual libration for initial out-of-plane errors.

ΔF_{thrust}	-50%	-30%	-15%	REF	+15%	+30%	+50%
CASE 1	0.54	0.42	0.51	0.70	0.95	1.20	1.54
CASE 2	0.24	0.26	0.27	0.29	0.31	0.33	0.35

(c) residual libration for thruster force errors.

ΔF_0	-50%	-30%	-15%	REF	+15%	+30%	+50%
CASE 1	0.80	0.75	0.73	0.70	0.67	0.65	0.61
CASE 2	0.3	0.3	0.29	0.29	0.29	0.28	0.28

(d) residual libration for reel friction force errors.

α	REF	+1°	+2°	+5°	+20°
CASE 1	0.70	1.00	1.63	3.41	9.76
CASE 2	0.29	0.24	0.24	0.14	0.58

(e) residual libration for periodic misalignment errors.

β	<-2°	-2°	-1°	-0.5°	REF	+1°	+2°	+5°
CASE 1	🟥	🟥	🟥	28.32	0.70	19.26	24.56	26.11
CASE 2	🟥	44.05	4.82	-	0.29	3.12	4.58	4.52

(f) residual libration for secular misalignment errors.

Table 3.10: single variable error analysis results for 10-km long tethers (CASES 3 and 4)

$\Delta\vartheta_0$	-5°	-3°	-2°	-1°	REF	+1°	+2°	+3°	+5°
CASE 3	17.52	6.57	3.75	1.73	0.22	1.00	2.00	2.86	4.3
CASE 4	0.31	0.37	0.42	0.49	0.56	0.64	0.73	0.82	1.02

(a) residual libration for initial in-plane angle errors.

$\Delta\varphi_0$	-5°	-2°	-1°	REF	+1°	+2°	+5°
CASE 3	0.37	0.28	0.23	0.22	0.23	0.28	0.37
CASE 4	0.59	0.57	0.56	0.56	0.56	0.57	0.59

(b) residual libration for initial out-of-plane errors.

ΔF_{thrust}	-50%	-30%	-15%	REF	+15%	+30%	+50%
CASE 3	0.79	0.38	0.31	0.22	0.13	0.06	0.10
CASE 4	0.66	0.61	0.58	0.56	0.52	0.49	0.46

(c) residual libration for thruster force errors.

ΔF_0	-50%	-30%	-15%	REF	+15%	+30%	+50%
CASE 3	0.20	0.22	0.21	0.22	0.22	0.24	0.25
CASE 4	0.53	0.56	0.54	0.56	0.55	0.56	0.56

(d) residual libration for reel friction force errors.

α	REF	+1°	+2°	+5°	+20°
CASE 3	0.22	0.57	0.57	1.29	4.38
CASE 4	0.56	0.57	0.60	0.66	1.04

(e) residual libration for periodic misalignment errors.

β	-3°	-2°	-1°	-0.5°	REF	+1°	+2°	+5°
CASE 3	🟥	🟥	🟥	13.68	0.22	7.61	11.90	16.44
CASE 4	22.62	9.21	3.44	-	0.56	1.27	2.18	2.72

(f) residual libration for secular misalignment errors.

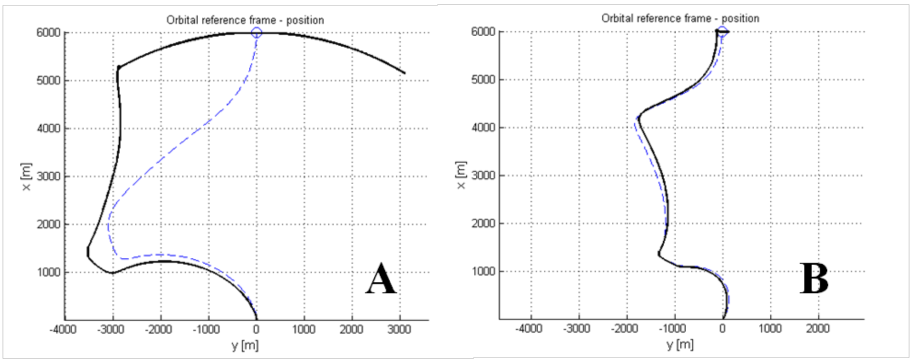

Figure 3.14: 6-km long tether cases, PD-controlled trajectories (solid black) adherence with reference trajectories (dashed blue) with $\Delta\vartheta_0 = -5^\circ$ error. A) CASE 1, $\vartheta_0 = 0^\circ$; B) CASE 2, $\vartheta_0 = 40^\circ$.

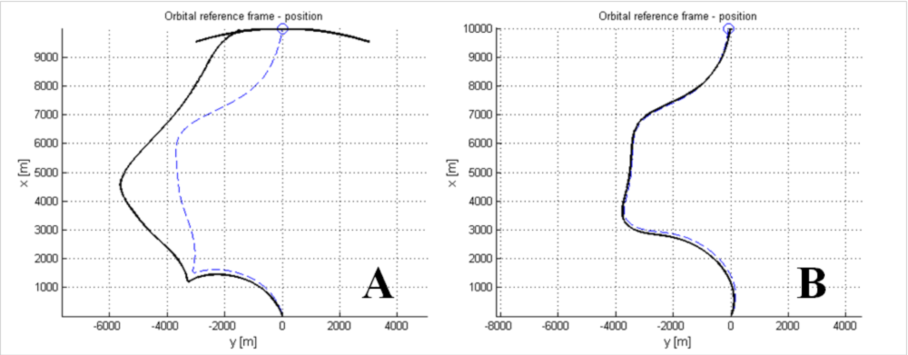

Figure 3.15: 10-km long tether cases, PD-controlled trajectories (solid black) adherence with reference trajectories (dashed blue) with $\Delta\vartheta_0 = -5^\circ$ error. A) CASE 3, $\vartheta_0 = 0^\circ$; B) CASE 4, $\vartheta_0 = 40^\circ$.

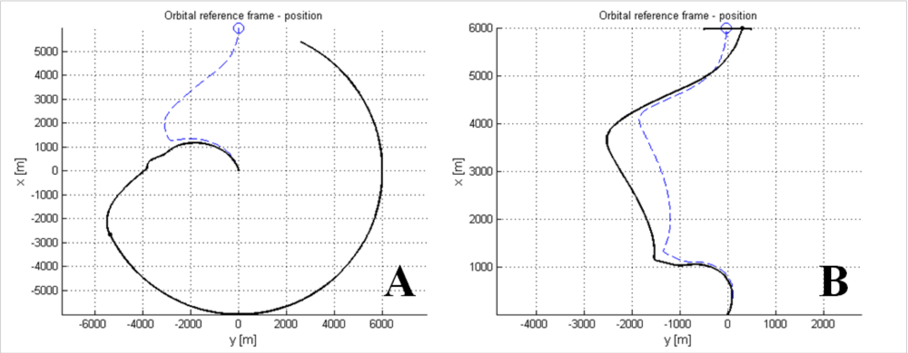

Figure 3.16: 6-km long tether cases, PD-controlled trajectories (solid black) adherence with reference trajectories (dashed blue) with $\beta = -1^\circ$ error. A) CASE 1, $\vartheta_0 = 0^\circ$; B) CASE 2, $\vartheta_0 = 40^\circ$.

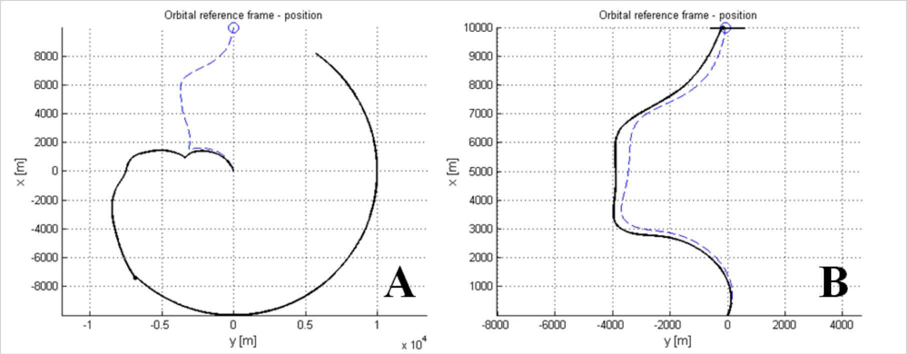

Figure 3.17: 10-km long tether cases, PD-controlled trajectories (solid black) adherence with reference trajectories (dashed blue) with $\beta = -1°$ error. A) CASE 3, $\vartheta_0 = 0°$; B) CASE 4, $\vartheta_0 = 40°$.

cases, we remind once again that secular misalignment is very unlikely to occur as the tip mass will surely spin about the tether longitudinal axis (as it was reported in previous tether missions with a non-stabilized tip mass), thus averaging every thruster misalignment errors around the zero bias.

3.4.2 Worst cases analysis

Table 3.11 reports the combination of error/perturbations that were chosen to represent the "worst case" condition. Figure 3.18 and 3.19 show once again the great improvement in error insensitivity that takes place passing from 0° to 40° values of the initial in-plane angle.

Table 3.11: combination of error and external perturbations for the worst case scenario.

WORST CASE	$\Delta\vartheta_0$	$\Delta\varphi_0$	ΔF_{thrust}	ΔF_0	α	β
VALUE	-2°	+2°	-30%	+50%	+5°	-0.5°

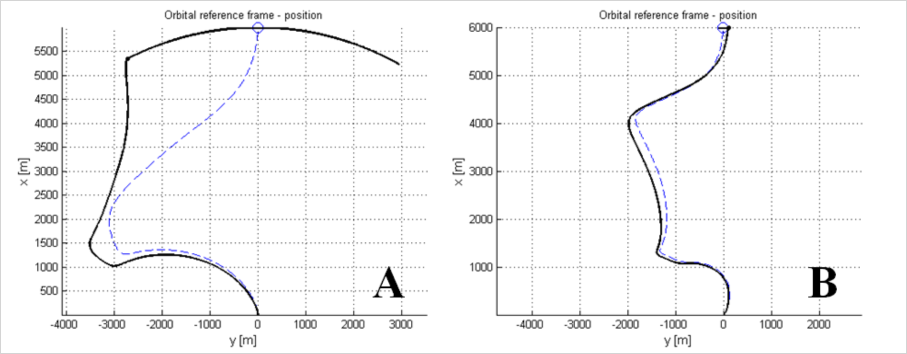

Figure 3.18: 6-km long tethers, PD-controlled trajectories (solid black) adherence with reference trajectories (dashed blue) with worst case error combination. A) CASE 1, $\vartheta_{max} = 29.36°$; B) CASE 2, $\vartheta_{max} = 1.09°$.

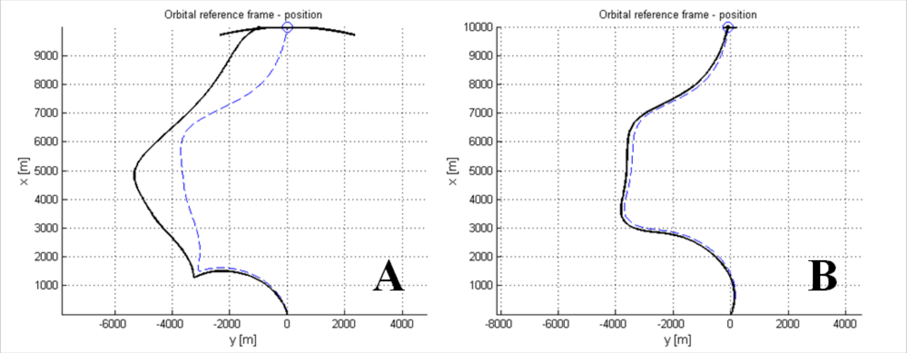

Figure 3.19: 10-km long tethers, PD-controlled trajectories (solid black) adherence with reference trajectories (dashed blue) with worst case error combination. A) CASE 3, $\vartheta_{max} = 13.56°$; B) CASE 4, $\vartheta_{max} = 1.35°$.

3.5 The Limited Firing Time Case

Analyzing the results obtained from zero-errors cases (Par. 3.3.3) it has been noticed that, at a certain point of the deployment maneuver, the torque due to gravity gradient, Coriolis and centrifugal terms, becomes much bigger than the torque originated by the reel friction. More precisely, a preliminary studies show that after about 2000 seconds from the beginning of the maneuver the thrusters can be safely turned off because gravity gradient and centrifugal forces are sufficient to conclude the deployment. This means that for more than half of the deployment maneuver the aid of the propulsion system is not necessary, thus saving a significant amount of propellant mass and volume of the propulsive system. Figure 3.20 shows the result of a simulation carried out under worst case conditions described in Table 3.11 for the CASE 2 (6-km tether, in-plane initial angle equal to 40°). In this simulation the thruster was turned off after 2000 s from the beginning of the maneuver. The residual libration is equal to 0.76°, that is the tether ends up almost perfectly aligned with the local vertical. Figure 3.20-B shows the trends of all external torques during deployment. Please note that the brake feedback control reacts at the switching off of the thruster: the brake torque (black dashed line) is almost instantaneously reduced to zero at t = 2000 s and is starts to grow again after some time to counteract the ever growing dynamic torque.

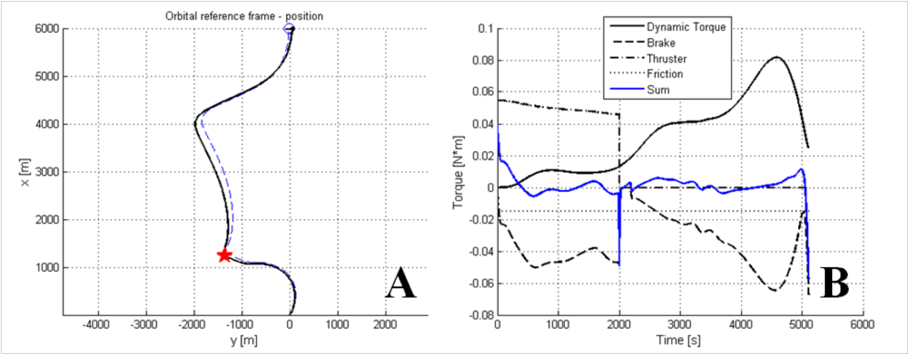

Figure 3.20: simulation with 2000-s limited firing time, worst case conditions for CASE 2. Red star indicates the point at which thruster was turned off. A) Trajectory adherence; B) Torques trends throughout the maneuver.

3.6 Conclusions

This work addresses key issues relative to the thrust-aided deployment of a multi-km tape-shaped tether in space by means of a librating maneuver. In particular, the study was conducted on a proposed system configuration that utilizes a reeling passive deployer equipped with a closed-loop controlled brake system and a low-thrust propulsion system on board the tip mass, which are suitable for deploying tape tethers. The control strategy involves the use of a feed-forward reference trajectory and a feedback proportional-derivative control law. A family of length-velocity reference trajectories that guarantee a correct deployment of tape tethers with total length of 6km and 10km were found utilizing the Nelder-Mead numerical optimization algorithm. Furthermore, the set of reference trajectories covers several values of the initial tip mass ejection angle, that is, ϑ_0 =0, 20, 40, and 60deg. For all the cases analyzed, the residual libration amplitudes of the tether about the local vertical at the end of deployment were minimized (in all cases $\vartheta_{end} <$ 1deg) to provide the tether system with the highest dynamic stability margin during deorbiting of the mother spacecraft. Subsequently, the sensitivity of the system to errors and external perturbations was tested by means of a specialized software to find an initial in-plane angle equal to 40deg (measured from local vertical toward the satellite flight direction) provides a robust deployment tolerant of worst-case errors combination.

Bibliography

[1] Zanutto, D., Pertile, M., and Lorenzini, E.C., *Deployment Control Survey*, Deliverable D212.1 for FP7-SPA.2010.2.3-2, November 2012.

[2] Mantellato, R., and Lorenzini, E.C., *Deployment Control Survey*, Deliverable D212.2 for FP7-SPA.2010.2.3-2, May 2013.

[3] Mantellato, R., Zanutto, D., Pertile, M., Colombatti, G., and Lorenzini, E.C., *Tether Dynamics Survey*, Deliverable D13.2 - final for FP7-SPA.2010.2.3-2, January 2014.

[4] Lorenzini, E.C., Bortolami, S.B., Rupp, C.C., and Angrilli, F., *Control and Flight Performance of Tethered Satellite Small Expendable Deployment System-II*, Journal of Guidance, Control, and Dynamics, Vol. 19, No. 5, Sept.-Oct. 1996, pp. 1148-1156. doi: 10.2514/3.21757

[5] Peláez, J., Lorenzini, E. C., López-Rebollal, O., and Ruiz, M., *A New Kind of Dynamic Instability in Electrodynamic Tethers*, Journal of the Astronautical Sciences, Vol. 48, No. 4, 2000, pp. 449-476.

4 An Optimization Method for BET Systems

At a first glance, a deorbit device that makes use of an electrodynamic tether to drag a spacecraft down into the atmosphere may appear to be a simple system. It basically consists of a long tether, a cathode, some simple electronic, and an inert tip mass and the system is meant to be entirely passive and autonomous. Indeed, the reality is quite different. The tethered system needs a deployer to be deployed in a proper way before electric current can start to flow inside it, which dimensions and weight depends on the tether length, thickness, and width. A remarkable portion of the tether length must be non-conductive for dynamical stabilization purposes and the amount of this fraction depends on several variables, e.g. the starting orbit altitude and inclination, the tip mass, the average electric current flowing in the conductive portion of the tether. In turns, the electric current and the probability to have the tether cut by space debris (i.e. the system reliability) depend on tether geometry and orbital parameters. Moreover, also the mass and volumetric characteristics of the electronic box, cathode, and tip mass subsystems depend on all the other components, making an electrodynamic tether system difficult to be optimized. Table 4.1 shows a qualitative description of the interdependency of BETs subsystems together with cut probability and deorbit time. The table is built answering the following question: *if one subsystem configuration is fixed giving it as an input, how much does it directly influence the other subsystems?* It is easy to see by inspection that almost all subsystems are interdependent with several other subsystems. Moreover, most of the dependencies are classified as strong, and, in particular, all of table items has at least one strong relation with another subsystem. Table 4.1 also highlights that the most important component of a BET system is with no doubt the conductive tether that influences all other subsystems characteristics. Other important subsystems are the inert portion of the tether, the tip mass, and the stabilization strategies, whereas the subsystems that affect a least number of subsystems are the electronic, the cathode, and deployer together with the deorbit time. In any case, the most important thing that we can infer from Table 4.1 is that the change of the characteristics of a single subsystem affects at least another subsystem, giving birth to a chain reaction that can, in some cases, influence the whole BETs system. As a representative example, let us suppose to change the conductive portion of the tether configuration by extending its length and doubling its cross section. This would lead to shorter deorbit time and higher cut probability. Moreover, the inert portion of the tether should be increase in length

Table 4.1: Interdependency of BETs subsystems (how much first column depends on first row items). Yellow color indicates weak dependences, red color strong dependences. The *Stabilization strategies* row group additional devices meant to stabilize tether dynamic, such as rotational dampers, shock absorbers, current control algorithms.

	Deployer	Conductive tether	Inert tether	Tip mass	Cathode	Electronic	Stabilization strategies	Cut probability	Deorbit time
Deployer	-	🟥	🟥						
Conductive tether	🟥	-		🟨	🟥	🟨	🟥	🟥	🟥
Inert tether	🟥	🟥	-	🟥			🟥	🟥	
Tip mass		🟥	🟨	-			🟥		
Cathode		🟥			-	🟥			
Electronic		🟥			🟥	-	🟥		
Stabilization strategies		🟥	🟥	🟥			-		
Cut probability		🟥	🟥					-	🟥
Deorbit time		🟥	🟨				🟨	🟥	-

roughly by the same amount of the conductive one the tip mass together with all other stabilization strategies must be adjusted to guarantee a proper dynamic stability during deorbitng. Finally, the deployer size would increase considerably to be able to store a longer tether, whereas the electronic and the cathode shoud be redimensioned to deal with higher electric currents.

In this chapter we attack the problem of finding an optimized configuration of a BETs system when a mission profile and system requirements are provided. The work here presented was conducted in close collaboration with our partners at the Technical University of Madrid (Universidad Politécnica de Madrid, UPM) whom developed an optimization analytical algorithm and a simple simulation software that can be usefully used to discard most of improper BETs configurations in a realist end-of-life deorbiting mission.

Table 4.2: Optimization process input and output.

Initial input	Final output
Orbit height (H_0)	Conductive tether geometry and mass ($L_c \times w \times h$, m_c)
Orbit inclination (i)	Tip mass (m_B)
	Inert tether geometry and mass ($L_i \times w \times h$, m_i)
	Deployer mass and volume (m_D, V_D)
	Cathode mass and volume (m_C, V_D)
	Electronic box mass (m_E)
	Rotational damper parameters (if needed)
	Shock absorber parameters (if needed)
	Current control parameters (if needed)

4.1 Overview of the method

The process devised within the present work aims to optimize a bare electrodynamic tether system when a mission profile is provided as an input. The main output of the optimization are the conductive tether geometry and the tip mass, whereas secondary results are the mass and/or the geometry of inert tether, deployer, electronic box and cathode mass, and the stabilization devices configuration. Table 4.2 summarizes the initial input and final output of the process. The optimization process was designed taking into account all the work that has been done within the *BETs Project*, in particular the two simulation software, BETsMA, developed at UPM, and Flexible Tether Simulator (FTS), developed at UniPD. [1, 2, 3]

The optimization method is composed of three main steps. The first step consists of a preliminary analysis carried out by means of BETsMA optimization module that implements a semi-analytical algorithm to find the optimized BET configuration for a given set of input variables such as orbit altitude, inclination, satellite mass. As a second step, once the optimized configuration has been found, BETsMA deorbiting module simulates the deorbiting maneuver making use of a simplified tether model; in particular, it assumes a rigid tether aligned with the local vertical. BETsMA deorbiting module outputs include deorbit time, tether survival probability, satellite trajectory and mass of BET main subsystems, like the hollow cathode, deployer subsystem and electric module. Finally, in the third step the results obtained from BETsMA are used as input in the FTS that utilizes a more complex model that takes into account both lateral and longitudinal motion of the tether along with all the latest environment routines. Within this step several stabilization strategies can also be simulated by means FTS dedicated tools (e.g. inert portion of tether, rotational damper, shock absorber), thus the simulations results are much more accurate than those found in the second step. Deorbit time, tether attitude, tether tension, tether temperature, current profile, and orbit propagation are calculated with relative high accuracy throughout deorbiting maneuver. Subsequent numerical simulations carried out with FTS are used to gradually refine the tether system configuration. If an acceptable set of results is not obtained at the end of the refinement process (e.g. because of insufficient dynamical stability, excessive deorbit time), the optimization process must be restarted at step 1 and a different conductive tether geometry must be selected (e.g. longer tether, narrower cross section, thicker tether) and the new configuration must go through the procedure again. The iterative process stops when results obtained with FTS are acceptable. It must be clear since now that the BET optimization process described in this chapter does not provide an unique optimal configuration, indeed different choices made at step one and two can lead to different acceptable "optimal" configurations at step three. For this reason, user's experience together with a good knowledge of tethered system are crucial to obtain good results. Unluckily, as explained above, BET systems complexity does not allow (up to now) for an easy and unique optimization process. Nonetheless, the devised procedure here described is unquestionably a useful tool to the user that would like to pinpoint suitable solutions to the essential question that troubles BET deorbiting systems designers:

> *for a given mission profile, which is the best system configuration to provide reliable and competitive deorbit performances?*

In the next sections we provide an example of an optimization procedure for a selected practical case. The orbit profile defined in Par. 4.1.3 is used as input. The results of the optimization process are shown in Par. 4.2. The two software utilized in the study are briefly described in the following two subsections.

4.1.1 BETsMA

The software BETsMA is divided in two modules. The first, the *Optimization Module*, utilizes a semi-analytical algorithm developed by Sanmartin *et al.* [4] to find the tether geometry (width, thickness, and length) that minimizes certain objective functions involving tether-to-spacecraft mass ratio, cut probability, and deorbit time for given values of the starting orbit and the spacecraft mass. Tether geometry is of primary importance impact on the mission performance. For example, longer tethers provide faster deorbiting but increase both front area exposed to debris impacts and tether mass, and the high electrodynamic forces can induce serious dynamical instability eventually leading to catastrophic failures. Tether figures of merit, like cut probability by tether-to-spacecraft mass ratio, are written as integrals from the initial to the final altitude. The functions inside the integral depend on tether geometry because they involve physical models like survivability against debris impact and tether current profile. At each altitude, these functions are evaluated by making an average over many orbital periods; a rigid bare tether aligned with the local vertical that carries out a sequence of quasi-circular orbits along the deorbiting maneuver is also assumed.While using

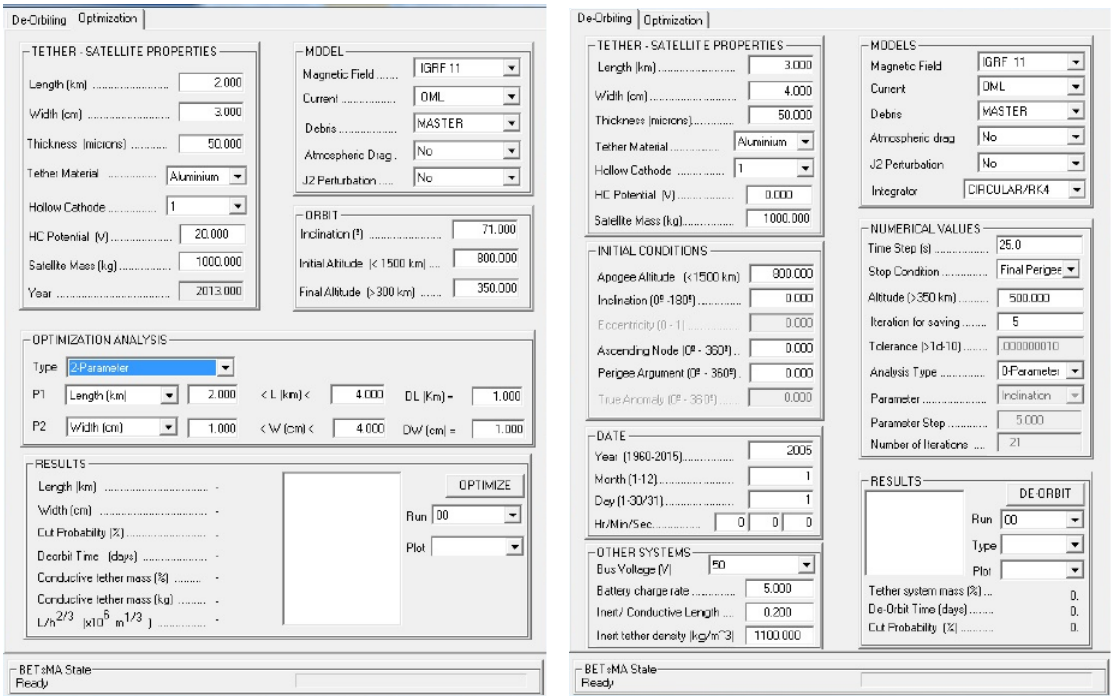

TETHER - SATELLITE PROPERTIES
Length (km) 2.000
Width (cm) 3.000
Thickness (microns) 50.000
Tether Material .... Aluminium
Hollow Cathode 1
HC Potential (V) 20.000
Satellite Mass (kg) 1000.000
Year 2013.000

MODEL
Magnetic Field ...... IGRF 11
Current .... OML
Debris .... MASTER
Atmospheric Drag . No
J2 Perturbation .... No

ORBIT
Inclination (º) 71.000
Initial Altitude (< 1500 km) 800.000
Final Altitude (> 300 km) 350.000

OPTIMIZATION ANALYSIS
Type 2-Parameter
P1 Length (km) 2.000 < L (km) < 4.000 DL (Km) = 1.000
P2 Width (cm) 1.000 < W (cm) < 4.000 DW (cm) = 1.000

RESULTS
Length (km) .... -
Width (cm) .... -
Cut Probability (%) .... -
Deorbit Time (days) .... -
Conductive tether mass (%) .... -
Conductive tether mass (kg) .... -
$L/h^{2/3}$ ($\times 10^6$ $m^{1/3}$) .... -
Run 00
Plot

BETsMA State
Ready

TETHER - SATELLITE PROPERTIES
Length (km) 3.000
Width (cm) 4.000
Thickness (microns) 50.000
Tether Material .... Aluminium
Hollow Cathode 1
HC Potential (V) 0.000
Satellite Mass (kg) 1000.000

INITIAL CONDITIONS
Apogee Altitude (<1500 km) 800.000
Inclination (0º -180º) 0.000
Eccentricity (0 - 1) 0.000
Ascending Node (0º - 360º) .. 0.000
Perigee Argument (0º - 360º) . 0.000
True Anomaly (0º - 360º) 0.000

DATE
Year (1960-2015) 2005
Month (1-12) 1
Day (1-30/31) 1
Hr/Min/Sec. 0 0 0

OTHER SYSTEMS
Bus Voltage (V) 50
Battery charge rate 5.000
Inert/ Conductive Length 0.200
Inert tether density (kg/m^3) 1100.000

MODELS
Magnetic Field IGRF 11
Current OML
Debris MASTER
Atmospheric drag No
J2 Perturbation No
Integrator CIRCULAR/RK4

NUMERICAL VALUES
Time Step (s) 25.0
Stop Condition .... Final Perigee
Altitude (>350 km) 500.000
Iteration for saving 5
Tolerance (>1d-10) .... .000000010
Analysis Type 0-Parameter
Parameter .... Inclination
Parameter Step 5.000
Number of Iterations 21

RESULTS
Run 00
Type
Plot
Tether system mass (%) ... 0.
De-Orbit Time (days) .... 0.
Cut Probability (%) .... 0.

BETsMA State
Ready

Figure 4.1: User interface of the Optimization and Deorbit modules of BETsMA.

this module the user must make some choices regarding the maximum acceptable cut probability together with the possible tether width and thickness. Thus, more than one tether configuration can be pointed out from each optimization process. It should be clear at this point that the Optimization Module does not provide the absolute optimal tether geometry, indeed it is extremely useful to *discard* most of the unsuitable configurations and to individuate *narrow ranges* of suitable values of tether length and width for given cut probability values. The user's experience together with historical results on past tethered projects should be capitalized to complete the first optimization process and pinpoint the best conductive tether configuration to be used as input in the next optimization step which takes advantage of the FTS accurate tether model. The second module of BETsMA, the *Deorbiting Module*, utilizes a LV-pointing dumbbell model to obtain a more accurate computation of the deorbiting maneuver, providing deorbit time, probability of cut and an estimation of the mass of each subsystems. As opposed to the optimization tool, the deorbiting module does not assume circular orbit and it does not involve any average. The orbit is computed by using DROMO, a robust and efficient orbit propagator based on special perturbations methods [5]. The program also provides a preliminary mass budget for all the tether subsystems, which estimations are based on scaling algorithms provided by *BETs Project* consortium members. Figure 4.1 shows the user's interface of BETsMA modules. The interested reader is invited to refer to BETsMA manual for more details on the models used in the software.

4.1.2 Flexible Model Simulator

The FTS software was developed in FORTRAN at University of Padova by Dr. Denis Zanutto within BETs Project during his Ph.D (2010-2012) [3] and subsequently improved by Dr. Marco Pertile and the author of this thesis in the following years. The tether flexible model implemented in FTS is able to provide the user with accurate information on the deorbit of a spacecraft. The dumbbell model used in BETsMA is useful to quickly get early preliminary results for the integration of the dynamic equations is much faster. Nevertheless it says nothing about libration, lateral, and longitudinal dynamics of the tether, thus it is unable to predict dynamical instability of the system. Moreover, during the deorbit the tether is usually not aligned with the local vertical and, due to electrodynamic and aerodynamic drags, it bends laterally giving birth to the well known skip-rope motion, heavily influencing the efficiency of the electrodynamic drag. The flexible model is in turn able to provide the user with all of these information, together with more accurate deorbit time and orbit propagation, nevertheless paying a tribute in terms of higher computation time. Hereafter we describe briefly the FTS model, for more detailed information please refer to [3, 6]. The FTS implements a lump masses model, that is the tether is modeled with a number of lump masses connected with straight massless elastic elements (springs and dampers) to simulate lateral and longitudinal tether dynamics. Elements bending and torsional stiffness are not taken into account as they can be reasonably neglected for a tape-shaped tether. The characteristics of the orbit propagation model are described below:

- **Gravitational forces:** a 4x4 gravity potential harmonic expansion model is used to calculate the gravitational forces of each lump mass, mother satellite, and tip mass.

- **Electrodynamic forces:** the current collection is assumed to take place in the Orbital Motion Limited (OML) regime and the electric current and voltage profiles are calculated following an asymptotic formulation provided by Bombardelli. [7]

- **Thermal gradient:** temperature distribution along the conductive tether is important because it affects its electric and mechanical characteristics, thus influencing the electrodynamic interaction and eventually the system dynamic. Thermal fluxes originated by Sun, albedo, Earth, atmospheric drag, ionospheric electrons impact, and ohmic losses are considered.

- **Atmospheric density:** the NRLMSISE00 model is used to find air density to calculate air drag.

- **Earth magnetic field:** the IGRF model is used.

- **Ionospheric electron density:** the IRI2007 model is used.

Apart from environmental and lump masses dynamical models, some instability countermeasures have also been implemented in the code. In fact, experience matured through a copious number of simulations together with literature teaching tells us that we cannot have a dynamical stable BET configuration without adopting some strategies to limit inborn dynamical instabilities of an electrodynamic tether. The user can choose to simulate several stabilizing strategies:

- **Inert tether:** gravitational forces have a stabilizing effect on the tether as they always tend to restore the alignment with local vertical. With the scope of increasing these forces a non-conductive (inert) tether is introduced between the electrodynamic tether and the tip mass for the configuration with the cathode installed in the mother spacecraft.
- **Rotational mechanical damper:** a passive damping rotational damper located at the interface between the conductive tether and the mother spacecraft, like the ones described in Chapter 2, can be simulated.
- **Current control:** various current control strategies can be activated to prevent excessive amplitude of the electrodynamic forces.
- **Shock absorber:** electrodynamic forces amplitude and direction undergo (relative) quick and wide variations along the orbit with a strong dependence on orbit altitude. As a consequence of this, tether can experience high peak tension loads that help instability mechanisms to take place. A shock absorber can then be installed inside the tip mass with the scope of soften and damp tension peaks induced by sudden ED forces variations.

The numerical integration of the equation of motion is carried out with widely used commercial integrators, nonetheless the author has developed an *ad-hoc* implicit integrator based on a 5th order RADAU scheme in collaboration with Dr. Gonzalo Sánchez-Arriaga. The implicit integrator, named RIGON5, was designed to be 100% compatible with FTS FORTRAN code, and it has proven to be useful (sometimes indispensable) when dealing with relative short tethers combined with high electrodynamic forces. In this cases, in fact, the differential equations integration originate stiff problems that are well solved by utilizing implicit integrators. For more information of RIGON5 please contact the author.

4.1.3 A practical case: near-polar sun-synchronous orbit

According to ESA there are some regions of space around the Earth that are particularly subject to space debris hazard due to their extensive utilization. In particular there are three so called *high ranking hotspot regions* that are defined as follows:

- altitude 800 km, inclination 98 degrees;
- altitude 850 km, inclination 71 degrees;

- altitude 1000 km, inclination 82 degrees.

Among these orbits, for a BET system those defined by the first region (i.e. sun-synchronous orbits) is among the most severe. The amplitude of the electrodynamic drag forces, in fact, depends in first place on the motional electric field E_m generated along the tether due to tether-to-plasma relative velocity $\mathbf{v}_{rel}$ and geomagnetic field $\mathbf{B}$. The motional electric field component E_m along the tether direction $\hat{\mathbf{u}}_\mathbf{t}$ reads:

$$E_m = (\mathbf{v}_{rel} \times \mathbf{B}) \cdot \hat{\mathbf{u}}_\mathbf{t} \tag{4.1}$$

If the tether is left uninsulated (bare tether) and the electrical circuit is closed through the ionosphere by means of a plasma contactor, the motional electric field component E_m makes an electrical current to flow in the tether. This current, in turn, interacts with the Earth magnetic field producing electrodynamic forces according to Lorentz law:

$$F_{el} = \int_l I(s)\, \hat{\mathbf{u}}_\mathbf{t} \times \mathbf{B} ds \tag{4.2}$$

where I is the electric current flowing inside the tether and s is the arc-length along the tether. At high-inclination orbits the angle between the magnetic field vector and the relative velocity is very small, resulting in a low motional electromagnetic field and, in turn, in a low electrodynamic force. By inspection of Eqs. (4.1) and (4.2), it can be easily seen that for high-inclination orbits $\mathbf{F}_{el}$ is close to be perpendicular to $\mathbf{v_{rel}}$, thus considerably exciting the out-of-plane libration whereas the drag component of the forces are modest. These facts lead to have lower deorbiting efficiencies (i.e., longer deorbit time) than those achievable at lower inclinations. For this reason in this work the first region was chosen as the mission profile, for if it will be demonstrated that an BET system is effective in deorbiting a spacecraft from a sun-synchronous orbit it will possibly be effective also in the other two hotspot regions. The starting orbit was fixed as in Table 4.3. Concerning the selection of the mass of the spacecraft to be deorbited, it must be noted that not all the subsystems of an BET system can be scaled down in the same way. This fact poses a lower limit in the mass-range in which a BET system is competitive. This limit could be fixed roughly around 100 kg. For this reason a 125 kg value was assigned to the spacecraft mass taking into account also the mass of the BET system, again choosing the most severe configuration. Lastly, the tether should be deployed from the mother spacecraft toward Earth to get an electron current flowing toward the cathode that we suppose installed on the spacecraft. Starting simulation year was set to 2000 that corresponds to a maximum of F10.7 solar flux. Refer to Fig. 4.10 for a complete sketch of the tethered system.

Table 4.3: Summary of the mission profile selected for a BET system preliminary optimization.

ITEM	VALUE
Starting altitude (H_0)	750 km
Orbit inclination (i)	98.7 deg
Spacecraft mass (including BET system) (M_s)	125 kg
Deployment direction	toward Earth
Starting date	1st Jan 2000

Table 4.4: Summary of tether geometry and mission performance after STEP 1 of optimization process.

Item	Value
Cut probability, N_c	1.154%
Mass ratio, m_c/M_s	2.7%
Deorbit time, t_d	73.78 days
Tether length, L_c	2.5 km
Tether width, w	1 cm
Tether thickness, h	50 µm
Tether mass, m_c	3.375 kg (Al)

4.2 Step 1: tether geometry

The first step consists in selecting the geometry of the conductive tether segment using the optimization module of BETsMA. Table 4.4 summarizes the characteristics of the optimal conductive tether segment and the deorbit performance of the mission as in Table 4.3. A brief summary of the procedure followed to obtain the results in Table 4.4 is reported below. The calculations were carried out using MASTER to model the space debris flux and the final altitude was set to $H_f = 350$km, where aerodynamic drag over the satellite and the tether is strong. A potential drop at the Hollow Cathode equal to 20 V was considered. The optimization algorithm indicates that a tether of length equal to 2.5 km, width 1cm and thickness 50 µm is the most appropriate. Therefore, using a conductive segment of 3.4 kg (aluminum density is equal to 2700 kg/m3) the satellite is deorbited from 750 km to 350 km in 73 days and tether cut probability is about 1,15%. We remark that recent tests in the CISAS Hypervelocity Impact Facility at University of Padova suggest that BETsMA survivability model is conservative [8].

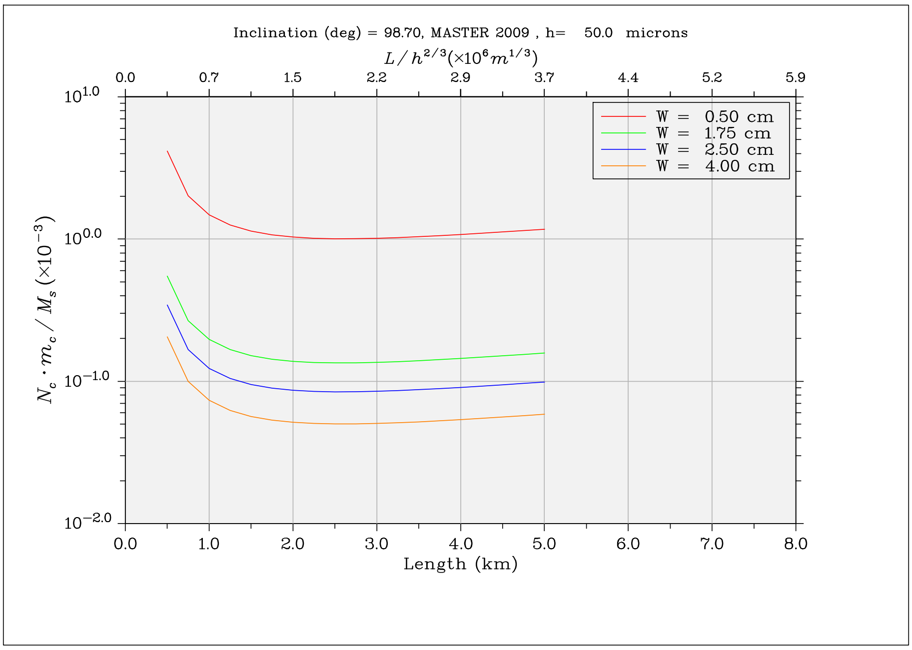

Figure 4.2: Function Π_1 versus tether length for different tape widths. ($h =$ 50 microns).

I part: optimal length

The fist step in the optimization procedure of BETsMA consists in selecting the optimal tether length that best suit the mission profile. This is done by an analytical algorithm that takes into consideration all main variables of the tethered system, such as tether geometry, average current inside the tether, orbit altitude and inclination (that are necessary to calculate average debris impact flux). Figure 4.2 shows the product of probably cut N_c and tether to spacecraft mass ratio against tether length for a given tether thickness that was fixed to $t = 50$ microns (this value derives from *BETs Project* tether prototype). The product $\Pi_1 = N_c \cdot \frac{m_c}{M_s}$ must be minimized to get a combination of low impact probabilities together with light tethers. By inspection of Fig. 4.2 the value of Π_1 has a minimum equal to $1.006 \cdot 10^{-3}$ in correspondence of $L/h^{2/3} = 1.842 \cdot 10^6 \,\mathrm{m}^{1/3}$ (or $L = 2.5$ km). It's worth to note that the optimal length does not change with respect to tether width. In turn, the value of Π_1 decreases with increasing tether width. This apparently paradoxical result is readily explained by the fact that if a tether is hit by a debris which size is smaller than tether width the probability that the tether is cut is low. The cut probability after one single impact increases and reaches values close to (or equal to) 100% when the impact size becomes comparable with tether width. Since overall debris flux decreases rapidly for increasing debris size (see Fig. 4.3), wider tethers guarantee lower cut probabilities N_c.

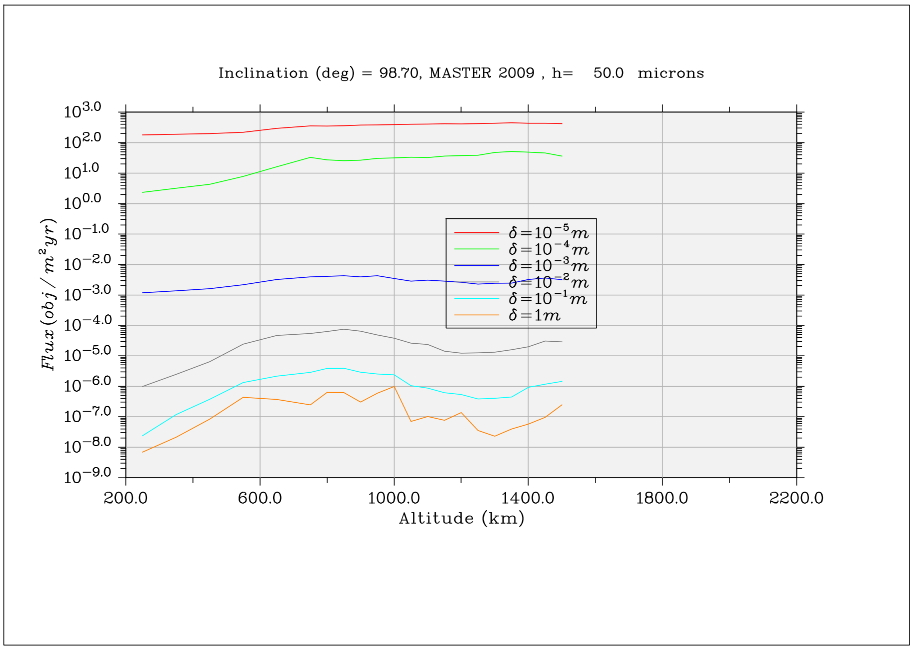

Figure 4.3: Debris flux according to MASTER for different debris dimension. ($h = 50$ microns).

II part: deorbit performance

After the length of the conductive tether is selected we can get some information on the system deorbit performances. Utilizing Fig. 4.2 the product $\Pi_2 = t_d \cdot \frac{m_c}{M_s}$ can be found. One fundamental characteristic of Π_2 is that it's value depends only on tether length whereas it is not dependent on tether width; this result is obtained from analytic calculations, more information on this matter can be found in [4]. If the tether length has been fixed in earlier steps together with spacecraft mass (in this work S/C mass is provided as input) then an unique value of Π_2 can be obtained, in particular by inspection of Fig. 4.2 Π_2 is found to be equal to 1.991 days in correspondence of $L = 2.5$ km. This, in turn, means that the product $t_d m_c$ is constant and is equal to $C = \Pi_2 M_s$. The deorbit time is therefore inversely proportional to the conductive tether mass, that is:

$$t_d = \frac{C}{m_c} = \frac{C^*}{w} \tag{4.3}$$

where the constant $C^* = \frac{C}{\rho_{Al} L h}$ is fixed for given tether length and thickness. Figure 4.4 depicts Eq. (4.3) showing the relation between deorbit time and tether width. This fundamental relation clearly states that we can obtain faster deorbiting maneuver by increasing the tether width, and viceversa. Anyway, the optimal tether width must be chosen taking into consideration others performance parameters as it is done in the next paragraph.

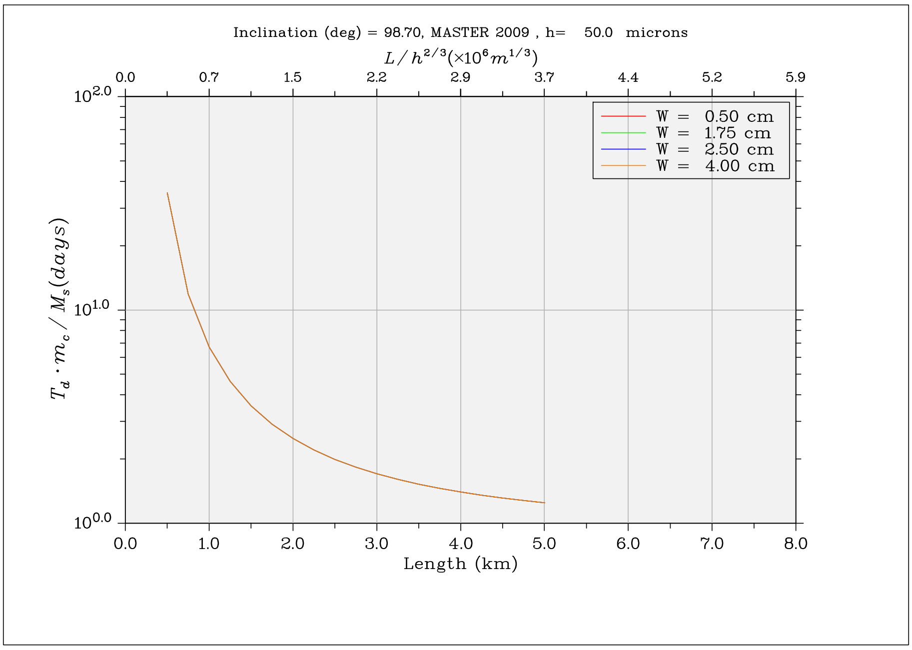

Figure 4.4: Function Π_2 versus tether length for different tape widths. Due to the no-dependence of Π_2 on tether width the curves are superimposed. ($h = 50$ microns).

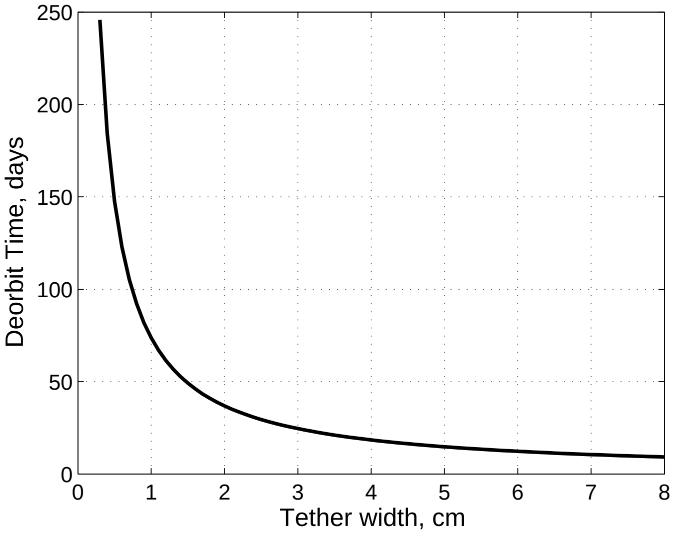

Figure 4.5: Mission performance curve for $L = 2.5$ km. Deorbit time versus tether width.

III part: tether width

The final step of BETsMA optimization process is to pinpoint the optimal tether width. Figure 4.6 depicts level curves of cut probability, tether to spacecraft mass ratio, and deorbit time in function of tether length and width. Note that, for given tether length, cut probability and mass ratio increase with lower widths, whereas mass ratio increases with increasing width. Thus, choosing a wider tether would deliver a safer system and lower deorbit time but also a heavier tether. This condition would be the best choice for the deorbiting maneuver but it would be rather unsuitable under the spacecraft mass budget point of view. For this reason the selection of the tether width must be a tradeoff between deorbit performance and tether mass budget. In particular, we shall choose the highest tether width that provide an adequate tether to spacecraft mass ratio.

To start, it is convenient to fix the maximum acceptable cut probability to 3% to guarantee a sufficient system reliability. For $L = 2.5$ km this condition is verified for roughly $w > 0.75$ cm. Table 4.5 summarizes the results obtained for different tether width. To select a proper tether width to start the iteration process of the tether system optimization we must consider that the mass of the conductive tether usually represents about 15% of the final total BET system mass, that includes tip mass, inert tether portion, deployer, electronics box, cathode, and possible devices for dynamic stabilization purposes. Also, we do not want the BET system mass to be more than 15-20% of the total spacecraft mass to keep the system competitive with other deorbiting technologies. For these reasons a tether width equal to $w = 1.00$ cm seems to be a good starting point. The corresponding deorbit performance terms are: cut probability $N_c = 1.154\%$, conductive tether to spacecraft mass ratio $\frac{m_c}{M_s} = 2.7\%$, and deorbit time $t_d = 73.78$ days.

4.3 Step 2: dumbbell model simulations

Once conductive tether geometry is known, BETsMA deorbiting module is used to obtain relevant information about the full tether system and the deorbiting mission profile. Table 4.6 summarizes some of the most important output of the deorbiting module. The oscillation of the deorbiting profile showed in the left panel of Fig. 4.7 is due to the fact that both eccentricity (Fig. 4.7, right) and inclination undergo small changes throughout the maneuver. The variation of these orbit elements causes the cut probability to be slightly higher compared with the value in Table 4.3. In turn, the deorbit time has remained practically unvaried. The deorbit module of BETsMA also provides the profiles of the electric current flowing in the conductive tether (average and in correspondence of the anode) and the anodic voltage as in Fig. 4.8. The code estimates that the maximum average current along the tether and anode voltage are equal to 1.4 A and 170 V, respectively. These values are important for the design of tether electrical system and the plasma contactor. Other quantities along the deorbiting like the motional electric field, ionospheric plasma variables and

Table 4.5: Values of performance parameters of the tether system for different tether width. ($h = 50$ microns)

Width, w [cm]	Cut probability,N_c [%]	Mass ratio, $\frac{m_c}{M_s}$ [%]	Deorbit time, t_d [days]
0.50	7.451	1.350	147.56
0.75	2.468	2.025	98.38
1.00	1.154	2.700	73.78
1.25	0.652	3.375	59.03
1.50	0.414	4.050	49.19
1.75	0.285	4.725	42.16
2.00	0.208	5.400	36.89
2.25	0.158	6.075	32.79
2.50	0.125	6.750	29.51
2.75	0.101	7.425	26.83
3.00	0.084	8.100	24.59

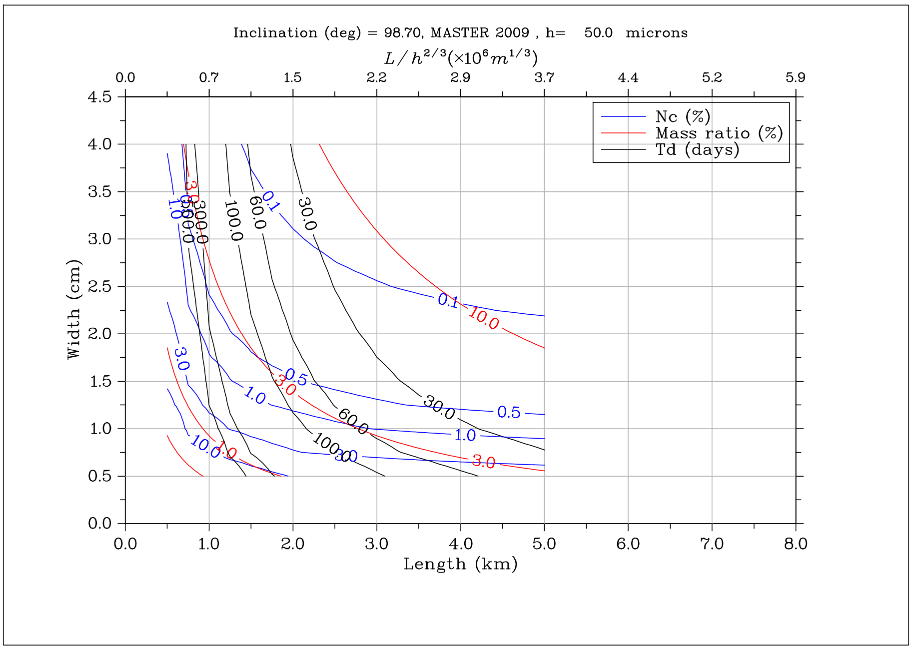

Figure 4.6: **Mission performance parameters versus the conductive tether geometry. ($h = 50$ microns)**

Table 4.6: Mission performances computed with BETsMA deorbiting module.

ITEM	VALUE
Cut probability, N_c	1.22%
Deorbit time, t_d	74 days
Average Maximum Current	1.4 A
Maximum Anode Voltage	170 V
Total BET mass	21.9 kg

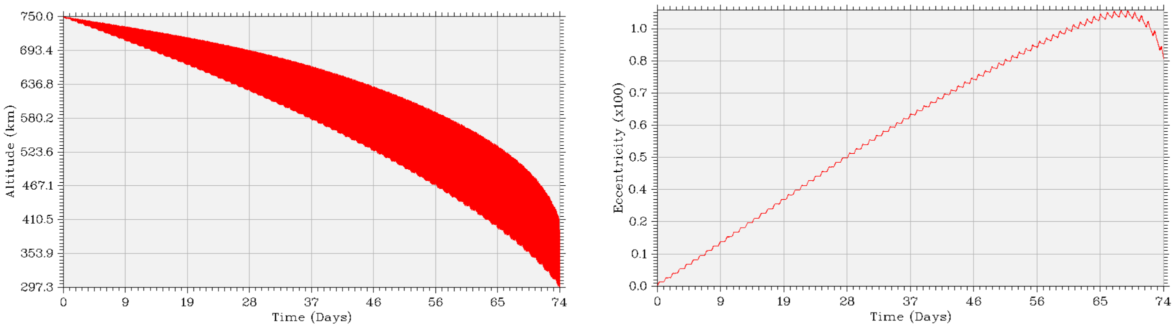

Figure 4.7: Orbital parameters during deorbiting in function of time: altitude (left) and eccentricity (right).

evolution of the orbital elements are also provided by the software but are not reported here.

Finally, BETsMA also provide an early estimation of all main subsystems mass and calculates the mass ratio of the BET system on spacecraft total mass. Figure 4.9 shows that by utilizing the tether geometry pinpointed in STEP 1 the tethered system mass percentage is about 17.5%, that is exactly half-way in the range of 15-20% that we fixed above. The mass estimations are done taking advantage of simple mathematical algorithms provided by each member of the *BETs Project* consortium. Please note that an inert portion of tether with length equal to the conductive one was assumed in the simulation as a first attempt. This assumption has proven to be suitable to dynamically stabilize the tether throughout deorbiting with most of BETs configurations.

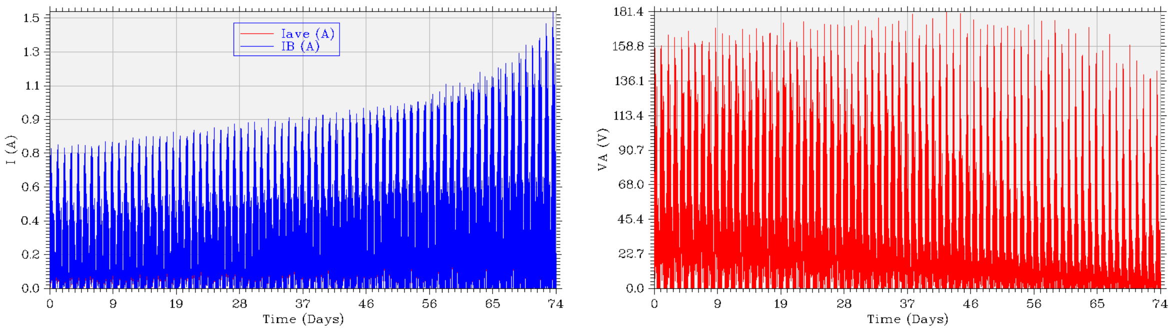

Figure 4.8: Electric current flowing in the tether (left) and anodic voltage (right) in function of time during deorbiting.

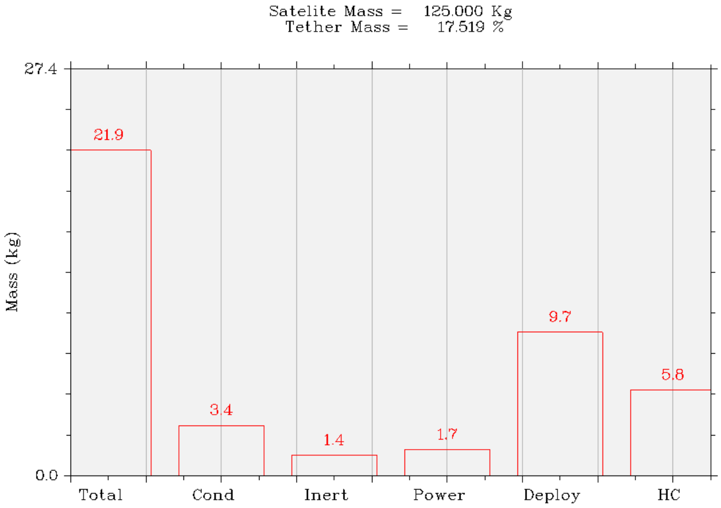

Figure 4.9: Preliminary mass budget of the BET deorbit system.

4.4 Step 3: Flexible Model Simulator and final optimization

BETsMA optimization and simulation tools are fundamental in the early design phases of a BET system as it can rapidly pinpoint essential system parameters. It focuses on the conductive tether segment, which is the core of the tether system. A BET system is characterized by a remarkable number of variables and their determination must be carried out through a complicated trade-off process. BETsMA is able to quickly discard most of the unappropriated system configuration thus greatly limiting the suitable ranges of system variables, allowing the designer to easily identify some optimal fundamental system parameters, such as tether length, width and thickness. However, some models implemented by BETsMA do not take into account several critical aspects of a space electrodynamic tether system. In particular, the software does not simulate the actual tether attitude during deorbiting and therefore cannot predict those dynamical instabilities that have been subject of deep investigation in the early 2000s by several authors [9, 10]. Furthermore, rigid dumbbell model does not consider neither the longitudinal flexibility nor the lateral bending of the tether. The former property can give rise to high frequency longitudinal modes of vibration that can couple with tether librational motion, which phenomena can adversely affect the dynamical stability of the system. Lateral bending might become relevant overall in inclined orbit missions where out-of-plane and in-plane librational motions couple giving birth to the so-called “skip rope motion” [10], a mechanism that can excite the tether eventually bringing it to dynamical instability. For these reasons, the use of BETsMA cannot be sufficient to preliminary design a BET system and the more accurate model implemented in FTS is needed to study the dynamical behavior of a BET system during deorbiting missions.

4.4.1 I part: instability countermeasures

In this study only two strategies among those listed in Par. 4.1.2 were used to keep the system simple and light, as the design of a deorbiting system for spacecraft of the class of small satellites impose a strict mass budget to keep it competitive with other deorbiting technologies. In particular two measures were utilized in the simulations: an inert portion of tether and a shock absorber. The length of the inert tether and the stiffness of the shock absorber depend on the mission profile and they are subjected to the system optimization process. Figure 4.10 depicts a sketch of a tether modeled with lump masses. As stated above, the configuration here reported refers to the configuration with the electron emitter positioned in the spacecraft, that is conventional electric current (positive charges) flows from spacecraft to the tip mass.

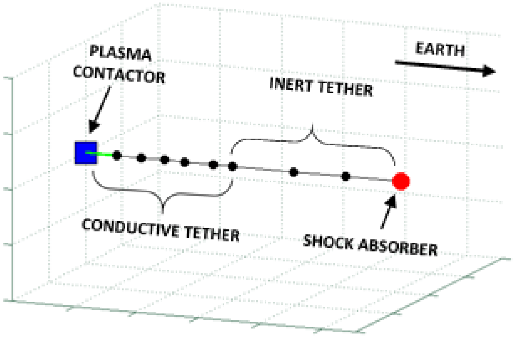

Figure 4.10: Lump masses model. The blue cube is the mother spacecraft, the red sphere is the tip mass, whereas black spheres represent the lump masses.

4.4.2 II part: first attempt with BETsMA configuration

In this paragraph simulation results obtained utilizing the configuration provided by BETsMA optimization process are reported. As first attempt, it was decided to use an inert tether of length 2.5 km, as it was done in STEP 2, together with an optimized shock absorber and a tip mass of 7 kg. Table 4.7 reports the main results obtained simulating a deorbit maneuver by means FTS utilizing the system configuration defined in Table 4.4. Figure 4.11-left depicts the deorbiting profile of the 125-kg spacecraft. The oscillating altitude is due to the fact that the initial circular orbit becomes somewhat eccentric during the maneuver, as it was also predicted by BETsMA deorbit module. The EDT system carries out a complete deorbit in 44 days, thus much faster than BETsMA prediction. This result can be regarded to the impossibility of BETsMA to determine the tether attitude. In fact, in high-inclination orbits an inclined tether (i.e., displaced from local vertical) can produce higher electrodynamic forces than a tether aligned with the local vertical. In such orbits high out-of-plane oscillations determine higher electrical current and, in turn, higher drag forces that lead to lower deorbit time. Nevertheless, the higher deorbit velocity has a cost in terms of dynamical stability. By inspection of Fig. 4.11-right it can be noted that the tether libration is pretty high, in particular the three lump masses closest to the spacecraft repeatedly reach higher altitudes than the spacecraft, meaning that the tether bending is remarkable. This is confirmed from Fig. 4.13-right from which it is possible to see that the absolute distance between spacecraft and tip mass reaches 3 km (out of 5 km total) several times throughout the maneuver. However, Figure 4.12 shows that the spacecraft-tip mass vector oscillation is limited in the -40 ÷ 40 degrees, both in the in-plane and in the out-of-plane, meaning that we still have some safety margin before instability occurs (i.e., the tether start to roll up around the spacecraft). Indeed, it is not possible to predict with reasonable precision how big this safety margin is. Therefore, for the sake of conservativeness, some adjustments to the initial configuration must be done to keep the tether libration

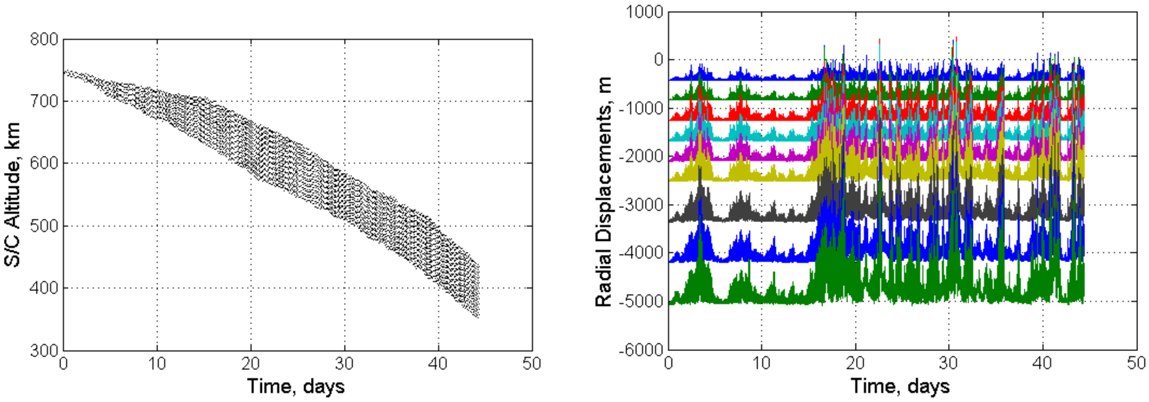

Figure 4.11: Deorbit profile of spacecraft (left) and radial displacements of lump masses with respect to orbital frame (right).

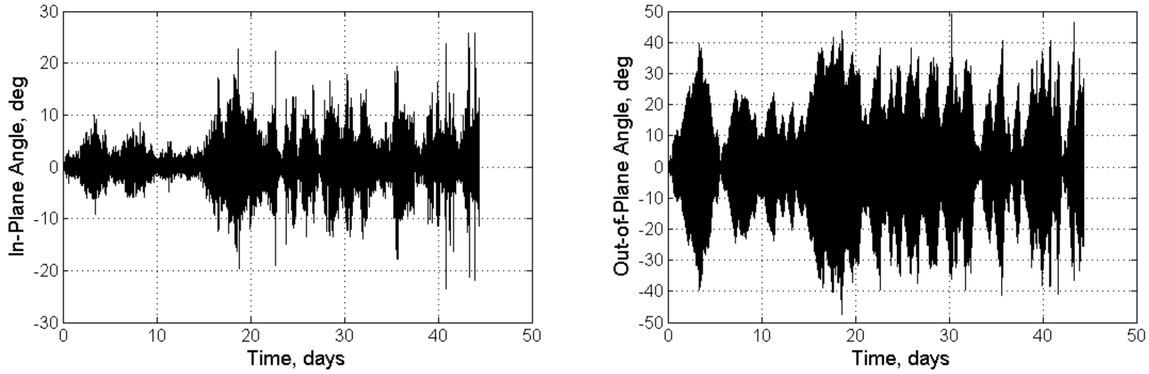

Figure 4.12: In-plane (left) and out-of-plane (right) angles of spacecraft-tip mass vector during deorbit maneuver. Tether attitude is calculated considering the instantaneous angles between the local vertical and the spacecraft-tip mass vector projected onto the orbital plane and the orthogonal one.

more restrained.

4.4.3 III part: shock absorber and final optimized configuration

Since the deorbit time found with the flexible tether simulator was lower than the one computed with BETsMA deorbit module, we can safely decrease the tether dimensions (i.e., length and thickness) to make the system lighter, more stable but still with a low (if not lower) cut probability. Starting from the tether configuration obtained from BETsMA, a numerical simulation campaign was carried out with the aim of further optimizing the tether system, this time taking into account dynamical issues. Table 4.7 reports a full summary of all the simulated system configurations. Several simulations were run to find the best shock ab-

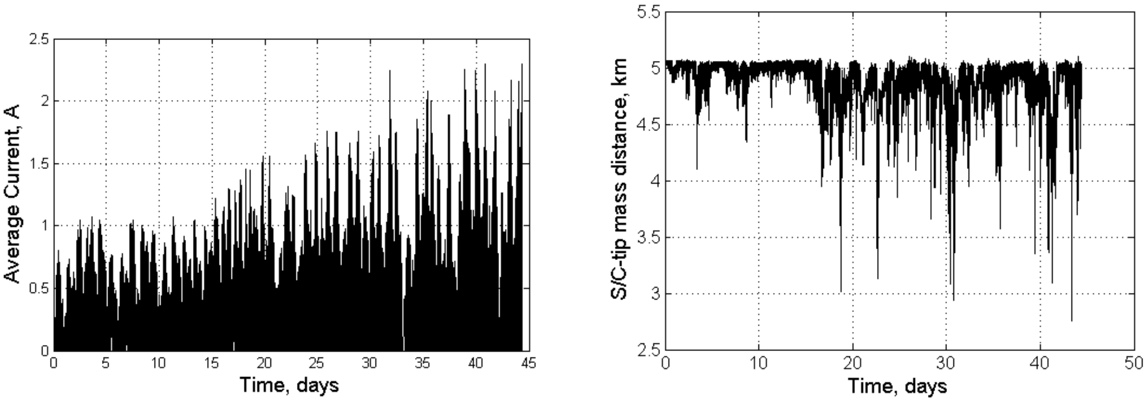

Figure 4.13: Average electric current flowing through electrodynamic portion of tether (left) and absolute distance between spacecraft and tip mass (right).

sorber parameters (i.e., stiffness and damping parameters). A tip mass of 7 kg was chosen as first attempt for all cases. Case 1 refers to the system configuration outlined by BETsMA optimization module and it was already described in Par. 4.3. In Case 2 the conductive tether was shortened and results showed a higher dynamical stability together with higher deorbit time. In subsequent Case 3 also the inert tether was shortened to try to lower the system mass, but this has proven not to be a good solution as the dynamical stability worsened considerably. In the last Case 4 it was decided to utilize a thinner and shorter conductive tether maintaining a 2.5-km inert tether. This configuration has proven to be the lightest and most stable one and still with a reasonable deorbit time now matching the one predicted from BETsMA (see Table 4.6). Once the conductive and inert tether length and cross section were fixed further simulations were run to verify if the tip mass could be reduced without affecting the system stability. It turned out that the optimal system configuration was that outlined by Case 4 adopting a 6-kg tip mass. In summary, a shorter and thinner conductive tether was selected to lower system mass together with electrodynamic forces amplitude. Also the tip mass is 1 kg lighter, whereas the length of the inert portion of the tether was left unchanged to ensure a robust dynamic stability. Due to the lower current (1.5 A maximum) the deorbit time has increased and now it matches the one predicted by BETsMA. Figures 4.14-4.16 depict the optimal configuration system deorbit variables in function of the time. With respect to Case 1, the higher level of stability can be noted from Figs. 4.14-right and 4.16-right. With this system configuration no lump masses experience positive radial displacements (with respect to the spacecraft) and the absolute distance between spacecraft and tip mass never drops below the 80% of the total tether length (60% in CASE 1). From Fig. 4.15-right it is possible to see that the range of tip mass attitude angle in the out-of-plane is roughly ±40deg and it remains unaltered with respect to Fig. 4.12-right, whereas the in-plane angle undergoes more restrained oscillation:

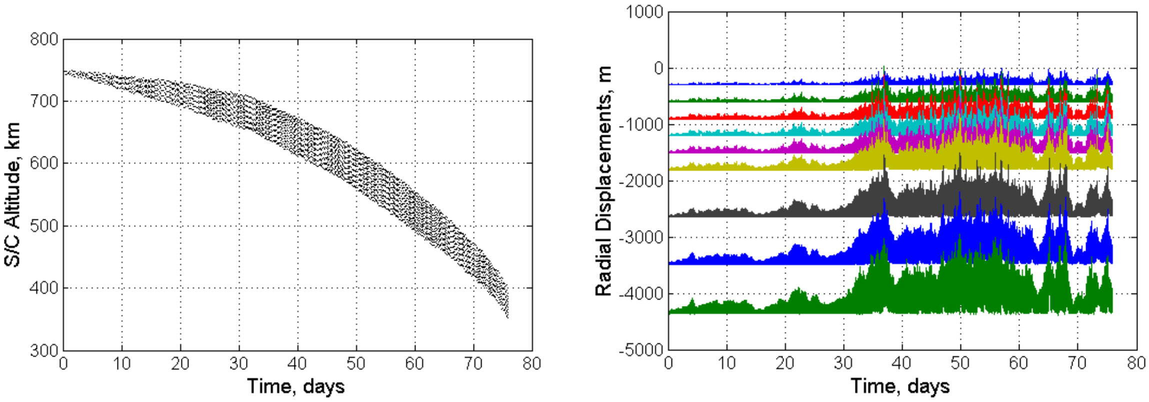

Figure 4.14: Deorbit profile of spacecraft (left) and radial displacements of lump masses with respect to orbital frame (right) for the final optimized configuration.

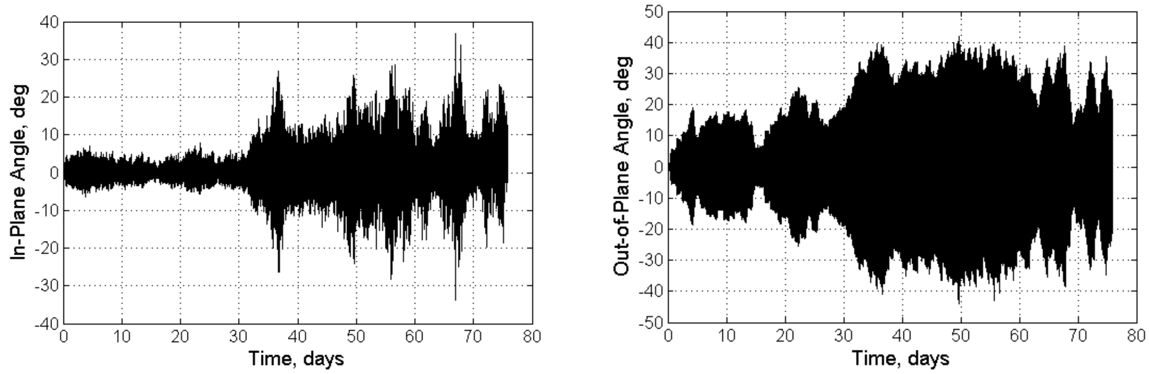

Figure 4.15: In-plane (left) and out-of-plane (right) angles of spacecraft-tip mass vector during deorbit maneuver for the final optimized configuration.

±15deg of Fig. 4.15-left versus ±20deg of Fig. 4.12-left. Current profile, depicted in Fig. 4.14-left, shows that the average current flowing in the tether is substantially lower throughout the maneuver. This fact can be regarded as the first cause of the higher system dynamical stability together with the higher deorbit time: as it was already explained it Par. 4.1.3, roughly lower current levels correspond to lower electrodynamic forces.

4.5 Conclusion

A preliminary design of an end-of-life deorbiting system for a 100-kg class microsatellite based on bare electrodynamic tether technology has been carried out. The study has been conducted by means of two synergistic *ad-hoc* software developed within the FP7 program *BETs Project*: BETsMa, developed at the Technical University of Madrid, and the Flexible Tether Simulation (FTS), developed

Table 4.7: **System configurations resulting from the numerical optimization process carried out by means of FTS.**

CASE	Conductive tether L_c [km]	Inert tether L_i [km]	Tether cross section $w \times h$ [cm X µm]	Tip mass m_B [kg]	Deorbit time t_d [days]	Maximum average current I_{max} [A]	Tether dynamical stability
1	2.5	2.5	1 X 50	7	˜44	2.3	low
2	2	2.5	1 X 50	7	˜60 ÷ 65	2.0	high
3	2	2	1 X 50	7	˜56 ÷ 60	2.1	medium
4	1.8	2.5	1 X 30	5 ÷ 7	˜60 ÷ 76	1.4 ÷ 1.6	very high

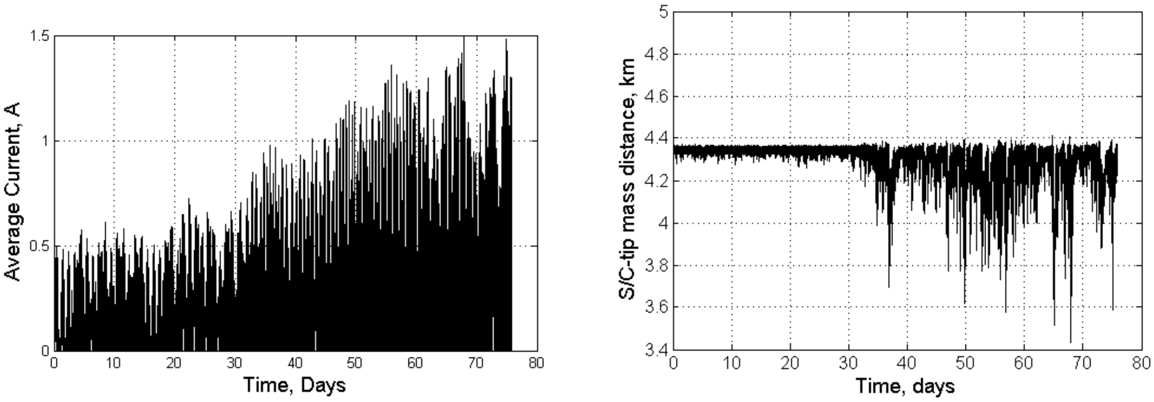

Figure 4.16: Average electric current flowing through electrodynamic portion of tether (left) and absolute distance between spacecraft and tip mass (right) for the final optimized configuration.

at the University of Padova. The process flow from initial mission profile definition to final optimal system configuration selection has been described. In order to define an exemplifying mission profile, a densely populated sun-synchronous orbit has been selected among the three high-ranking hotspots regions identified by ESA. Subsequently, the first step of the preliminary design has been carried out utilizing the BETsMA optimizing module. Thanks to an innovative semi-analytical algorithm, this tool is able to pinpoint a restricted set of BET system configurations optimized for the given mission profile. Once the first attempt of optimal configuration was outlined, the second step of the design has been carried out by means the BETsMA deorbit module, based on a dumbbell-model simulator, that provides the profiles of fundamental system variables. The third and last step has been conducted through an extensive numerical simulation campaign utilizing the Flexible Tether Simulator. After a trade-off between system mass, deorbit time, and tether dynamical stability the final optimal configuration of the BET deorbiting system was defined. The mission selected is one of the most severe for the tether system due to the high inclination and the relatively low satellite mass (about 100kg). This work demonstrated that bare tethers can efficiently deorbit the satellite with a low cut probability in just few months. In this respect, the determination of the tether geometry is crucial and an appropriate set of numerical tools must be used. For instance, this work showed that, if tether attitude is considered in high orbit inclination missions, then deorbit time decreased with respect to simulations carried out with simple dumbbell models. This has an important impact on the performance of the mission. In fact, the initial configuration designed with BETsMA estimated a tether mass about 22 kg. However, for Case 4 in Table 4.7, we find a total mass of 14.4 kg distributed as follows: conductive tether 1.5 kg, inert tether 0.8 kg, electrical system 1 kg, deployer system 5.4 kg, and plasma contactor 5.7 kg. The main cause of the difference between the total masses is due to deployer subsystem, which is much lighter in the optimized case because of the shorter conductive tether. To the 14.4 kg the tip mass contribution should be added, nonetheless at the moment of the writing of this work the option of using the deployer as the tip mass is still under consideration. Also, it must be taken into account that the above mass estimations are based on preliminary empirical algorithms provided by each of *BETs Project* partner. However, a proper integration process of all subsystems has not been done yet so that the sum of masses provides an overrated estimation due to redundancies. The integration process of the BET system could deliver a lighter configuration, let's say about 10% of the small satellite mass. For heavier satellites, the percentage would be even smaller because the mass of some subsystems, like the plasma contactor or the electrical system, would be essentially the same as for a small satellite.

Bibliography

[1] Sánchez-Arriaga, G., Bombardelli, C., and Chen, X., *Impact of Nonideal Effects on Bare Electrodynamic Tether Performance*, Journal of Propulsion and Power. (Accepted)

[2] Sánchez-Arriaga, G., *BETsMA Manual*, URL: http://www.thebetsproject.com/resources [cited 30 Jan 2015].

[3] Zanutto, D., Colombatti, G., and Lorenzini, E. C., *Electrodynamic Tethers For Deorbiting Maneuvers*, 3rd CEAS Air&Space Conference, Venice, Italy, 2011.

[4] Sanmartín, J. R., Sánchez-Torres, A., Khan, S. B., Sánchez-Arriaga, G., and Charro, M., *Optimization method in tape-tether sizing for de-orbiting satellites at end of mission.* (submitted)

[5] Bau, G., Hunh, A., Urrutxua, H., Bombardelli, C., Peláez, J., *DROMO: a new regularized orbital propagator*, International Symposium on Orbit Propagation and Determination, Sept. 2011, IMCCE, Lille (F).

[6] Zanutto, D., Lorenzini, E. C., Mantellato, R., Colombatti, G., and Sanchez-Torres, A., *Orbital Debris Mitigation Through Deorbiting with Passive Electrodynamic Drag*, 63rd International Astronautical Congress, IAF, Naples, Italy, 2012.

[7] Bombardelli, C., Peláez, J., Sanjuro, M., Asymptotic solution for the current profile of passive bare electrodynamic tethers, Journal of Propulsion and Power, Vol. 26, No. 6, Nov.-Dec. 2010. doi: 10.2514/1.46808

[8] Francesconi, A., Giacomuzzo, C., Branz, F., and Lorenzini, E.C., *Survivability to Hypervelocity Impacts of Electrodynamic Tape Tethers for Deorbiting Spacecraft in LEO*, 6th Conference on Space Debris, 2013, April 22-25, Darmstadt, Germany.

[9] Peláez, J., Lorenzini, E. C., López-Rebollal, O., and Ruiz, M., *A New Kind of Dynamic Instability in Electrodynamic Tethers*, Journal of the Astronautical Sciences, Vol. 48, No. 4, 2000, pp. 449-476.

[10] Peláez, J., Ruiz, M., López-Rebollal, O., Lorenzini, E. C., *Two-Bar Model for the Dynamics and Stability of Electrodynamic Tethers*, Journal of Guidance, Control and Dynamics, Vol. 25, No. 6, 2002, pp. 1125-1135.Peláez, J.,

Lorenzini, E. C., López-Rebollal, O., and Ruiz, M., *A New Kind of Dynamic Instability in Electrodynamic Tethers*, Journal of the Astronautical Sciences, Vol. 48, No. 4, 2000, pp. 449-476.

Acknowledgements

I am and I will always be grateful to my family for giving me life, love, shelter. I would like to deeply thank prof. Lorenzini for considering me trustworthy since the beginning and for teaching me countless lessons, thank you Enrico, I hope you will keep on teaching me. Thanks also to Gonzalo, for the fruitful collaboration during my stay in Madrid and for the support he gave me during exhausting working days. I special thought goes to my little family in Madrid, las Bubies y Pivano y Daviduccio, it could have been hell without you. Thank you Claudio for your valuable tips on work, for your friendship, and above all for your music. Good luck to Ufficio Arroganza & co. for your future and thank you for the good time. Thanks to my Virgin Fortress brothers for making me feel cleverer, mojito? Thanks to all my friends that did not consider my Ph.D. a waste of time. Thank you Vale for your love.